Synthesis and applications of multifunctional hybrid materials based on microgel particles

D i s s e r t a t i o n

zur Erlangung des akademischen Grades

d o c t o r r e r u m n a t u r a l i u m

(Dr. rer. nat.)

im Fach Chemie

eingereicht an der

Mathematisch-Naturwissenschaftlichen Fakultät

der Humboldt-Universität zu Berlin

von

M. Sc. He Jia

Präsident der Humboldt-Universität zu Berlin

Prof. Dr.-Ing. Dr. Sabine Kunst

Dekan: der Mathematisch-Naturwissenschftlichen Fakultät

Prof. Dr. Elmar Kulke

Gutachter: 1. Prof. Dr. Matthias Ballauff

2. Prof. Dr. Klaus Rademann

Tag der mündlichen Prüfung: 15.11.2016

True Strength is being able to hold it together when everyone is expecting you to fall apart.

Bruce Lee

To my family & friends

Abstract

The combination of inorganic nanoparticles and organic microgels in one hybrid system allows for the preparation of new materials with multifunctional properties. Ideally, such hybrid materials reflect both the properties of its individual components and synergetic effects due to the interaction between inorganic nanoparticles and microgels.

In the first part of this thesis, the fabrication of Cu_2O@Poly(N-isopropylacrylamide) (PNIPAM) core-shell nanoreactors has been presented. It was found that the PNIPAM shell effectively protects the Cu_2O nanocubes from oxidation. The core-shell microgels have been used as photocatalyst for the decomposition of methyl orange and a significant enhancement in the catalytic activity has been observed compared with the bare Cu_2O nanocubes. Most importantly, the photocatalytic activity of the core-shell nanoreactors can be further tuned by the thermosensitive PNIPAM shell. The aqueous solution of Cu_2O@PNIPAM core-shell nanoparticles with quite low solid content (1.5wt. %) can be also directly used as a novel ink material for the inkjet printing without adding any other surfactants and organic solvents. The gas sensor device printed by core-shell nanoparticles is more sensitive to NO_2 than that made from the bare Cu_2O nanocubes.

In the second part, a kind of hybrid microgel has been fabricated by immobilization of catalytically active Au nanoparticles in the α-cyclodextrin (α-CD) modified poly(N-vinylcaprolactam) (PVCL) microgels without addition of reducing agent and surfactant. The hybrid microgels can work efficiently as catalyst for the reduction of aromatic nitro-compounds by using the reduction of 4-nitrophenol (Nip) and 2,6-dimethyl-4-nitrophenol (DMNip) as model reactions. Due to the selective binding property of α-CDs to nitro compounds, the synthesized hybrid microgels show different catalytic activity for the target compounds, 4-nitrophenol (Nip) and 2,6-dimethyl-4-nitrophenol (DMNip), during the catalytic reactions.

Key words: hybrid microgels, nanoreactors, Cu_2O nanocubes, Au nanoparticles, thermosensitive, catalysis, inkjet printing, gas sensor, cyclodextrin.

Zusammenfassung

Die Kombination aus anorganischen Nanopartikeln und Mikrogelen in einem hybriden System erlaubt die Herstellung von Materialien mit vielseitigen neuen Eigenschaften. Im Idealfall weisen solche hybriden Materialien neben den Eigenschaften von beiden indivduellen Systemen zusätzlich synergetische Effekte auf, welche aus den Interaktionen zwischen dem anorganischen Nanopartikel und dem Mikrogel resultieren.

Im ersten Teil dieser Arbeit wird eine neuartige und eingängige Methode zur Herstellung von Cu_2O@PNIPAM Kern-Schale Nanoreaktoren präsentiert. Die PNIPAM Schale schützt dabei die Cu_2O Nanopartikel effektiv vor Oxidation. Die Cu_2O@PNIPAM Kern-Schale Strukturen wurden als Photokatalysator zum Abbau von Methylorange unter sichtbarem Licht eingesetzt. Im Vergleich zu den reinen Cu_2O Nanopartikeln konnte eine signifikante Steigerung der katalytischen Aktivität festgestellt werden. Desweiteren kann die photokatalytische Aktivität mittels Temperatur durch die thermosensitive PNIPAM Schale abgestimmt werden. Verhältnismäßig geringe Konzentrationen einer Cu_2O@PNIPAM wässrigen Lösung (1,5 Gew%) können direkt als neuartige Tinte genutzt werden. Keine zusätzlichen Additive oder organische Lösungsmittel sind für die Strahldruckprozesse vonnöten. Gedruckte Bauelemente bestehend aus den Cu_2O@PNIPAM Kern-Schale Strukturen wurden als Gas Sensoren eingesetzt und zeigten eine geringere Nachweisgrenze für NO_2 als die reinen Cu_2O Nanowürfel.

Im zweiten Teil der Arbeit wurden katalytisch aktive Au Nanopartikel an copolymerisierten α –Cyclodextrin (α-CD) Einheiten in einem Poly(*N*-vinylcaprolactan) (PVCL) Mikrogel immobilisiert. Diese hybriden Partikel sind sehr aktive Katalysatoren für die Reduktion von aromatischen Nitroverbindungen. Die Reduktion von 4-Nitrophenol (Nip) und 2,6-Dimethyl-4-nitrophenol (DMNip) wurden als Modellreaktionen ausgewählt. Durch selektive Bindungseingenschaften der Nitroverbindungen an die α-CD Einheiten konnten verschiedene katalytische Aktivitäten für Nip and DMNip festgestellt werden.

Schlagwörter: Hybride Mikrogele, Nnaoreaktoren, Cu_2O Nanowürfel, Au Nanopartikel, thermosensitiv, Katalyse, Tintenstrahldruck, Gas Sensor, Cyclodextrin.

Table of contents

1. Introduction

Hybrid materials are composites of two constituents at the nanometer or molecular level. In general, one of these compounds is inorganic and the other is organic in nature.[1] Commonly, a hybrid material possesses both of the original properties of the components and the properties that do not exist in either of the parent components.[2–4] In this thesis, two novel hybrid materials based on stimuli-responsive microgels have been synthesized and the applications of these two novel materials have been intensively investigated.[5,6] In the following the main results of these studies will be presented and discussed.

1.1 Hybrid materials based on stimuli-responsive microgels

Stimuli-responsive microgels have gained increasing attention in recent years as they can undergo reversible conformational changes in response to external stimuli, which are often accompanied by variations in the physical and chemical properties of the polymers, such as volume, shape, surface area, solubility, or mechanical properties.[7–10] More importantly, these properties can be used to tune the corresponding properties of the functional nanoparticles embedded inside the microgels.[5,6,11,12] The hybrid materials based on stimuli-responsive microgels can be mainly classified into two groups. One is using microgel as the carrier to load different functional nanoparticles,[13–17] the other is the core-shell hybrid microgels with functional nanoparticles as the cores.[12,18–22]

1.1.1 Microgel as carrier for the generation of functional nanomaterials

The stimuli-responsive microgels can provide excellent nucleation and growth environments for functional nanoparticles without aggregation due to the availability of free spaces in the swollen gel networks.[12,23–25] Thus, the networks of the microgels are well-suited for in-situ synthesis of catalytically active metal nanoparticles. Until now, different microgel systems have been developed and applied as "nanoreactors" for the deposition of metal nanoparticles (NPs).[26–28]

Liz-Marzán and his co-workers have successfully coated PNIPAM shell on the surface of highly magnetic iron oxide nanocrystals and stabilized silver nanoparticles in situ inside the PNIPAM networks. They also reported that the temperature-responsive PNIPAM shell with limited cross-linking density allowed for particularly efficient control of embedded Au nanoparticles.[14,20,29] Kumacheva *et al.* used polyampholyte poly(*N*-isopropyl acrylamide-co-acrylic acid-co-vinyl imidazole) (poly(NIPAm-AA-VI)) microgels as nanoreactors to fabricate gold nanorods within the microgels.[15] In the research of Pich *et al.*, poly[(*N*-vinylcaprolactam)-

co- (acetoacetoxyethyl methacrylate)] (PVCL/AAEM) microgels have been used to immobilize ZnS nanoparticles by the reaction of zinc acetate and thioacetamide under ultrasonic agitation.[17] Recently Suzuki *et al.* used NIPAM and 3-(methacrylamino) propyltrimethylammonium chloride (MAPTAC) as monomers to synthesize thermosensitive microgels as carriers to immobilize Au nanoparticles. In their study, the cationic sites in the microgels were used to nucleate the particle growth, while $NaBH_4$ and dimethylamineborane were used as the reducing agents.[16] In the previous study of our group, thermosensitive PS-PNIPAM core-shell microgels have been applied as the nanoreactors to generate Ag nanoparticles as well as Au, Rh, Pt nanoparticles. [13,31,32]

In most of these studies, the synthesis of metal nanoparticles using microgels as template has been always conducted in the presence of strong reducing agents, such as $NaBH_4$, H_2, NH_2NH_2 and so forth.[33–35] The use of strong reducing agents, however, will limit the type number of microgels according to the functionalities within the polymer with respect to chemical stability.[6,33,34,36] Moreover, a random distribution of metal nanoparticles inside the microgel structure will be obtained with such approaches. Developing a novel hybrid material based on microgel particles without use of reducing agents will open new possibilities for the synthesis of hybrid colloidal particles directly under mild conditions and facilitate the use for catalytic applications.

1.1.2 Core-shell hybrid microgels with functional nanoparticles as the cores

Recently, as the most famous stimuli-responsive microgels, poly(N-isopropylacrylamide) (PNIPAM) microgels have been used as the shells to modify inorganic nanoparticles.[18,22] In this way, the nanoparticles encapsulated inside PNIPAM shells can be prevented from aggregation in aqueous solution.[19]

For example, Liz-Marzán and co-workers developed Au@PNIPAM core-shell nanoparticles via the growth of PNIPAM gels on the surface of Au nanoparticles.[29,37] Lu and her co-workers also successfully synthesized different kinds of core-shell or yolk-shell hybrid systems with PNIPAM in the last few years.[12] The corresponding results have been shown in Figure 1.1.2.1.

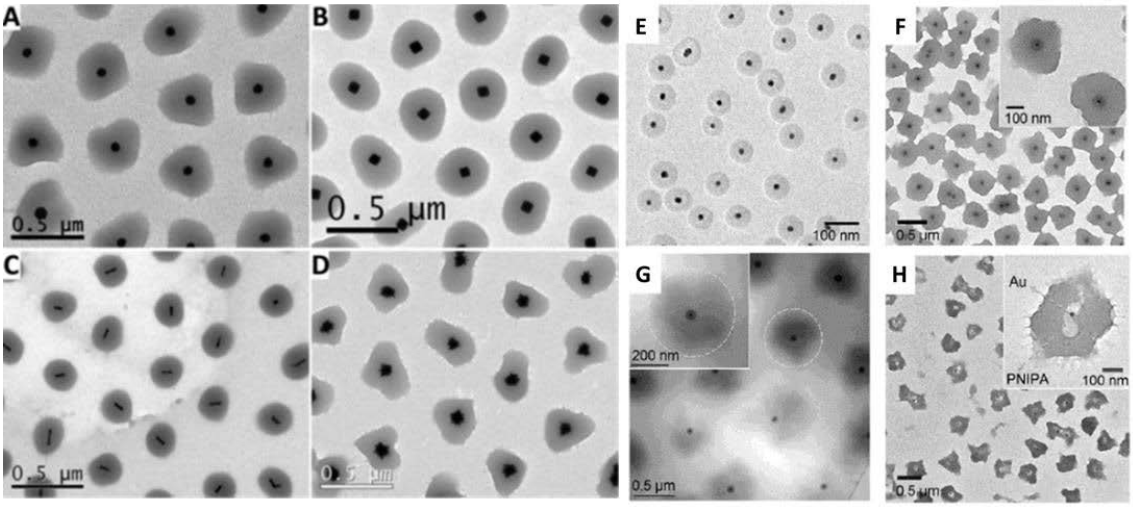

Figure 1.1.2.1 TEM images of Au nanoparticles coated with PNIPAM: (A) spheres, (B) octahedral, (C) nanorods and (D) nanostars. (E) TEM image of Au-SiO_2 core-shell nanoaprticles. (F) TEM image of Au-SiO_2-PNIPAM trilayer composites. (G) Cryo-TEM image of Au-SiO_2-PNIPAM core-shell nanoparticles. (H) TEM image of Au-PNIPAM yolk-shell nanoparticles. Reprinted from ref.[12,20] Copyright 2013 with permission from *The Royal Society of Chemistry* and 2012 with permission from *WILEY-VCH.*

Besides the Au nanoparticles, Li et al. synthesized a novel Ag@PNIPAM core-shell nanocomposite particle which combines the thermoresponsive property of PNIPAM and the metal-enhanced fluorescence effect of Ag together.[38] Yu and his co-workers prepared core-shell nanoparticles comprised of a Fe_3O_4 core and a mesoporous silica shell coated with a PNIPAM layer.[39] ZnO, CdS and several other kinds of metallic/metal oxide nanoparticles have also been used as the cores for the modification of PNIPAM.[40–42]

Recently, Angioletti-Uberti *et al.* presented a theory for the diffusion- and solvation-controlled contribution to the reaction rate of such a core-shell "nanoreactor".[11] It was demonstrated that the thermosensitive shell can be used to enhance or reduce the local concentration and permeability of a given reactant and thus increase or decrease the total catalytic activity of the embedded nanoparticle, respectively. Thus, core-shell systems consisting of a catalytically active nanoparticle and a polymeric shell present a novel type of mesoscopic catalyst with tunable properties.

Compared with the stable metallic/metal oxide nanoparticles, Cu_2O nanomaterial is more easily degraded with the changes in environmental conditions, because of which the classical methods for the PNIPAM coating cannot be applied to Cu_2O materials. Thus, to the best of our knowledge, until now very few work has been reported on the colloidal stable Cu_2O

nanoparticles modified with PNIPAM shells. Such functional hybrid nanoparticles will not only improve the stability of sensitive semiconductor nanoparticles, but also can be applied as "nanoreactors" with stimuli-responsibility.

1.2 Stimuli-responsive microgels

Microgels are crosslinked polymeric particles, which were firstly proposed by Baker in 1949.[43] The word "micro" from Baker's work refers to the size of the gel particles and the "gel" represents the swelling behavior of the particles in the solvent. Microgels containing interactive functional groups along the main polymeric chains are normally named as "stimuli-responsive" microgels. Recently, more and more attentions have been paid on this kind of special microgels. Because of the functionalized polymer chains, the solubility, volume, configuration and conformation of the microgels can be reversibly manipulated by external stimuli involving chemical and physical signals. The chemical signals including pH, metabolites and ionic species can alter the molecular interactions with the polymeric chains and solutes,[44–47] while the physical signals, such as temperature, light, shear force, pressure and electrical potential, can be used to alter the energies of chain dynamics and molecular interactions.[48–50] With further research on these special properties, stimuli-responsive microgels can be applied in different areas such as drug delivery,[51,52] sensing,[53,54] fabrication of photonic crystals,[27,55,56] template-based synthesis of metallic nanoparticles and purification technologies.[44]

Among different kinds of stimuli-responsive microgels, thermo-responsive microgel becomes the most popular one since it exhibits properties in common with water-soluble polymers, water swollen macro gels and water insoluble latex particles at different stages with the increase of temperature.[57] Nowadays, the most commonly used temperature-sensitive microgels are poly(N-isopropyl acrylamide) (PNIPAM) and poly(N-vinylcaprolactam) (PVCL), the monomer structures of which are shown in Figure 1.2.1, respectively.[58–61] At low temperature, the polymer chains are soluble in water due to the formation of hydrogen bonds between the water molecules and the amide side chains. In this case, the PNIPAM and PVCL microgels exhibit similar properties like water-soluble polymers and water swollen macrogels. When temperature increases, the chains of microgel become hydrophobic, which leads to the shrinkage of the microgel by expelling water from the interior. At this stage, the property of the microgels is closer to water insoluble latex particles.[6,62]

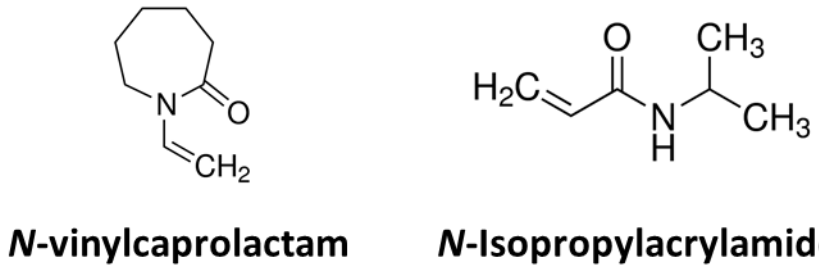

***N*-vinylcaprolactam** **N-Isopropylacrylamide**

Figure 1.2.1 Structures of N-vinylcaprolactam (VCL) and N-isopropylacrylamide (NIPAM).

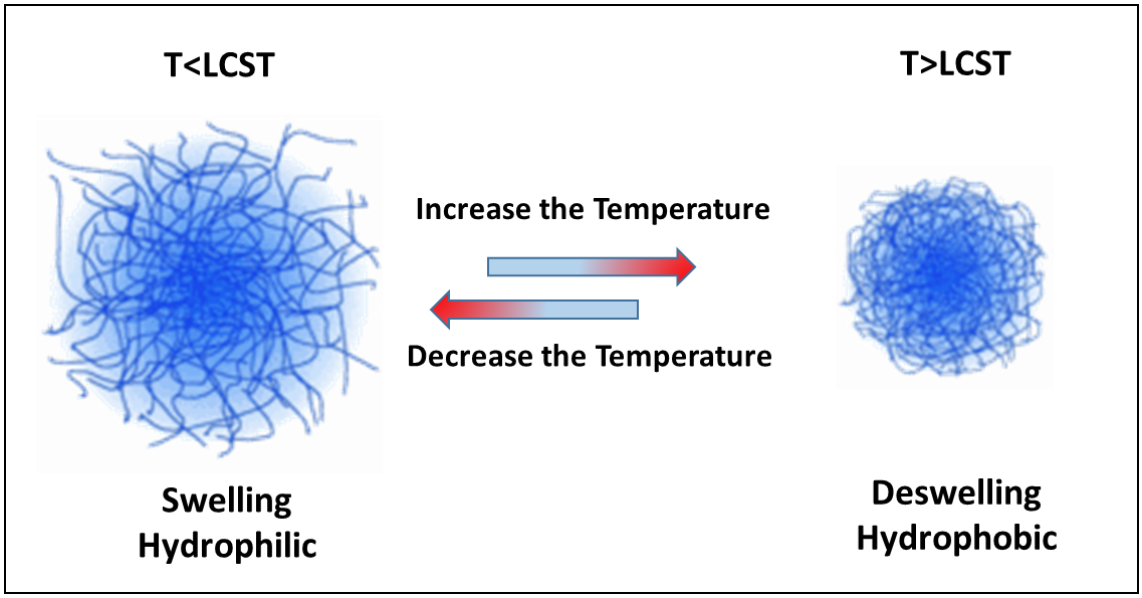

Figure 1.2.2. A schematic illustration of the transition behavior of PNIPAM microgels below and above the LCST.

The mechanism of the changing of PNIPAM or PVCL microgels at different temperatures has been shown in Figure 1.2.2. In aqueous media, both PNIPAM and PVCL exhibit a lower critical solution temperature (LCST), which is attributed to a shift in the distribution of hydrophobic and hydrogen-bond interactions. [31,63]

Recently, the research on PNIPAM and PVCL thermosensitive microgels has been further developed. Makino et al., our group and several other groups have successfully used a two-stage approach to synthesize polystyrene (PS)-PNIPAM core-shell systems.[13,32,64] This kind of system can be used as nano-reactors for the generation of various metallic nanoparticles. Pich and his co-workers developed poly[(*N*-vinylcaprolactam)-co-(acetoacetoxyethyl methacrylate)] (PVCL/AAEM) co-polymer as the carriers for the generation of different metallic nanoparticles.[65] Nowadays more and more researches have been focused on hybrid nanoreactors based on these two thermosensitive microgels.

1.3 Functional nanoparticles

1.3.1 Au nanoparticles

The modern research on gold nanoparticles began from 1850s when Michael Faraday first observed the different properties between gold nanoparitcles and bulk gold materials.[66] Due to the unique properties of Au nanoparticles, they represent an ideal platform for chemical and biological sensing as well as applications in nanomedicine. Moreover, after Hutchings and coworkers first applied gold nanoparticles as catalysts for the hydrochlorination of ethylene to vinyl chloride, Au nanoparticles were discovered to display catalytic properties for various reactions.[67]

Since the performance of the Au catalysts is highly dependent on the size and shape of the nanocrystals and the stimuli-responsive microgels can provide excellent nucleation and growth environments for nanoparticles without aggregation, various microgel systems have been developed and applied as "nanoreactors" for the deposition of Au nanoparticles (NPs). For instance, Ballauff and his co-workers used spherical polyelectrolyte brushes (SPB) as the carrier systems to obtain Au nanoparticles with an average size of 2-4 nm, which present very high catalytic activity for the p-nitrophenol reduction.[68,69] PNIPAM and PVCL microgels have been also used to synthesize Au nanoparticles by Hellweg, Liz-Marzán and Pich, respectively.[2,20,47,70]

However, for most of the above systems, the synthesis process of Au nanoparticles has been always conducted in the presence of strong reducing agents and a large amount of surfactant, which will impact on the surface property of gold nanoparticles.

Although poly(*N*-vinyl-2-pyrrolidone) and polyvinylpyrrolidone (PVP) can work as both the surfactants and the reducing agents for the preparation of homogeneous metal nanoparticles, they could not work as the "nanoreactor" as observed for microgels.[71,72] More recently, Pich *et al.* have reported that a newly developed *N*-vinylcaprolactam/acetoacetoxyethyl methacrylate/acrylic acid based microgel displays in situ reductive reactivity towards $HAuCl_4$, forming hybrid polymer-Au nanostructures at ambient temperature without additional reducing agents.[73] The Au nanoparticles immobilized inside the microgels have good catalytic activity. However the hybrid systems do not contain the selectivity for the reactants. Thus, it is still a big challenge to develop an active "nanoreactor" based on stimuli-responsive microgels for the generation of functional metal nanoparticles containing specific/selective binding domains on the surface without the use of reducing agents and surfactant. This will open new possibilities

for the synthesis of metal hybrid colloidal particles directly under mild aqueous conditions and facilitate the use for catalytic applications.

In this thesis, poly(*N*-vinylcaprolactam) (PVCL) microgel modified with reactive α-cyclodextrins (α-CDs) has been synthesized and successfully used to reduce and stabilize Au nanoparticles in situ without any additional surfactant and reducing agents. Moreover, because of the different complexation abilities of CDs with aromatic nitro compounds with various structures, the Au nanoparticles could show specific/selective binding abilities to certain reagents resulting in enhanced catalytic activity.

1.3.2 Cu_2O nanoparticles

Cu_2O is a well-known native p-type semiconductor, which is highly abundant in the earth crust. As the band gap of Cu_2O is 2.17 eV, it exhibits great potential for the applications in solar energy conversion, lithium-ion batteries, gas sensors, photocatalytic degradation of dye molecules, propylene oxidation and photoactivated water splitting. [74–77] Since the properties of the Cu_2O nanoparticles are strongly dependent on their shape, there is a growing interest in the synthesis of Cu_2O nanostructures with defined shape.[78–83] Thus, Cu_2O nanocubes, octahedral, nanocages, spheres, nanowires and other highly symmetrical structures have already been reported (as shown in Figure 1.3.2.1).[77,84]

A main drawback for further applications of Cu_2O nanoparticles is the easily oxidized property of Cu_2O in water and the destroying of nanostructure of Cu_2O depending on external conditions such as pH or visible light. For this reason, a simple and effective method providing protection of Cu_2O-based nanostructures from oxidation is highly desirable. Parecchino *et al.* successfully improved the chemical stability of a Cu_2O layer in water by depositing multiple protective layers of Al-doped zinc and titanium oxide on the surface of it.[86,87]

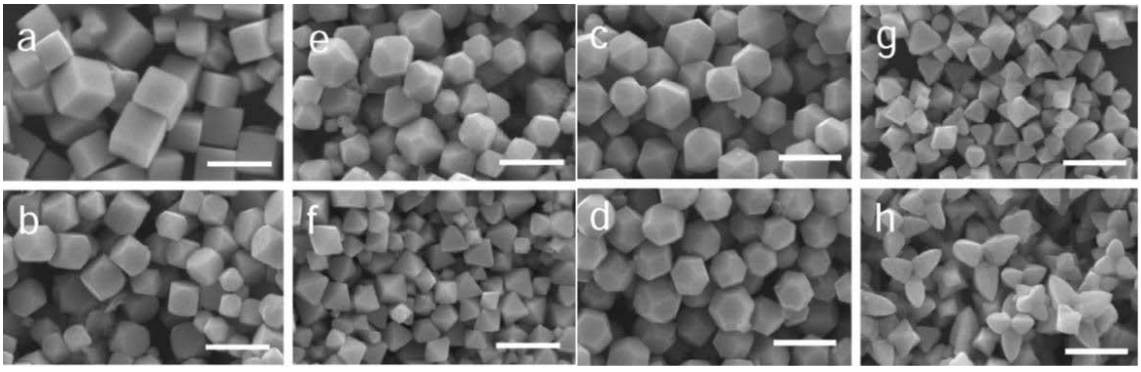

Figure 1.3.2.1 Cu_2O nanoparticles with different nanostructures. Reprinted from ref.[85] Copyright 2009 with permission from *American Chemical Society*.

Similarly, Wang's group found that both CuO and carbon can be used to protect Cu_2O films and nanofibers.[88,89] Notably, the aforementioned protection strategies have all been applied to protect one- and two-dimensional Cu_2O materials. In the regard of zero-dimensional Cu_2O nanoparticles, Yang *et al*.[90] and Su *et al*.[91] tried to synthesize $Cu_2O@SiO_2$ core-shell nanoparticles. Unfortunately the SiO_2 shell makes Cu_2O nanoparticles aggregate more easily and prevents further study on their surface properties.

To the best of our knowledge, until now little work has been reported on the synthesis of colloidal stable Cu_2O nanoparticles modified with microgels as the shells. Such functional core-shell nanoparticles will not only improve the stability of Cu_2O nanoparticles, but can also be applied as "nanoreactors" with stimuli-responsibility. In this thesis, we present for the first time the synthesis and characterization of Cu_2O@PNIPAM core-shell hybrid nanoparticles. We demonstrate that the stability of Cu_2O nanocubes is significantly enhanced by the PNIPAM shell, and the photocatalytic activity of the Cu_2O nanocubes can be tuned by temperature via the thermosensitive shell.

1.4 Applications of hybrid materials based on stimuli-responsive microgels

1.4.1 Active hybrid microgels nanoreactors

Recent results show that the catalytic reaction rate of the metallic nanoparticles immobilized inside the thermosensitive microgels does not follow a typical Arrhenius-type dependence on temperature. This demonstrates that the volume transition within the thermosensitive network can be used as a switcher to tune the catalytic reaction rate of the hybrid microgels. Lu *et. al* found that the change of the catalytic reaction rate of the silver nanoparticles immobilized inside the PNIPAM network can be divided into three regions, which result from the diffusional barrier for the reactants induced by the shrinkage of the PNIPAM networks with the increase of the temperature. [13] A similar result has been also observed by Pérez-Juste *et. al* for the catalytic activity of Au nanoparticles encapsulated in PNIPAM microgels. [92]

Moreover, the reducing of the hydrophilicity of the thermosensitive microgels with increasing temperature will also influence the catalytic activity of the hybrid microgel nanoreactors towards the particular reactants. For example, Lu and her co-workers found that the catalytic activity of oxidation reaction of benzyl alcohol is in general more sensitive to the change of polarity than the diffusional barrier caused by the volume transition of PNIPAM networks. [12]

Recently, Angioletti-Uberti *et. al* presented a theory which combined a two-state thermodynamic model with the description of the reactants' diffusion to describe the reaction

rate observed in polymer-based, stimuli-responsive catalytic nanoreactors. The theory predicts the relationship between the changing of the catalytic reaction rate of the nanoreactors and the thermosensitive property of the microgels depending on the solvation free enthalpy change at the swollen-to-collapse transition of the thermosensitive hybrid microgel nanoreactors. [93]

1.4.2 Novel ink system for inkjet printing

Inkjet printing is one of the most attractive surface patterning technologies in our daily life. Due to its advantages of low cost, efficient use of materials and scalability to large-area manufacturing, increasing attentions have been devoted to the applications of inkjet printing on fabricating optic or electronic devices, displays and sensors by directly printing conductive materials onto various functionalized substrates.[94–101] In order to obtain high resolution of the printed patterns and increase the performance of the devices, the major challenges in inkjet printing technology are to increase the stability of the ink system to attain monodispersed patterns on the substrates without aggeragation, and to obtain suitable fluid properties of the ink, such as viscosity and surface tension, which should be beneficial for the high resolution inkjet printing according to the theory identified by Fromm in 1984. [102,103]

One of the most commonly used method is to use metal precursors instead of metallic nanoparticles as the ink systems. For example, Lewis et al. synthesized particle-free reactive silver inks by a modified Tollens' process to do the inkjet printing, which is able to achieve bulk silver conductivity upon annealing at 90 °C for several times.[104] Song and his co-workers fabricated a kind of stable and colourless silver precursor ink for directly printing silver conductive patterns. [105] However, the devices obtained after the printing process from this method still require additional treatment to reduce the precursors to metallic particles, which increases the cost and makes the experiment process more complicated. In addition, the metallic species after reducing process are always the bulk ones, which cannot exhibit properties as good as the nanoparticles. Another intuitive method is to increase the viscosity of the ink by mixing different kinds of solvent, increasing the solid content of the solute or adding large amount of surfactants. [101,106] However, this method is not suitable for unstable systems which are easy to be oxidized after long term preservation. Moreover, the volatilization of the small molecules from the surfactants and the non-aqueous solvent will lead to the agglomeration of the particles during the heating treatment.

As one of the most well-known thermosensitive microgels, poly(N-isopropylacrylamide) (PNIPAM) have been used to modify inorganic nanoparticles. Due to the hydrophilic property

below lower critical solution temperature (LCST), PNIPAM shells can improve the colloidal stability of nanoparticles in aqueous solution and form an array with distance between each of the hybrid nanoparticles by drying on different substrates. [107] Because of the modification of PNIPAM shell, the viscosity of the solution will be substantially increased while the surface tension apparently decreased.[108,109] All of these improvements make it possible to use the core-shell nanoparticles solution based on PNIPAM as the novel ink system for the inkjet printing to obtain homogeneous deposition without introducing any other surfactants and solvents. Most importantly, this system should be able to be widely applied to various nanomaterials including unstable semiconductors.

2. Objectives of this Thesis

The main objective of this thesis is to synthesize two novel hybrid thermosensitive microgel systems and to explore their corresponding applications. One is the hybrid core-shell nanoparticle with Cu_2O nanocube as core and PNIPAM as shell. The Cu_2O@PNIPAM core-shell nanoparticles can be further used as photocatalysts with tunable photocatalytic activity and novel ink system to prepare gas sensor devices by inkjet printing method. The other system is the hybrid microgel based on PVCL with Au nanoparticles which shows specific/selective binding abilities to 4-nitrophenol and 2,6-dimethyl-4-nitrophenol resulting in different enhanced catalytic activity. The investigation on these novel multifunctional hybrid materials is carried out as following:

The first part of this work focuses on the synthesis of Cu_2O@PNIPAM core-shell systems. The morphology of the core-shell nanoparticles is characterized by methods of SEM, TEM and cryo-TEM. To characterize the stability of the Cu_2O@PNIPAM nanoparticles in water, XRD and NEXAFS-TXM are performed for the samples kept in water for different times. The thermosensitivity of the core-shell nanoparticles is determined by DLS measured at various temperatures.

The next part of this thesis aims at exploring the applications of Cu_2O@PNIPAM core-shell nanoparticles. The photocatalytic activity of the core-shell nanoparticles is determined by the degradation of Methyl Orange under visible light, which is performed at different temperatures. UV-vis and ESR measurements has been carried out to investigate the rate of catalytic reaction and the relevant principles. The gas sensor devices made of core-shell nanoparticles are operated at a typical elevated temperature of 300 °C and exposed to varying levels of 0.5 -10 ppm NO_2 in dry synthetic air. The sensor property is compared with the device made of bare nanoparticles. The viscosity and surface tension of the core-shell nanoparticles aqueous solution are determined by Contact Angle System and Rheological measurements. The inkjet printing method is used to obtain homogeneous deposition on the sensor devices with core-shell nanoparticles solution as the novel ink system.

Finally, the study is extended to the preparation of a new kind of nanoreactors based on poly(*N*-vinylcaprolactam) (PVCL) microgel modified with reactive α-cyclodextrins (α-CDs) to reduce Au nanoparticles in situ. A comprehensive characterization is performed to characterize the morphology and dimensional information of these hybrid microgels. The specific/selective

catalytic activity of the microgels is determined by different enhanced catalytic activity to 4-nitrophenol and 2,6-dimethyl-4-nitrophenol.

3. Theory

3.1 Thermosensitive microgels

Thermosensitive microgel is a kind of gels that the polymer network can change its volume in response to a change in temperature. The best known examples of these polymers are PNIPAM and PVCL.[6,58–61]In water solution, both PNIPAM and PVCL can exhibit a lower critical solution temperature (LCST) at about 30-35°C.[70,110–112] Below the LCST, the amide side chains of the microgels will form the hydrogen bonds with water molecules, which leads to the hydrophilic property of the microgels at low temperature. When the temperature increases, the hydrogen bonds between the microgels and water molecules become weak, which can be substituted by the intermolecular hydrogen bonds and nonpolar bonds, as shown in Fig. 3.3.1. Thus, with increasing of the temperature above the LCST, water is expelled from the microgel interior and the microgel transforms from hydrophilic to hydrophobic, which leads to the shrinkage of the microgels.[113,114]

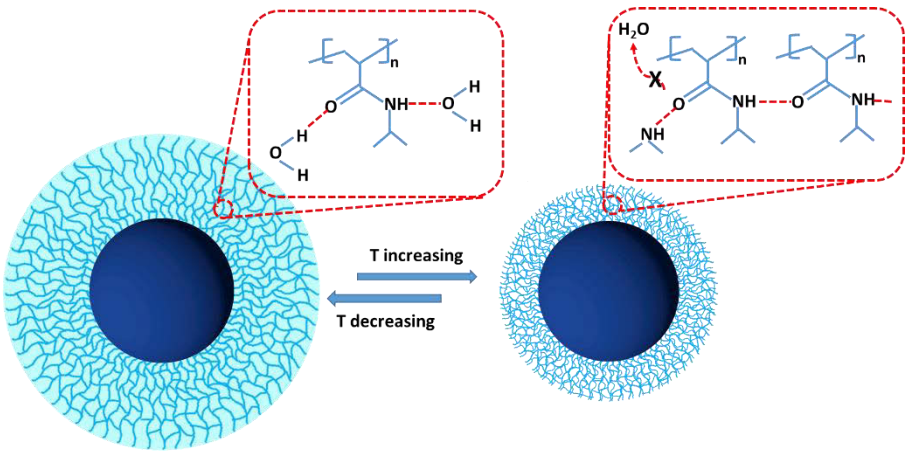

Figure 3.1.1 Swelling and deswelling behavior of the PNIPAM network below and above the LCST: the amide groups of PNIPAM can form the hydrogen bonds with water molecules below the LCST which can be substituted by the intermolecular hydrogen bonds and nonpolar bonds above the LCST.[115,116]

Besides the stimulus responsive behavior towards the temperature, thermosensitive microgels also contain several advantages over other systems, such as colloidal stability, ease of synthesis, and good control over particles size.[117] Thus, this kind of microgels are suitable for the stabilization of metallic nanoparticles. [26,30,118–122] Firstly, the colloidal stability of the immobilized metallic nanoparticles will be significantly increased and no aggregation can be observed for the hybrid systems, because of which the hybrid materials can combine the advantages of both homogeneous and heterogeneous catalysts.[123] In addition, when the

microgels are used as reactors for the immobilization of metal nanoparticles, the size of the nanoparticles can be tuned through the crosslinking degree of the microgels.[32,124] Moreover, for the sensitive nanomaterials such as Cu_2O, the modification with microgel shell can effectively protect the embeded materials from oxidation for months.[5] At last, since the thermosensitive property of the microgels is retained after the doping of the metal nanoparticles, the catalytic activity of the metal nanoparticles becomes tunable by changing the temperatures.[65]

Therefore, the use of thermosensitive microgels as carrier systems or the shells for the catalytically active metal or semiconductor nanoparticles makes it possible to obtain an active nanoreactor with tunable catalytic activity.

3.2 Catalytic applications of metal nanoparticles

Because of high surface area to volume ratio, metal nanoparticles contain a large contact area between the active material of the catalyst and the surrounding gas or liquid phase. This ensures the effective catalytic applications of metal nanoparticles.[125] Moreover, the nanosized metallic nanoparticles will show different catalytic properties from the bulk ones. For instance, Au was always considered as chemically inert[126] until Au nanoparticles (<5 nm) were found as effective catalysts. [127]

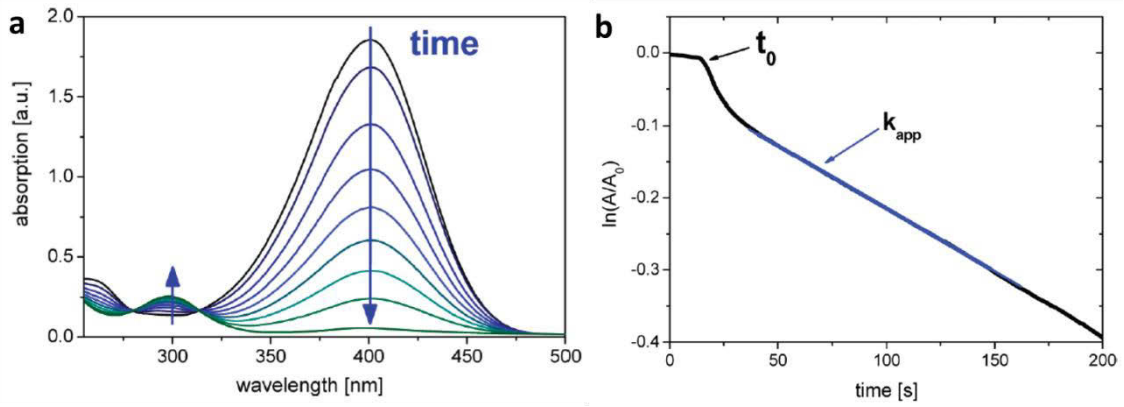

Figure 3.2.1 a) Absorption spectrum of Nip by sodium borohydride. The main peak at 400 nm (nitrophenolate ions) is decreasing with reaction time (blue arrow), whereas a second peak at 300 nm (Amp) is slowly increasing. The two isosbestic points are visible at 280 nm and 314 nm. b) Typical time dependence of the absorption of 4-nitrophenolate ions at 400 nm. The blue portion of the line displays the linear section, from which k_{app} is taken. The induction period t_0 is marked with the black arrow. Reprinted from ref[129]. Copyright 2010, with permission from *American Chemical Society*.

Among different catalytic reactions in the presence of metallic nanoparticles, the reduction of p-nitrophenol by sodium borohydride can be used as a model reaction to determine the catalytic activity of different metal nanoparticles because of its following advantages: proceeding without side reactions,[128] cannot continue without the catalyst,[129] easy to be monitored,[130–132] taking place under mild conditions, and no degradation or transformation of the metal nanoparticles occuring within the measured temperature range.

The typical evolution of the UV-vis spectra of Nip with time in the presence of Pt nanoparticles has been shown in Fig. 3.2.1a. Similar results have been also obtained for the catalytic runs with Au nanoparticles.[6] Nip shows a distinctive absorption peak at 400 nm and the p-aminophenol (Amp) exhibits a weak absorption peak at around 300 nm at high pH condition. Thus, the reduction of Nip is easily followed by UV-vis spectroscopy by the decrease of the strong absorption of Nip anion at 400 nm, leading directly to the rate constant.[133] Moreover several isosbestic points in the spectra of the reacting mixtures demonstrate that there are no side reactions and only one product is formed. If an excess of sodium borohydride is used, the reaction rate can be calculated by pseudo first order reaction from the vanishing intensity of the absorption at 400 nm.[133,134] A typical time dependence of the UV peak of 4-nitrophenolate ions at 400 nm has been shown in Fig. 3.2.1b. The generation of 4-nitrophenolate ions takes place immediately after addition of borohydride in the system. After an induction time t_0, the reaction becomes stationary and follows a first-order rate law. The apparent rate constant k_{app} can be obtained from the liner slope. Moreover, the apparent kinetic rate constant k_{app} is strictly proportional to the total surface S of all metal nanoparticles.[135–137] Hence, a kinetic constant k_1 can be defined through normalization to the total surface of the nanoparticles in the system:

$$\frac{d_{c_{Nip}}}{d_t} = -k_{app} c_{Nip} = -k_1 S c_{Nip} \qquad \textbf{(3.2.1)}$$

This rate constant, k_1, can be applied to compare the catalytic activity of different metal nanoparticles.[138]

Since the catalysis takes place on the surface of the nanoparticles, [139–143] a full analysis of the heterogeneous reduction of Nip in the presence of metallic nanoparticles has been studied by using Langmuir-Hinshelwood kinetics.[144–146]

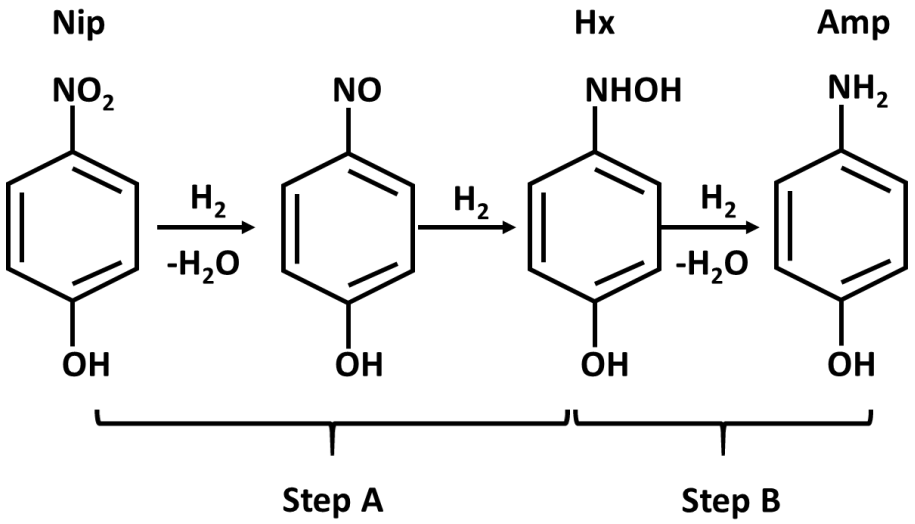

Scheme 3.2.1 Direct route of the reduction of 4-nitrophenol by metallic nanoparticles: In step A, 4-nitrophenol (Nip) is first reduced to the nitrosophenol which is quickly converted to 4-hydroxylaminophenol (Hx). This compound is the first stable intermediate. Its reduction to the final product, namely 4-aminophenol (Amp), takes place in step B, which is the rate-determining step. There is an adsorption/desorption equilibrium for all compounds in all steps. All reactions take place at the surface of the particle.

The reaction scheme of the conversion of p-nitrophenol to p-aminophenol by sodium borohydride with metallic nanoparitlces as the catalysts has been shown in scheme 3.2.1. Firstly, Nip is reduced to 4-nitrosophenol and then to 4-hydroxylaminophenol (Hx) which is the only stable intermediate during this reaction.[22,147] Hx is reduced to Amp in the final step (see scheme 3.2.1). Thus, this reaction can be modeled in two steps termed A and B: In the first step, Nip is reduced to Hx. Then Hx is reduced to aminophenol in step B. The reaction of Nip can be defined by:[129]

$$-\frac{dc_{Nip}}{d_t} = k_{app}c_{Nip} = k_a S\theta_{Nip}\theta_{BH_4} = \left(\frac{dc_{Hx}}{d_t}\right)_{source} \qquad \textbf{(3.2.2)}$$

S represent the surface area of used nanoalloys normalized by the volume of reaction solution, k_a is the reaction rate of step A normailized to *S*, θ_{Nip} and θ_{BH4} denote the surface coverage of the nanoparticles by Nip and borohydride, respectively. In the same way, the reduction of Hx in step B can be defined as:

$$-\left(\frac{dc_{Hx}}{dt}\right)_{decay} = k_b S\theta_{Hx}\theta_{BH_4} \quad \textbf{(3.2.3)}$$

Hence, with the Langmuir-Freundlich adsorption isotherm equation, we get a system of two coupled differential equations as the follows:

$$-\frac{dc_{Nip}}{dt} = k_a S \frac{(K_{Nip}c_{Nip})^n K_{BH_4}c_{BH_4}}{\left[1+(K_{Nip}c_{Nip})^n+K_{Hx}c_{Hx}+K_{BH_4}c_{BH_4}\right]^2} \quad \textbf{(3.2.4)}$$

$$\frac{dc_{Hx}}{dt} = k_a S \frac{(K_{Nip}c_{Nip})^n K_{BH_4}c_{BH_4}}{\left[1+(K_{Nip}c_{Nip})^n+K_{Hx}c_{Hx}+K_{BH_4}c_{BH_4}\right]^2} - k_b S \frac{K_{Hx}c_{Hx}K_{BH_4}c_{BH_4}}{\left[1+(K_{Nip}c_{Nip})^n+K_{Hx}c_{Hx}+K_{BH_4}c_{BH_4}\right]^2} \quad \textbf{(3.2.5)}$$

where c_{Nip}, c_{Hx} and c_{BH4} are the actual concentrations of Nip, 4-hydroxylaminophenol, and Amp, respectively. K_{Nip}, K_{Hx} and K_{BH4} are the Langmuir adsorption constants of the respective compounds. S denotes the total surface of all nanoparticles in the solution, k_a and k_b are the reaction rate of step A and step B normailized to S respectively. These two equations contain the reaction rates of the different steps as well as the adsorption constants of different components that fully define the kinetics of this reaction.

3.3 Hybrid microgels as "active" nanoreactor with tunable catalytic activity

The hybrid microgels used for the catalytic reactions can be mainly classified into two groups. One is core-shell hybrid microgels with metallic nanoparticles as the core and microgel network as the shell. The other one is the microgels filled with metallic nanoparticles, as shown in figure 3.3.1. For both systems, the microgel provides an ideal catalytic environment for the metallic nanoparticles due to its superior colloidal stability and protects metallic nanoparticles from aggregation.

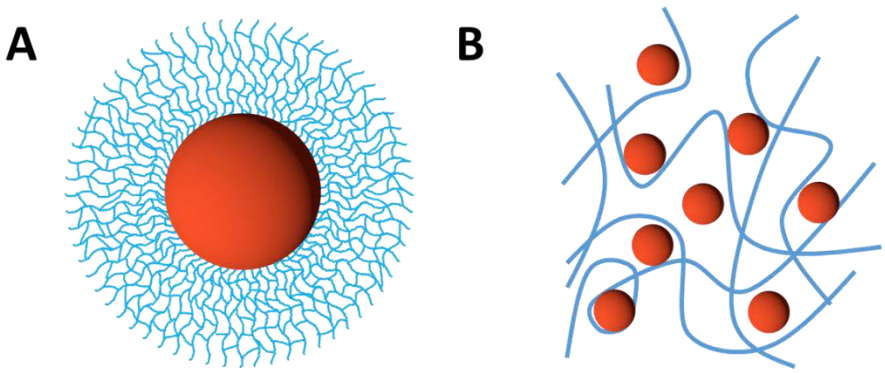

Figure 3.3.1 Schematic of the hybrid microgels used for the catalytic reactions: A) core-shell hybrid microgels with metallic nanoparticles as the core and microgel network as the shell. B) microgels filled with metallic nanoparticles.

3.3.1 Synthesis of hybrid microgels

Because of the non-dense network polymer structures and the colloidal stability, microgels can be used as a suitable carrier system for the fabrication of catalytically active metal nanoparticles, which can be considered as an active nanoreactor for different kinds of catalytic reactions.

So far, different microgel systems have been developed and applied as carrier systems for the deposition of metal nanoparticles. As shown in figure 3.3.1.1, there are a lot of free spaces in the swollen gel networks, which can provide excellent growth environment for the metallic nanoparticles without aggregation. The normal process for the in-situ synthesis of metal nanoparticles has been visualized in figure 3.3.1.1.

Firstly, the microgels with functional groups in the network can be obtained by copolymerization with variety of comonomers.[26,120] Metal ions, which are the precursors of metal nanoparticles, will be confined within the microgels by the electrostatic interaction[122,148] or the strong binding forces with the functional groups inside the microgels.[15,149] Then the reducing agent, such as sodium borohydride, hydrogen, NH_2NH_2 and so forth, is introduced and the metallic nanoparticles begin to grow in-situ inside the network of the microgels.[33,36,150,151] In the end, the hybrid microgels can be cleaned via ultrafiltration or dialysis. Different from the classic hybrid microgels, some polymers, such as poly(*N*-vinylcaprolactam) (PVCL), can not only supply the isolated reaction space for the generation of metallic nanoparticles, but also work as the reducing agent for metal precursors.[6,73] As shown in figure 3.3.1.2, amide group in the PVCL molecules can transform to enol structure with a hydroxyl group under high pH conditions.[152] After the transformation, the microgel will contain a structure similar to long-chain alcohols. This can be used as reducing agent for the synthesis of metal nanoparticles.[153,154] Compared to the traditional microgel systems, there is no need to use strong reducing agent for the formation of metal nanoparticles for this kind of microgels.

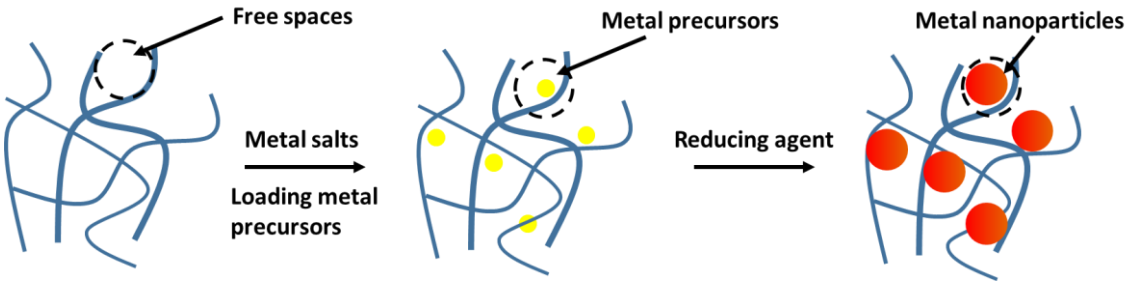

Figure 3.3.1.1 Process for the in situ synthesis of metal nanoparticles in the microgels.[6,73]

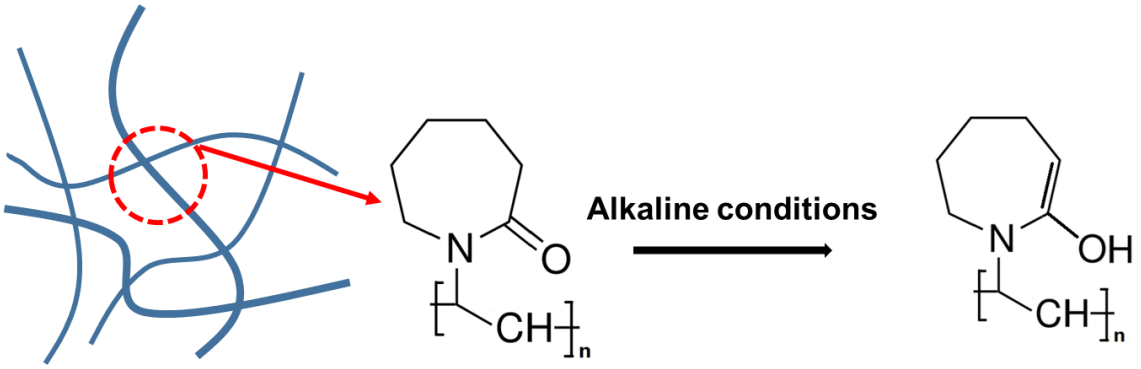

Figure 3.3.1.2 Transformation process of the structures in PVCL microgels under high pH conditions.

3.3.2 Hybrid microgels as stimuli-responsive nanoreactors

In recent years, stimuli-responsive microgels have been applied as active nanoreactors for metal nanoparticles.[12,13,31,37] Here the nanoparticles are embedded in a polymer gel that reacts to external stimuli and the reactant diffusion can be tuned by external parameters, e.g. temperature or pH, due to the phase transition of the microgel networks. Thus, the catalytic activity of the metallic nanoparticles embedded in stimuli-responsive microgels can be tuned accordingly. The best-studied examples of such hybrid microgel nanoreactors are microgels made from PNIPAM with a volume phase transition at 32°C. It has been reported that the catalytic activity of metal nanoparticles embedded in such stimuli-responsive microgels can be tuned by using temperature as the external stimulus.[13]

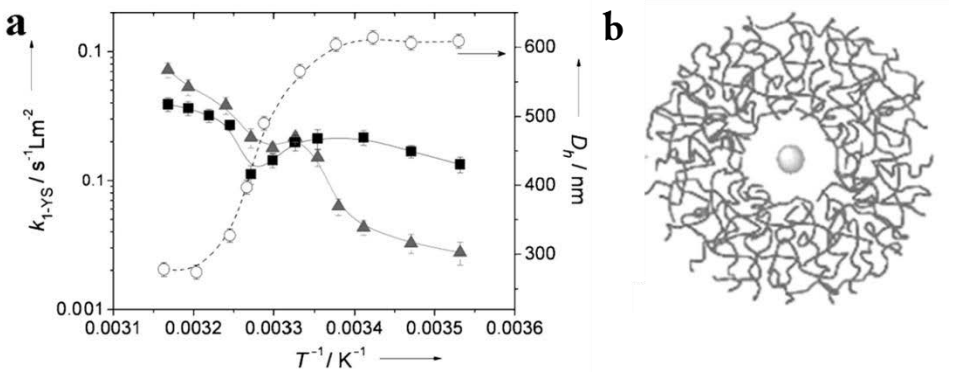

Figure 3.3.2.1 a) Arrhenius plots of the reaction rate constant k_1 (the apparent rate constant k_{app} normalized to surface area of Au nanocatalyst immobilized in the Au-PNIPAM yolk-shell carriers. Rectangles: 4-NP; triangles: NB. b) Schematic diagram of Au-PNIPAM yolk-shell nanoparticles.[12] Copyright 2012, with permission from *Wiley-VCH*.

As shown in figure 3.3.2.1, the catalytic activity of Au-PNIPAM yolk-shell particles has been measured as a function of temperature for the reductions of Nip and nitrobenzene (NB), respectively. For both of the reactants, the rate constants do not follow a simple Arrhenius law

with constant activation energy. Compared to the changing of the catalytic reaction rate of Nip by Au@PNIPAM york-shell nanoparticles as a function of temperature, the change of reaction rate for the reduction of NB is totally different. When the networks of the PNIPAM fully shrink, the reduction rate of NB increased, such that an inversion takes places from a Nip-favored reduction conditions (T<LCST) to a NB-favored reduction condition (T>LCST). Moreover, right at the LCST of PNIPAM, a local minimum rate was observed, which is similar to the results for metallic nanoparticles immobilized in PS-PNIPAM systems.[12]

The main reason of this phenomenon must be the difference between the hydrophilicity of NB and Nip.[128] Due to the hydrophobic nature of NB, the affinity of NB to the microgels was enhanced when the microgel's network became hydrophobic at high temperature. A higher number density of NB was expected in the microgels in the collapsed state, which led to the faster catalytic reaction rate. Conversely, the reactivity of the rather hydrophilic Nip is decreased when raising the temperature to the LCST of PNIPAM.

To discuss the catalytic reaction behavior based on stimuli-responsive microgels in further detail, the total reaction rate k_t, can be split into a diffusion controlled reaction rate k_D and the surface reaction controlled rate constant k_R of the free particles:[93,155]

$$k_t^{-1} = k_R^{-1} + k_D^{-1} \qquad \textbf{(3.3.1)}$$

For the microgel hybrid nanoparticles, the surface reaction rate, k_R, can be approximated by the rate constant measured on the free particles without influence of the microgels and the diffusion controlled rate, k_D, can be given by the Debye-Smoluchowski expression:[155]

$$k_D{}^{-1} = \int_{R_{np}}^{\infty} \frac{\exp[\beta \Delta G_{sol}(r)]}{4\pi c_0 D(r) r^2} dr \qquad \textbf{(3.3.2)}$$

where R_{np} is the radius of nanoparticles embedded in stimuli-responsive microgels, $\beta=1/k_BT$ is the thermal energy, $D(r)$ is the distance-dependent diffusion constant, $\Delta G_{sol}(r)$ is the local free enthalpy and c_0 is the concentration of reactant in the bulk solution.

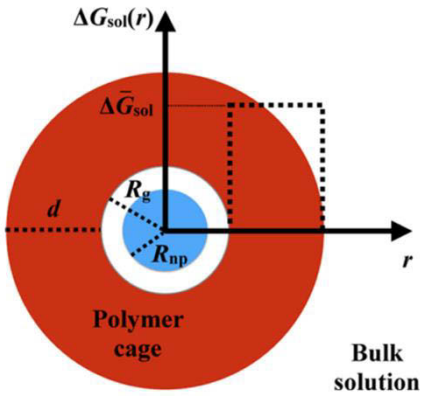

Figure 3.3.2.2. Schematic representation of a yolk-shell nanoreactor. At center core of the nanoreactor sits a metal nanoparticle (blue) of radius R_{np}, embedded in a spherical polymer shell of inner radius R_g and outer radius R_g+d. The reactants have to overcome a solvation free-enthalpy barrier $\Delta G_{sol}(r)$ to reach the nanoparticle depicted by the dotted lines. Copyright 2015, with permission from *American Chemical Society*.

As shown in fig.3.3.2.2, for the yolk-shell nanoreactors, $\Delta G_{sol}(r)$ is $\Delta \bar{G}_{sol}$ inside the polymer shell and zero otherwise. Thus, the eq 3.3.2 can be simplified as the follows:

$$k_D{}^{-1} = \int_{R_{np}}^{R_g} \frac{1}{4\pi c_0 D_0 r^2} dr + \int_{R_g}^{R_g+d} \frac{\exp[\beta \Delta \bar{G}_{sol}]}{4\pi c_0 D_g r^2} dr + \int_{R_g+d}^{\infty} \frac{1}{4\pi c_0 D_0 r^2} dr \quad \textbf{(3.3.3)}$$

We assume in the following that the reactants have a diffusion constant inside the gel D_g that is much smaller than in the bulk, that is $D_g \ll D_0$, one can further simplify eq 3.3.3 as[12]

$$k_D = 4\pi D_g c_0 R_g \exp(-\beta \Delta \bar{G}_{sol}) \quad \textbf{(3.3.4)}$$

Here, terms of order $1/(R_g+d)$ have been neglected inasmuch as R_{np} and R_g are typically considerably smaller than R_g+d. Since $\Delta \bar{G}_{sol} = \Delta \bar{H}_{sol} - T\Delta \bar{S}_{sol}$, the logarithm of the diffusion controlled rate constant k_D is given by

$$\ln[k_D] = \ln\left(4\pi D_g c_0 R_g\right) + \frac{\Delta \bar{S}_{sol}}{k_B} - \frac{\Delta \bar{H}_{sol}}{k_B T} \quad \textbf{(3.3.5)}$$

Thus, the equation demonstrates that the changes in diffusion rate are governed by the following two terms:[128] first, compared to the bulk solution, the diffusion of the reactants through the network is slowed down since $D_g < D_0$. Second, the changes of the transfer free energy $\Delta \bar{G}_{sol}$ will have a profound influence on the measured temperature dependence. Hence, the transfer entropy $\Delta \bar{S}_{sol}$ determines the intercept of the Arrhenius plot of k_D while the slope will be dominated by the respective enthalpy $\Delta \bar{H}_{sol}$ of the solute from the bulk into the network. Moreover, if $R_g=R_{np}$, the above model can be also applied to the core-shell systems.

3.4 Photocatalytic mechanism of Cu_2O

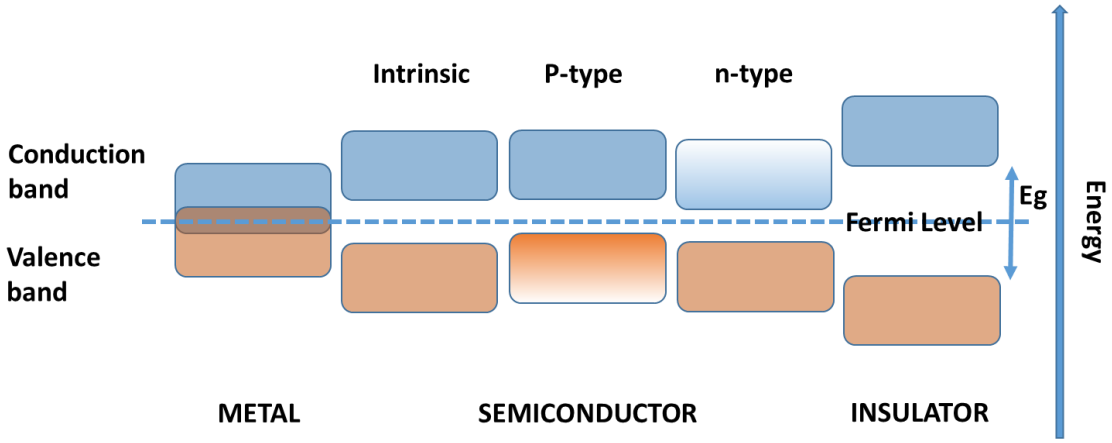

Figure 3.4.1 Electronic band structures of metal, semiconductor, and insulator indicating the Fermi level. The blue band is conduction band, the brown band is valence band, the dotted line is Fermi level and the *Eg* is energy band.

The intrinsic semiconductor is the semiconductor containing only one element or one compound which behaves as insulator at 0 K. When this kind of semiconductor is doped with acceptor atoms, p-type semiconductor will be produced. Because these atoms can take electrons from valence band by being reduced, the majority carriers are the positive holes. Correspondingly, n-type semiconductors are the semiconductors doped with donor impurities which provide electrons to the conduction band. Thus, for the n-type semiconductor, the majority carriers are the electrons. In addition, Fermi level will also shift because of the different impurities. The schematic of different kinds of semiconductors have been shown in Figure 3.4.1.

Because of oxygen excess exhibited as copper vacancies, which introduces the holes states and a stoichiometry defect of copper ion vacancies, cuprous oxide (Cu_2O) is considered as a prototypical p-type material. Due to the different synthesis process, the band gap of Cu_2O is from 1.8 eV to 2.2 eV.[156] Therefore, when the energy of photons is higher or equal to the band gap energy of Cu_2O, the photons can be absorbed.

If E_g represents the minimum energy of the photon which can be absorbed by the semiconductor, we can get the spectral absorption limit of Cu_2O from 688 nm to 563 nm according to the Planck-Einstein relation. It means the light, of which the wavelength is less than 688 nm or 563 nm, can be absorbed by Cu_2O.

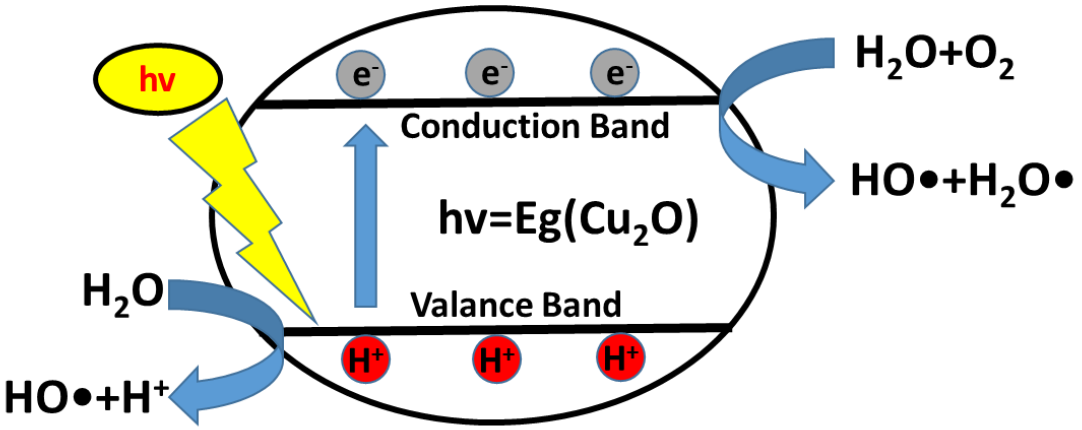

Figure 3.4.2 Schematic diagram of the production process of the hydroxide radicals by Cu_2O under visible light.

When the photons were absorbed by Cu_2O, the electrons (e^-) from the valence band (VB) transferred to the conduction band (CB) generating a hole (h^+) in the VB. In water solution, electrons transfer from water molecule to the positive holes to produce OH• radicals which are powerful oxidants and react with organic and toxic compounds.[76,85,157,158] The production process of the hydroxide radicals by Cu_2O has been shown in Figure 3.4.2.

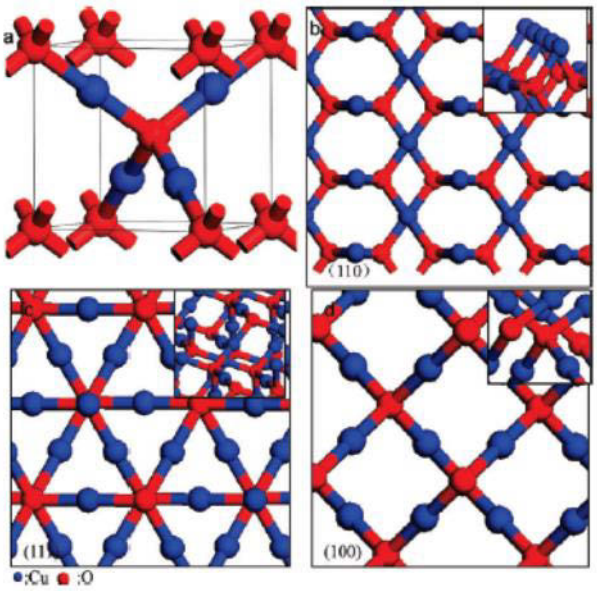

Figure 3.4.3 a) The unit cell of the cuprous oxide Cu_2O and (b-d) the atomic arrangements in the (110) b), (111) c), and (100) d) planes of the Cu_2O structure, repectively. The inset in each graph is the three-dimensional model of the terminated layer structure. Reprinted from ref[159]. Copyright 2010, with permission from *American Chemical Society*.

Moreover, the photocatalytic mechanism of Cu_2O is also closely associated with the surface crystal structures of Cu_2O nanomaterials and the charge of the reactants. For Cu_2O, each O is surrounded by a tetrahedron of Cu, and each Cu has two O neighbors.

Figure 3.4.3c shows that {111} planes with Cu dangling bonds are positively charged, which is similar with {110} planes in Figure 3.4.3b. On the contrast, the {100} planes contain 100% saturated oxygen bonds and thus are electrically neutralized.[77,84,85,157,160,161]

When the reactant is negatively charged, such as Methyl Orange (MO), the positively charged {110} and {111} facets should interact more strongly than {100} facets.[159] If the reactant is positively charged, such as Methylene Blue (MB), the reaction rate will be obviously decreased compared with negatively charged reactant as there is no attractive interation between reactant and crystal facets of Cu_2O nanoparticles, Considering that different Cu_2O nanomaterials will contain different crystal facets, the reaction rate should be quite different (see figure 3.4.4) when the Cu_2O nanomaterials with different nanostructures are used as the photocatalysts for the same reaction.

In the case of Cu_2O nanocubes, all of the crystal surfaces of Cu_2O nanocube belong to {100} facets, it has been demonstrated that it contains almost no photocatalytic activity when used as photocatalyst for the decomposition of negatively charged organic dye molecules.[159]

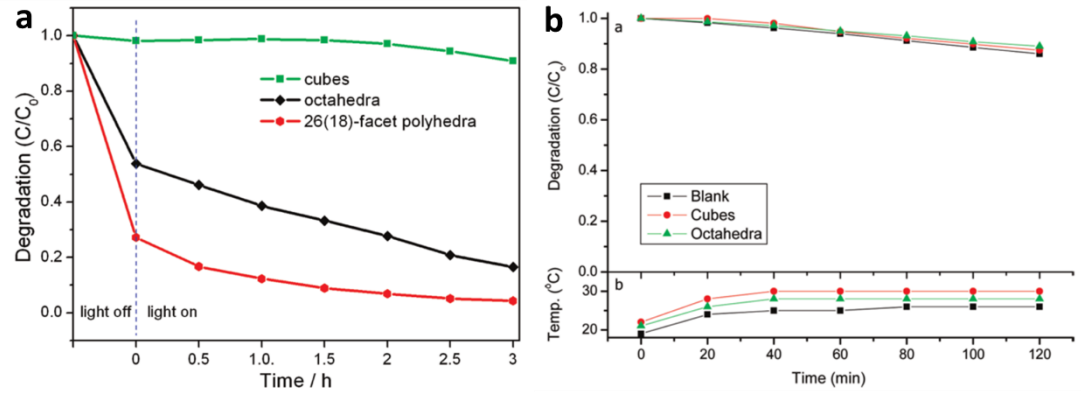

Figure 3.4.4 a) The curves of adsorption and photodegradation of MO by Cu_2O 26(18)-facet polyhedral, octahedral, and cubes, respectively. b) A plot of the extent of photodegradation of methylene blue vs. time for the Cu_2O cubes and octahedral is shown. The blank sample did not contain Cu_2O crystals but only the methylene blue solution. Reprinted from ref [85]. Copyright 2009, with permission from *American Chemical Society.*

3.5 Gas sensor mechanism of CuO

Based on the constitutional principle of sensor devices, the semiconductor gas sensors can be classified into five types: resistor, diode, metal-insulator-semiconductor capacitor, metal-insulator-semiconductor field effect transistor and oxygen concentration cell. Compared with the other four types, resistor semiconductor gas sensor is the most commonly used type at the moment and is also the only type successfully applied on the market at present. For the resistant semiconductor gas sensor, the host semiconductor can directly or indirectly supply or accept electors to or from the gases, which will influence the resistant of the semiconductor materials. As a kind of p-type semiconductor, CuO can also be used as the gas sensor materials and the mechanism of CuO gas sensor includes two steps.

Firstly, when CuO gas sensor device is placed in air, oxygen can be adsorbed on the surface of CuO in the form of O^- by the following reactions.

$$\frac{1}{2}O_2 + S_A \rightarrow O^- + h^+ \qquad \textbf{(3.5.1)}$$

where O_2 represents oxygen atmosphere, S_A means an adsorption site for oxygen, O^- is the adsorbed O anion and h^+ is the created hole in the CuO valence band. Due to the production of the holes, the resistant of CuO is decreased until the adsorption equilibrium.

Then the testing gases will react with the O^- and the resistant of the device will be changed accordingly, which can be used as the gas sensor signals. For the reducing testing gases, such as CO, O^- will react with CO and the released electron will combine with vacancy again as shown in equation 3-2, which will result in the decrease of the vacancies and the increase of the resistant of CuO.

$$\mathrm{CO} + O^- + h^+ \rightarrow CO_2 + S_A \qquad \textbf{(3.5.2)}$$

On the other hand, for the oxidizing gases, such as NO_2, more electrons will be consumed and the conductivity of the CuO device will be increased with the resistance of the device decreased at the same time (see equation from 3-3 to 3-6).[162]

$$NO_2 + e^- \rightarrow NO_2^- \qquad \textbf{(3.5.3)}$$

$$NO_2^- + O^- + 2e^- \rightarrow NO + 2O^{2-} \qquad \textbf{(3.5.4)}$$

$$\mathrm{NO} + e^- \rightarrow NO^- \qquad \textbf{(3.5.5)}$$

$$2NO^- \rightarrow N_2 + 2O^- \qquad \textbf{(3.5.6)}$$

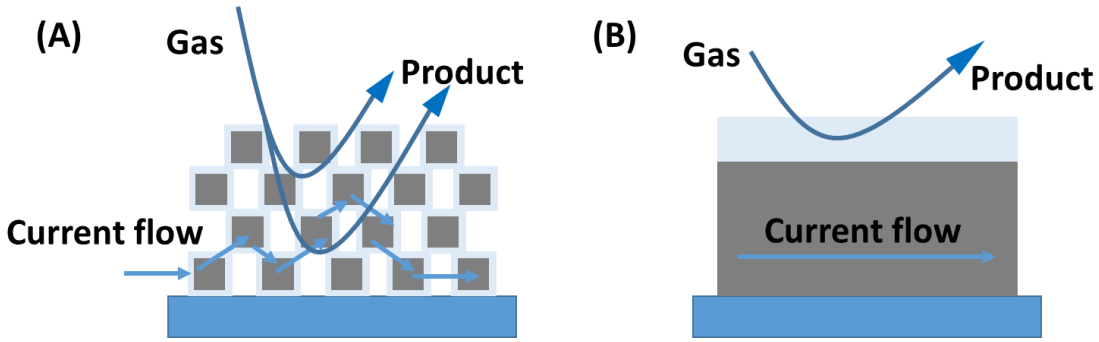

Figure 3.5.1 Schematic of gas interaction and flow of current in different kinds of CuO gas sensors: A) CuO nanoparticles. B) CuO bulk materials.

Except the intrinsic characteristics of CuO, the morphology of the materials can also impact on the gas sensor properties. As shown in Figure 3.5.1, for the bulk CuO gas sensor device, gas interaction only takes place on the surface of the materials and the flow of current is hardly influenced by the resistance changing from the surface of the materials. On the contrary, for porous layers in Figure 3.5.1A, the gas can flow into the entire layer and the resistance of every CuO nanoparticles will be affected by the testing gases. Because the current is forced to flow by passing from one particle to the next, the resistance changing of each CuO nanoparticle will directly influence the whole gas sensor device's resistance. That is why the porous gas sensor devices are always more sensitive than the bulk ones.[163]

3.6 Inkjet printing

Inkjet printing is a material's conservation and deposition technique only used for liquid phase materials, of which the solute can be dissolved or dispersed in a solvent. The use of inkjet for the direct deposition of metal nanoparticles and various other materials not only reduces the cost of materials, but also eliminates the time-consuming production steps. Moreover, this technology allows a required pattern on various substrates, such as MEMS sensing chips and so on.[96–99,103,164] The main properties affecting the printing result of using inkjet printing for the deposition of nanodispersions are the parameters of the printer and the ink properties.

3.6.1 Printer parameters

A piezoelectric inkjet system uses a piezoelectric material to convert applied externally electrical energy into mechanical deformation of an ink chamber. For this printing method, the following printer parameters will affect the printing quality of using nanoparticles solution as the ink. Firstly, the piezoelectric displacement is proportional to the applied voltage and larger voltage will induce stronger pressure waves and fluid accelerations. Hence above the critical

voltage value, which is the minimum value to eject the drop, both the volume and velocity of the droplets increase with voltage if all other parameters are kept constant.

Secondly, the size of the nozzle is another driving parameter of the printer influencing the printing quality. The smaller the nozzle size is, the smaller the droplets will be obtained when the other parameters are kept unchanged. However, if there are nanoparticles dispersed into the ink, the diameter of the nozzle should be at least 20 times larger than the nanoparticles, which will prevent the clogging. [102] At last, the distance between the nozzle and the substrate should be larger than the minimum distance, which can be defined as the minimum stand-off distance, that the drop needs to transform into a single droplet after ejected from the nozzle. But a longer minimum stand-off distance will lead to unstable and inaccurate deposition for the ink-jet printing. Thus, a proper ink system is indispensable for high-quality printing.

3.6.2 Ink property

The important ink properties include viscosity, density and surface tension, which can influence the drop formation mechanism and subsequent drop size at a given voltage. The inverse (Z) of the Ohnesorge number can be defined to represent the fluid ink physical properties which is independent of fluid velocity.[165]

$$Z = \frac{\sqrt{a\rho\gamma}}{\eta} = Oh^{-1} \qquad \textbf{(3.6.1)}$$

where a is the radius of the printing orifice, ρ is the density of the ink, γ is the surface tension of the ink, and η is the viscosity of the ink.

Although for different ink materials, the jettability range of Z is different, the printable range of Z is normally considered within $1<Z<14$ [164]. If the value of Z is too high, a large number of satellite droplets will be formed, whereas if it is too low, the ink will need more energy to form a new drop near the nozzle tip, which will prevent the separation of a drop. According to literature [103], for the same ink system, the Z value of the ink is closer to the maximum value of the printable range, it is easier to form single droplets at higher frequencies and the travel velocity of the droplet will be increased, because of which the minimum stand-off distance between the nozzle and the substrate (MSD) will become shorter and the positioning error of the printing process will become smaller.

For different printing systems, the requirements for the Z value of the ink are different. In this thesis, in order to obtain a gas sensor device with multi uniform layers of particles and save the materials as much as possible at the same time, a kind of ink with high Z value but low materials

loading is highly needed. Considering that the PNIPAM shell can not only increase the viscosity of the ink, but also enhance the colloid stability of the nanoparticles, the nanoparticles with PNIPAM shells should be an ideal ink system for the gas sensor inkjet printing.

4. Cu_2O@PNIPAM core-shell nanoparticles

4.1 Synthesis and Characterization of Cu_2O@PNIPAM core-shell nanoparticles

Due to the sensitive properties of Cu_2O nanoparticles which can form complexes with many chemical groups, such as amino-group, and can be easily etched by the changing of pH conditions, it is very difficult to coat polymer on the surface of Cu_2O nanomaterials. Thus there's lack of knowledge for the synthesis of colloidal stable Cu_2O nanoparticles with PNIPAM shell. In this part of the thesis, we present for the first time the synthesis and characterization of Cu_2O@PNIPAM core-shell hybrid nanoparticles. The related properties of the Cu_2O nanoparticles can be enhanced or tuned by the PNIPAM shell accordingly.

4.1.1 Fabrication of Cu_2O nanoparticles

4.1.1.1 Cu_2O nanocubes

Cu_2O nanocubes were initially synthesized by the seed-mediated method.[166] Since the {100} crystal planes have minimum energy state and Cl^- can be used to stabilize {100} planes, $CuCl_2$ solution was used for the fabrication of Cu_2O nanocubes. In order to obtain cubic nanoparticles with better morphology, NaOH solution was used to slow down the growth rate of the Cu_2O nanoparticles by forming $Cu(OH)_4^{2-}$ to decrease the reduction rate of Cu_2O.[167] By controlling the size of the seeds for the growing steps, Cu_2O nanocubes with different scales were obtained as shown in Figure 4.1.1.1.

Except sample A and sample B, all of the other Cu_2O nanoparticles contain the cubic shapes and some small sections were found at the corners of the Cu_2O nanocubes due to the stabilization from sodium dodecyl sulfate (SDS) on the {111} facets which has been reported recently.[68] With increasing the size of the seeds, the scales of the Cu_2O nanocubes increased from 24 nm to 314 nm. The size of the particles was measured based on their TEM images by counting more than 100 particles (A: 24.7±4.6 nm, B: 32.6±6.6 nm, C: 36.1±5.9 nm, D: 104±8.4 nm, E: 259±19 nm and F: 314±92 nm). For sample A and sample B, since the size of the seeds used for the growing process is too small, it is hard to obtain Cu_2O nanocubes after 2 hour growing process. Also the small particles prefer to aggregate together instead of growing into cubic structures, which can be seen from TEM images in Figure 4.1.1.1. When the size of the seeds used for the growing process is increased, cubic shapes can be obtained (see Figure 4.1.1.1c to f). However, if the size of the seeds used for the growing process is too big, the amount of Cl^- and SDS in the system is not enough to control the growing speed of all of the particles due to large surface area, because of which the size distribution of the particles become

un-uniform (see Figure 4.1.1.1f). Considering that the cubic structures and the size of the particles have close relationship with the properties of the Cu_2O nanoparticles and are quite important for the PNIPAM coating process, sample E has been chosen as the cores for the PNIPAM modification.

The XRD patterns of the as-prepared Cu_2O nanocubes are presented in Figure 4.1.1.2 a. The peaks at 2θ= 29.63°, 36.50°, 42.40°, 61.52°, 73.70° and 77.57° correspond to the Bragg reflections of Cu_2O nanocrystals at {110}, {111}, {200}, {220}, {311}, and {222} facets, indicating the production of fresh Cu_2O. The size distribution of Cu_2O nanocubes from sample E has been shown in Figure 4.1.1.2b. By counting hundreds of paritcles in the TEM image, the average size of Cu_2O nanocubes from sample E is 259±19 nm. The formation of the Cu_2O nanoparticles can be followed by the change of color in the solution and the UV-vis spectra. As shown in figure 4.1.1.3, with the formation of Cu_2O nanocubes, the color of the solution changed from light blue to orange and an absorption band can be observed at around 515 nm in the UV-vis spectra of Cu_2O nanocubes solution. The absorption band in the red and near-infrared regions comes from the light scattering of the large Cu_2O nanocubes.[168]

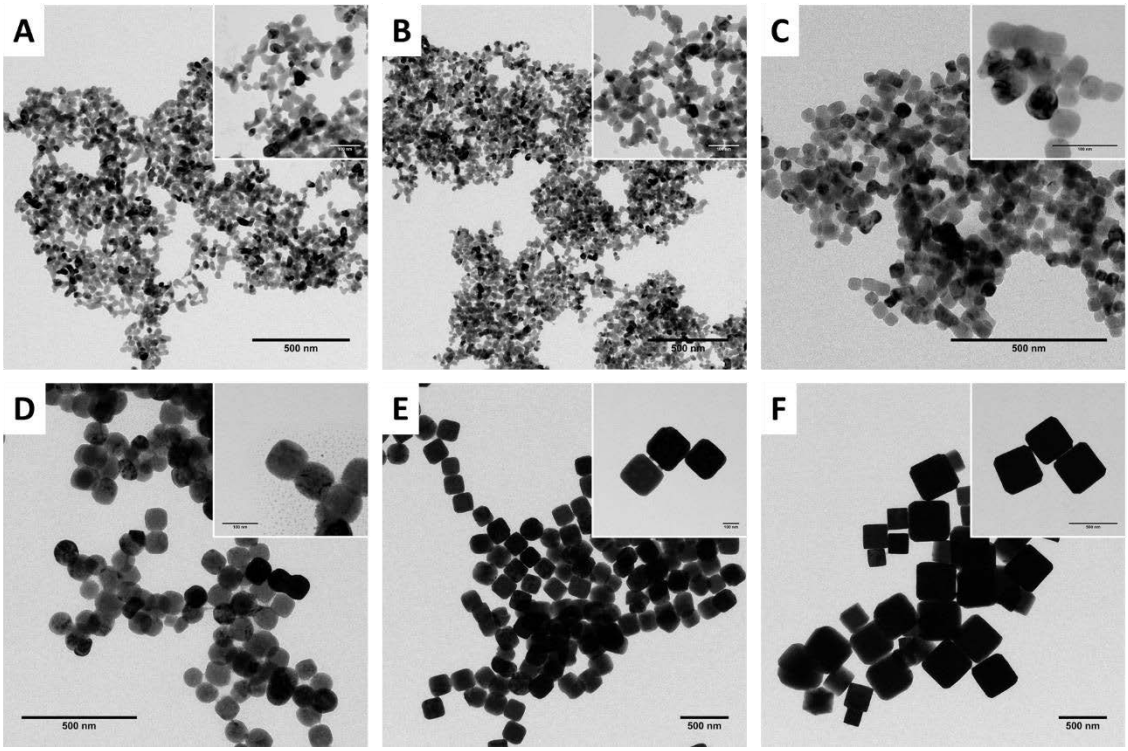

Figure 4.1.1.1 TEM images of Cu_2O nanoparticles from sample A to sample F.

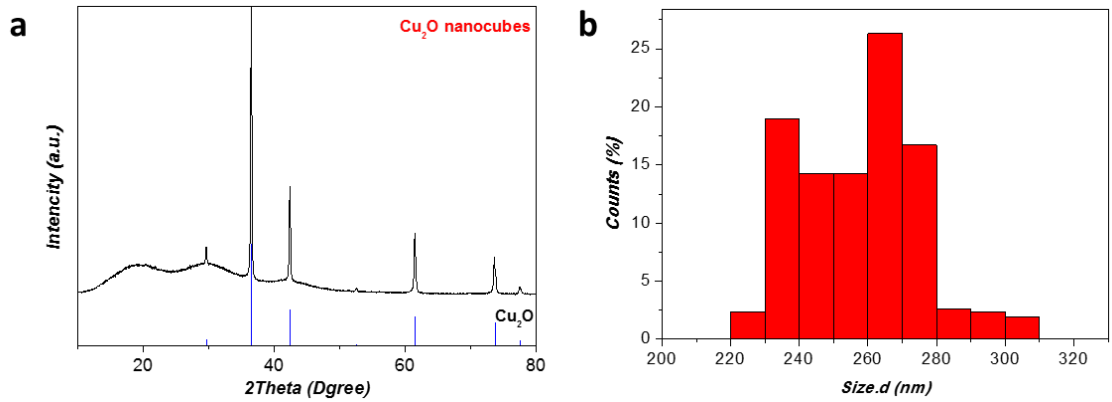

Figure 4.1.1.2 (a) XRD pattern and (b) size distribution of Cu_2O nanocubes measured from the TEM image by counting more than 100 particles.

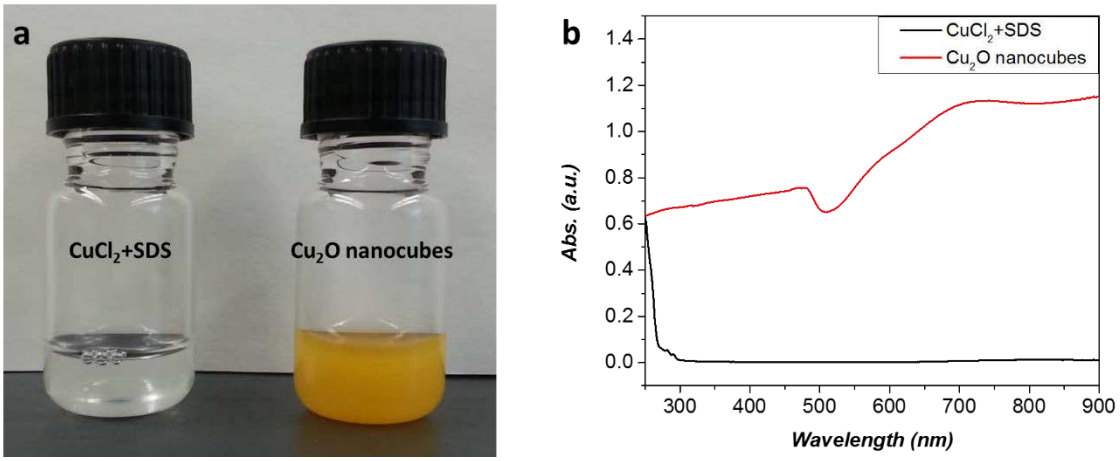

Figure 4.1.1.3 (a) the photo of $CuCl_2$-SDS solution (left) and Cu_2O nanocubes solution (right). (b) UV-vis spectra of $CuCl_2$-SDS solution (low) and Cu_2O nanocubes solution (up).

4.1.1.2 Cu_2O nanospheres

The synthesis of Cu_2O nanospheres relies on a precipitation reaction as shown in Figure 4.1.1.4. By using PVP as the surfactant and N_2H_4 as the reducing agent, Cu_2O nanospheres can be obtained by the aggregation of the Cu_2O nucleis. The changing of the color from blue to orange indicates the generation of the Cu_2O nanoparticles. The UV-vis spectra of the sample has been shown in Figure 4.1.1.6, with the generation of Cu_2O nanospheres, an aborption band at around 468 nm can be observed.

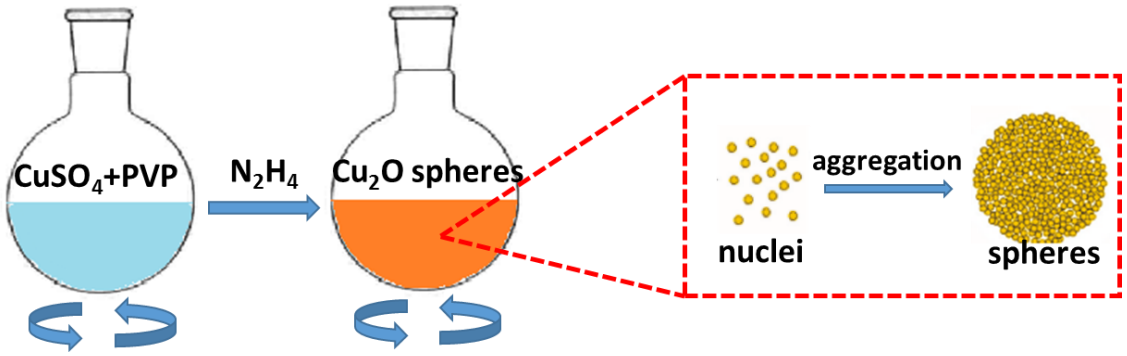

Figure 4.1.1.4 The synthesis process of Cu_2O nanospheres.

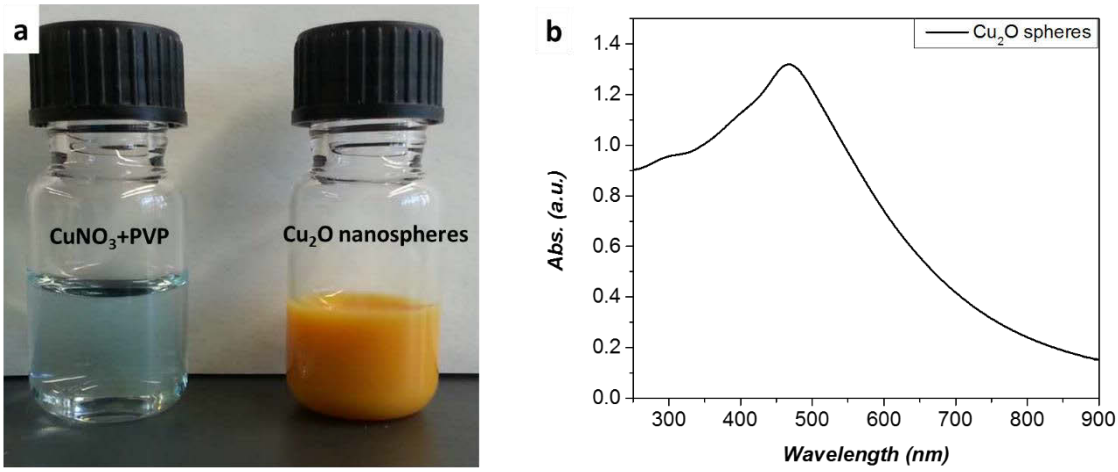

Figture 4.1.1.5 (a) The photo of Cu_2NO_3-PVP (left) and Cu_2O nanospheres solution. (b) UV-vis spectra of Cu_2O nanospheres solution.

As a surfactant, PVP could act not only as a stabilizer to prevent the aggregation of the products but also a shape-controller to influence the formation of different kinds of Cu_2O crystals structures. It is reported that PVP preferred to be adsorbed on the {111} planes of Cu_2O and decreased the surface energy of it, which leads to the lower growth rate of {111} planes compared with {100} planes.[169,170] Since the crystal structures is determined by the planes with the slowest growing speed, when the amount of PVP used during the reaction is limited in the range of 0.5 -1.5 mM, Cu_2O will grow into truncated cubes or octahedral structures.[66] However if continue to increase the amount of PVP in this synthesis process, owing to the high coverage of PVP on all planes of the Cu_2O nanocrystals, spherical particles will be generated. In addition, by using N_2H_4 as the reducing agent, the nucleation of Cu_2O was very fast and the PVP acted as a structural directing agent to mediate aggregation of the seeds particles into solid spheres. The SEM images and size distribution of the Cu_2O nanospheres with different amount of PVP

have been shown in Figure 4.1.1.6. When more PVP was used in the experiment, the size of the Cu_2O nanospheres became smaller and the size distribution became broader.

More PVP used during the synthesis process of Cu_2O nanospheres will lead to an isotropic growth mode and loose spherical particles due to the protection effect of PVP around the small Cu_2O nanoparticles, which makes the agglomeration of the Cu_2O small particles more difficult. As shown in Figure 4.1.1.7, when the amount of PVP was increased from 0.2g to 0.5g, the size of the Cu_2O nanospheres became smaller[171] and the surface of the Cu_2O nanospheres became rougher (see the insert images in Figure 4.1.1.7).

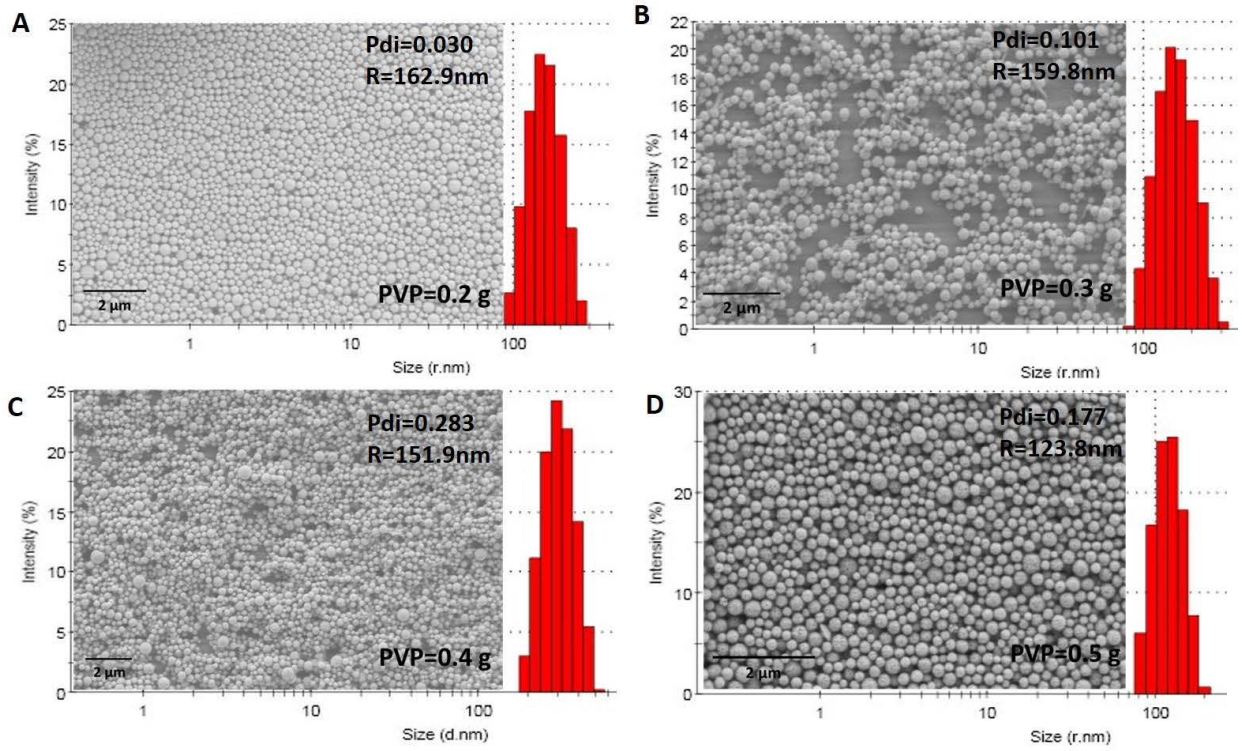

Figure 4.1.1.6 SEM images and size distribution of Cu_2O nanospheres from DLS with different amount of PVP.

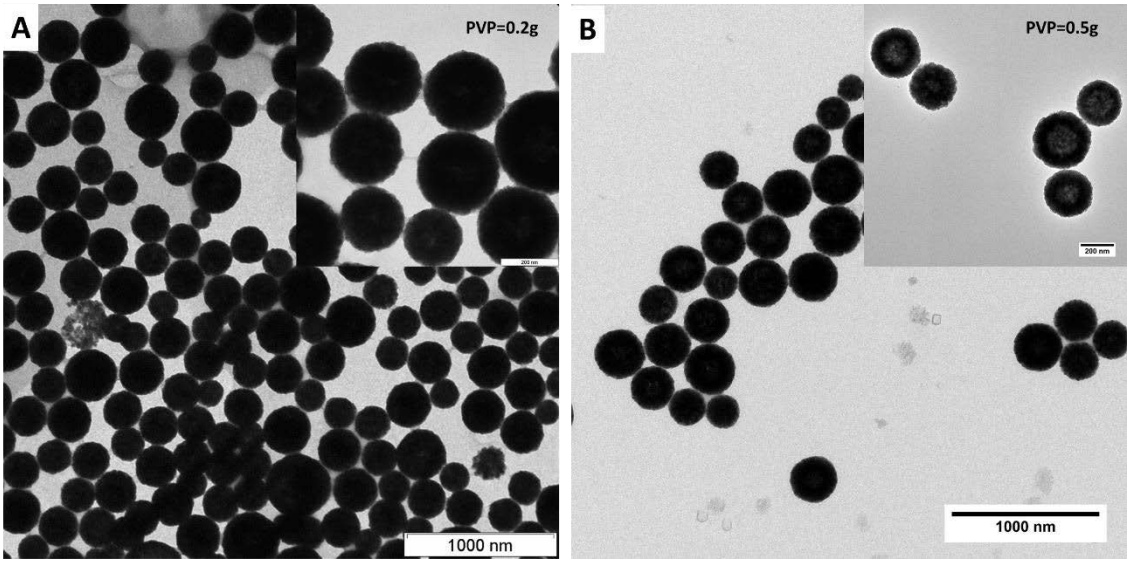

Figure 4.1.1.7 TEM images of Cu_2O nanosphere with different amount of PVP: (A) 0.2g PVP, (B) 0.5g PVP.

Because of the sensitive property, Cu_2O is quite easy to be oxidized to CuO in water. During this transformation process, the crystal structure of the nanoparticles will be changed and the regrowth of the crystal will happen. Since Cu_2O nanospheres are made up of many small particles, in the oxidation process, the reorganization of the crystal structure will occur in each of the small particles, which will lead to anisotropic growth for the nanospheres. Thus, the CuO nanoparticles with anisotropic structures will be obtained. As shown in Figure 4.1.1.8b, by keeping the Cu_2O nanospheres in water for 30 hours, needle-like structures began to appear on the surface of the spheres. After being stored in water for 50 hours, urchin-like nanoparticles replaced the nanospheres in the system. (see Figure 4.1.1.8c) The XRD patterns for both fresh Cu_2O nanospheres and CuO urchin-like nanoparticles have been shown in Figure 4.1.1.8d. When all of the nanospheres have transformed into urchin-like nanoparticles, the characteristic peaks of Cu_2O disappeared and the peaks at $2\theta=32.5^{o,}$ 35.5^{o}, 38.66^{o} and 48.8^{o} corresponding to the Bragg reflections {110}, {002}, {111}, and {202} of CuO have been observed.

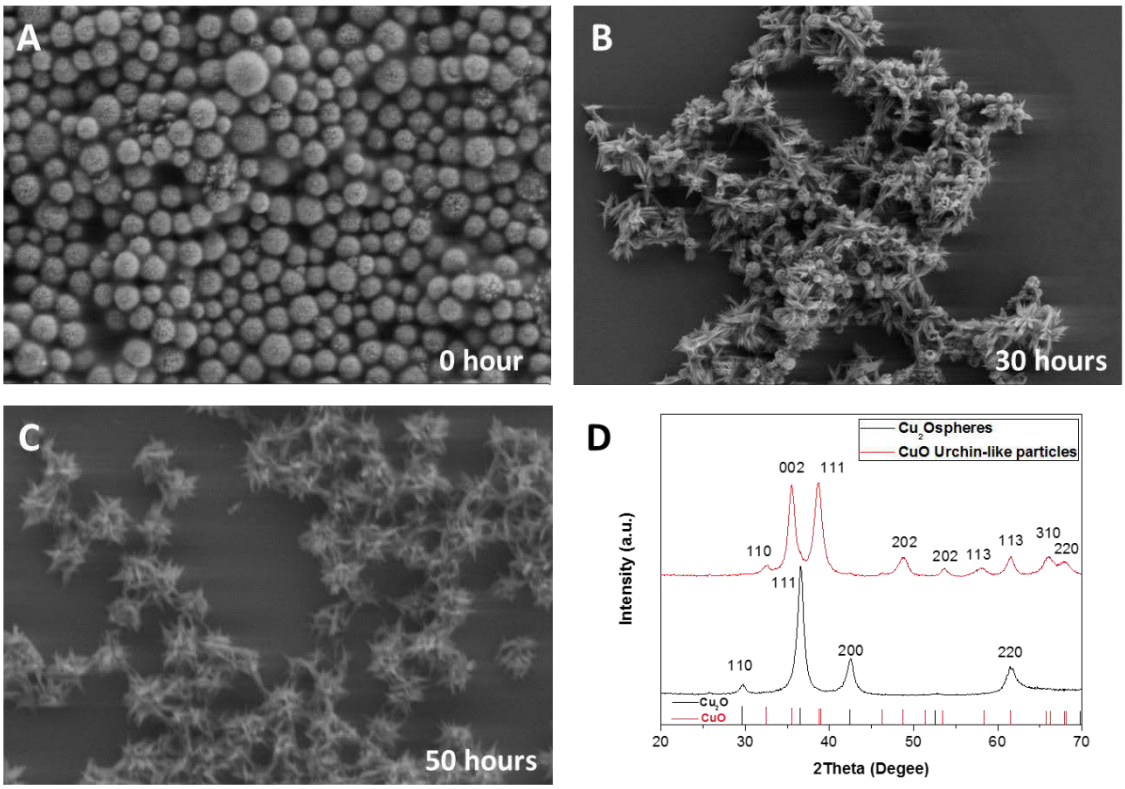

Figure 4.1.1.8 SEM images of (A) fresh made Cu_2O nanospheres, (B) Cu_2O nanospheres kept in water for 30 hours and (C) for 50 hours. (D) XRD patterns of fresh Cu_2O nanospheres and CuO urchin-like nanoparticles.

4.1.2 Synthesis of Cu_2O@PNIPAM core-shell nanoparticles

Until recently, there's lack of knowledge about colloidal stable Cu_2O nanoparticles. The modification of PNIPAM shell onto Cu_2O nanocubes will not only protect Cu_2O nanocubes from oxidation, but also increase the colloidal stability of Cu_2O nanocubes in the water solution. Moreover, such core-shell nanoparticles will be essential to understand the effect of PNIPAM shell on the properties of semiconductor nanomaterials.

The conventional method of PNIPAM coating on the surface of inorganic cores is based on the modification with SiO_2 or polystyrene shell as the interlayer.[20,92,172] Then coupling agents will be functionalized on the surface of the particles and makes it possible for the chemical coupling between PNIPAM network and inorganic nanoparticles. Thus we have first tried to do the SiO_2 coating around the Cu_2O nanoparticles for the PNIPAM modification.

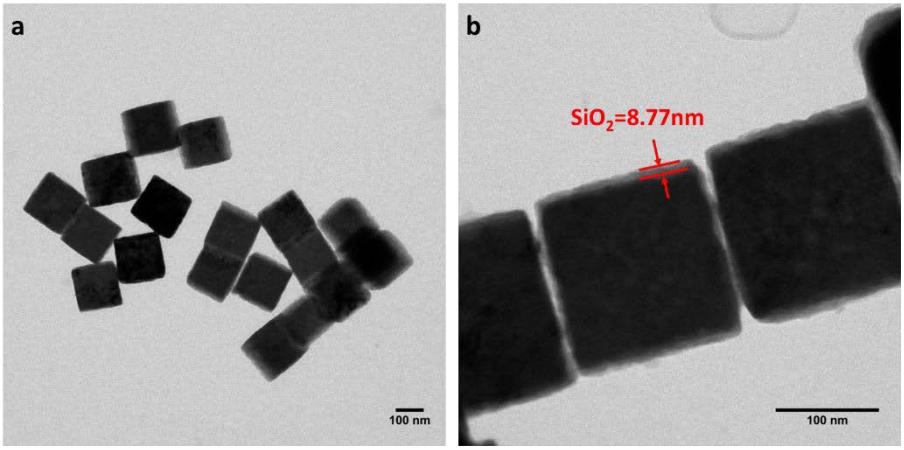

Figure 4.1.2.1 TEM images of Cu_2O nanocubes with thin SiO_2 layers.

Considering that Cu_2O is easily to be oxidized and its nanostructure can be destroyed depending on external conditions such as pH or visible light, a mild method was first tried to modify a thin SiO_2 layer on the surface of Cu_2O nanocubes. As shown in 4.1.2.1, a thin SiO_2 layer with thickness around 8 nm has been modified on the surface of Cu_2O nanocubes and the cubic structures were well maintained.

In order to increase the thickness of the SiO_2 shell for the functionalizing of coupling agent, the Cu_2O nanocubes with thin SiO_2 shells were used as the seeds for the growing of SiO_2 layers by using ammonia to adjust pH conditions and tetraethyl orthosilicate (TEOS) as the precusor of the SiO_2. As shown in Figure 4.1.2.2, although there was a thin SiO_2 layer to protect Cu_2O, the cubic structure of Cu_2O were still etched and the nanostructures of Cu_2O have been destroyed during the SiO_2 coating process due to the reactions between Cu_2O and ammonia as the follows:

$$Cu_2O+O_2+4H_2O+16NH_3 \rightarrow 4[Cu(NH_3)_4]^{2+}+8OH^- \quad \textbf{(4.1.1)}$$

$$[Cu(NH_3)_4]^{2+}+2OH^- \rightarrow Cu(OH)_2+4NH_3 \quad \textbf{(4.1.2)}$$

$$Cu(OH)_2+2OH^- \rightarrow Cu(OH)_4^{2-} \quad \textbf{(4.1.3)}$$

If we continued to increase the amount of ammonia, hollow SiO_2 nanocubes or even secondly SiO_2 nanoparticles can be obtained (see Figure 4.1.2.2 b and c). Thus, we need to find a novel approach for the PNIPAM coating on the surface of Cu_2O nanoparitcles. Compared with the conventional method of PNIPAM coating, our method is much simpler.[29,173]

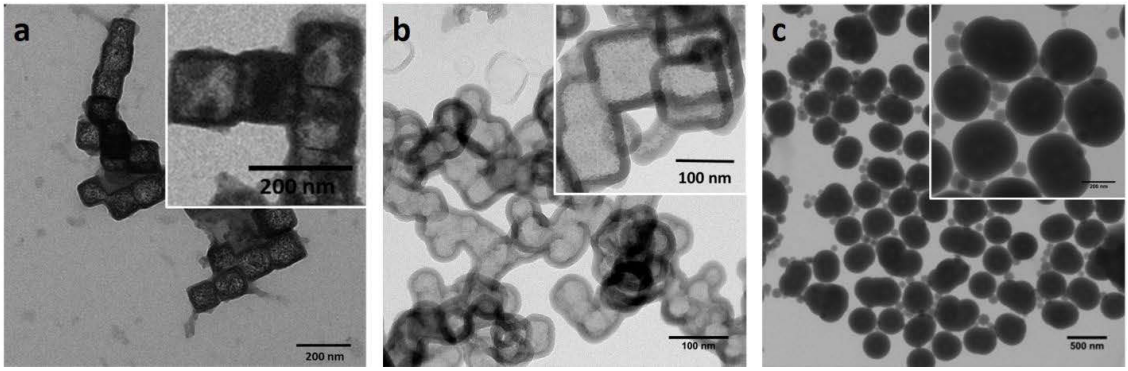

Figure 4.1.2.2 TEM images of Cu_2O@SiO_2 hollow nanoparticles with different amount of ammonia: (a) 0.013% (v/v) (b) 0.67% (v/v) and (c) 1.3% (v/v).

Without modifying SiO_2 or polystyrene shell as the interlayer, single Cu_2O nanocubes is encapsulated in a thermosensitive PNIPAM shell which avoids the etching and aggregation of Cu_2O nanocubes. Experimental process and a proposed mechanism are illustrated in Scheme 4.1.2.1. Cu_2O nanocubes were prepared first by seeds-mediated method using sodium dodecyl sulfate (SDS) as the capping surfactant and the surfaces of Cu_2O nanocubes are negatively charged. By charge interaction, NaSS was modified on the surface of Cu_2O nanocubes using PDDA as a medium and surface zeta potential of the Cu_2O nanocubes changed from -21.2 mV to 53 mV accordingly. Based on double bonds supplied by NASS, polymerization is initiated by the positive initiator V50 and PNIPAM-shell is coated onto Cu_2O nanocubes.

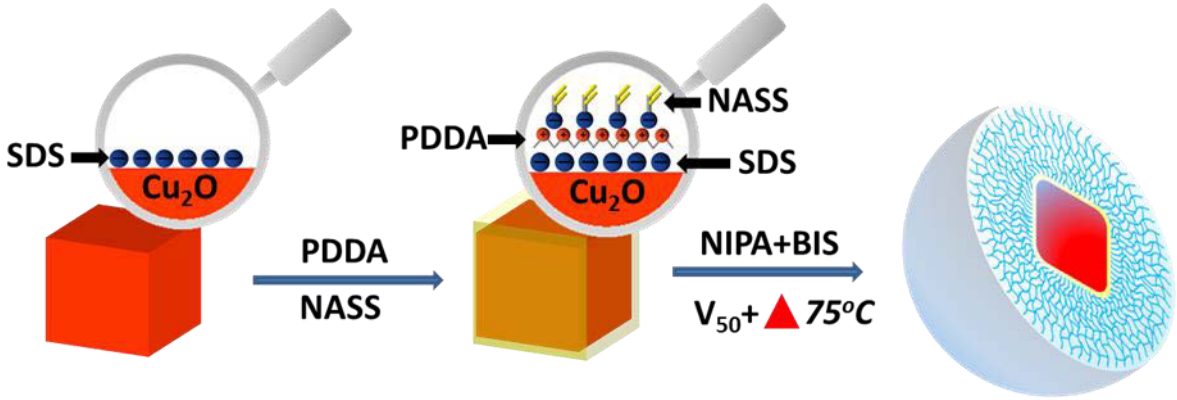

Scheme 4.1.2.1 Schematic illustration of the procedure used to coat PNIPAM on the surface of Cu_2O nanocubes.

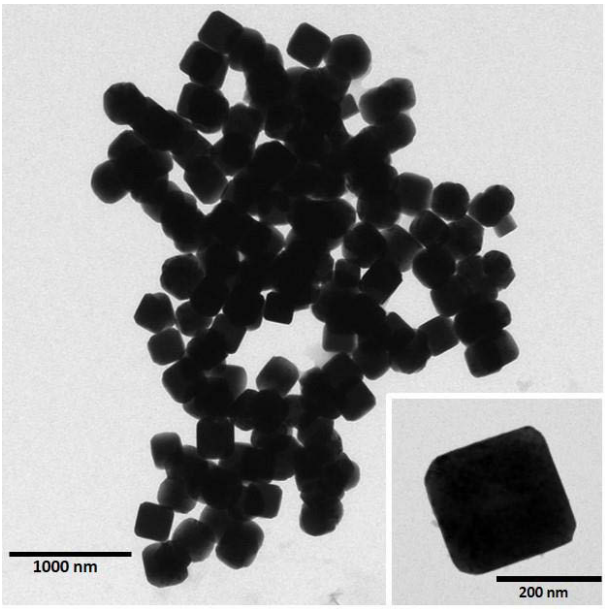

Figure 4.1.2.3 TEM images of bare Cu_2O nanocubes.

As shown in Figure. 4.1.2.3, Cu_2O nanocubes with an average edge length of 259±19 nm (see Figure 4.1.1.2b) were first prepared via seed-mediated method. Without surface modified, most of the Cu_2O nanocubes aggregated together due to the high surface energy. Although as a surfactant, SDS could provide limited hydrophilic force and charge repulsion, it was not enough to offset the effect of the surface energy.

In order to construct uniform PNIPAM shell coating, the Cu_2O nanocubes were modified with PDDA and NaSS as the interlayer. At first, PDDA acts as a carrier for the NaSS to supply the double bonds for the PNIPAM coating via a precipitation polymerization. Secondly, due to the large amounts of positive charges in PDDA chains after mixing with NaSS (the ratio of positive and negative charges contained in PDDA and NaSS is 1:0.074), PDDA/NaSS is firmly attached to the negatively-charged surface of the SDS stabilized cubes (the surface zeta potential changed from -21.2 mV to 53 mV) and serves as a stabilizer to make the Cu_2O nanocubes separate with each other during the polymerization process.

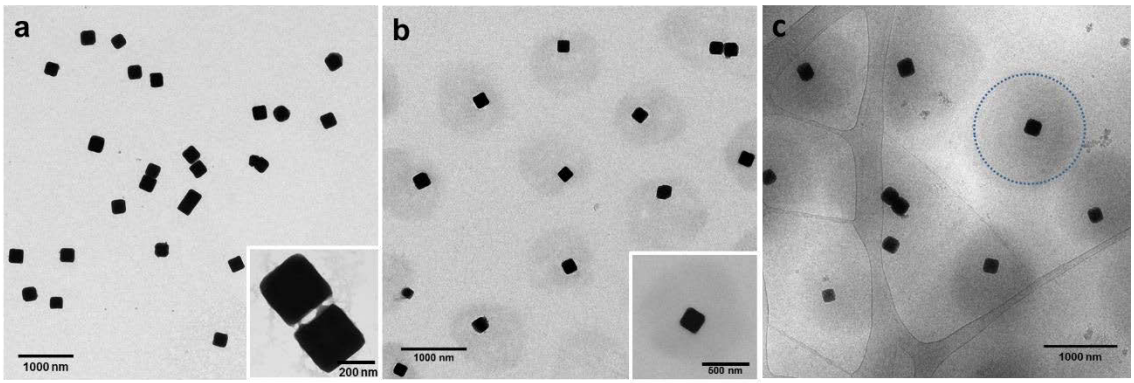

Figure 4.1.2.4 TEM images of (a) Cu_2O@PDDA-NaSS and (b) Cu_2O@PNIPAM core-shell nanoparticles. (c) Cryo-TEM image of Cu_2O@PNIPAM core-shell nanoparticles (Dashed circle indicate the size of the PNIPAM shell determined by DLS in its swollen state at room temperature).

As shown in Figure 4.1.2.4a, monodispersed Cu_2O nanocubes were obtained after PDDA/NaSS coating, and a very thin PDDA/NaSS layer can be observed clearly from the insert TEM image in Figure 4.1.2.4a. The formation of PNIPAM shell on the Cu_2O nanocubes surface was first confirmed by the TEM image (Figure 4.1.2.4b). PNIPAM shell of around 360 nm thick was uniformly wrapped on the surface of Cu_2O nanocubes and all of the Cu_2O nanoparticles retained the cubic shapes. Since PNIPAM contains strong hydrophilic interaction below the lower critical solution temperature (LCST), the Cu_2O@PNIPAM core-shell nanoparticles separated with each other very well. Figure 4.1.2.4c shows the cryo-TEM image of Cu_2O@PNIPAM core-shell particles at room temperature. The thickness of the PNIPAM shell measured from cryo-TEM image (marked as a dashed line in Figure 4.1.2.4c) was agreed well with the thickness determined by DLS at the same condition as shown in Figure 4.1.2.5, which was about 360 nm.

DLS measurements of Cu_2O@PNIPAM core-shell nanoparticles were shown in Figure 4.1.2.5a, which proved the thermoresponsibility of the PNIPAM shell. Figure 4.1.2.5b and Figure 4.1.2.5c show the cryo-TEM images of the core-shell nanoparticles taken at 15 ^oC and 50 ^oC, respectively, which are perfect corresponding to the point b and point c on the DLS curve. Due to the hydrophilic property of PNIPAM below LCST, the PNIPAM shell was fully swollen in the water solution (see Figure 4.1.2.5a and b). In contrast, when the temperature was increased to 50 ^oC, PNIPAM became hydrophobic and the water in the PNIPAM network was extruded which led to the shrinkage of the PNIPAM shell (see Figure 4.1.2.5a and c). As shown in Figure 4.1.2.5a, a well-defined volume transition is observed around 32 ^oC for the

Cu_2O@PNIPAM core-shell system and the presence of Cu_2O nanocubes core does not significantly affect the swelling and deswelling behavior of the PNIPAM shell.

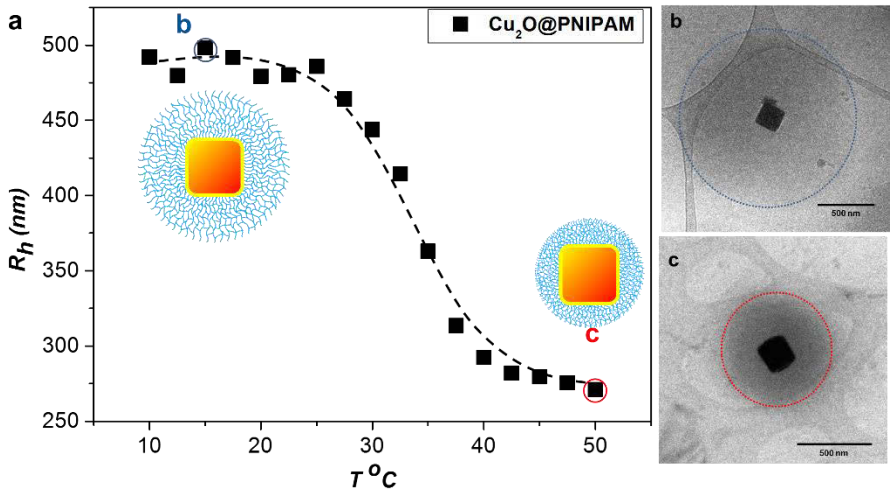

Figure 4.1.2.5 (a) Hydrodynamic radius of Cu_2O@PNIPAM core-shell nanoparticles as a function of temperature in aqueous solution, (b,c) Cryo-TEM images of Cu_2O@PNIPAM core-shell nanoparticles in swollen state at 15 °C and in shrunken state at 50 °C, respectively.

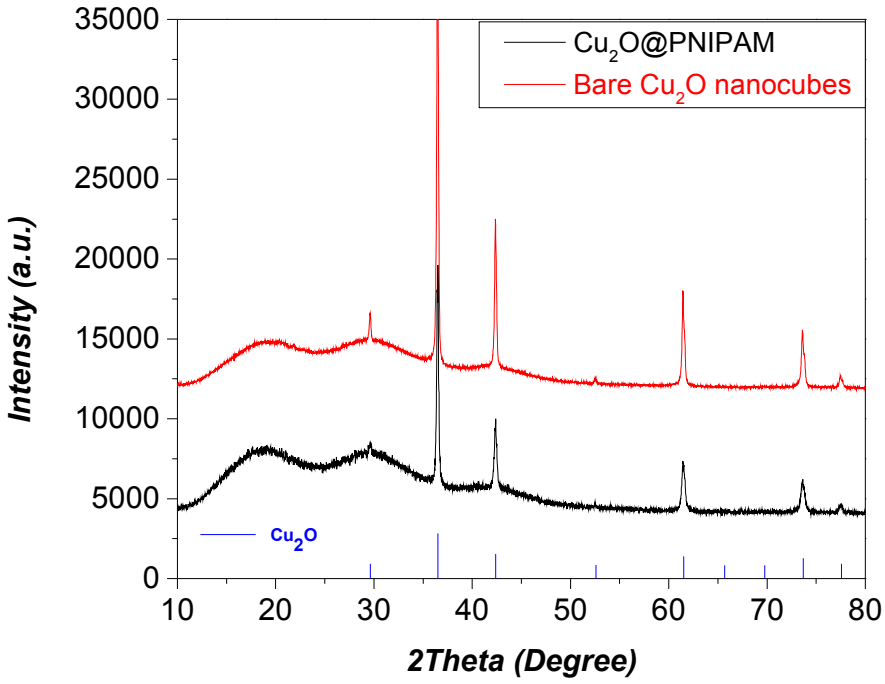

Figure 4.1.2.6 XRD patterns of fresh made bare Cu_2O nanocubes (red) and Cu_2O@PNIPAM core-shell particles (black). As reference, standard XRD pattern of Cu_2O (JCPDS: No.65-3288) is shown in Figure.

The XRD patterns of freshly prepared Cu_2O nanocubes and Cu_2O@PNIPAM core-shell nanoparticles are shown in Figure 4.1.2.6. After the PNIPAM coating, all of the peaks corresponding to Cu_2O at 2θ=29.63°, 36.50°, 42.40°, 52.58°, 61.52°, 73.70° and 77.57° were retained and no other peaks can be observed from the XRD spectra. This indicates that the modification of PNIPAM shells will not lead to the oxidation of Cu_2O. A similar result also can be seen from the selected area electron diffraction (SAED) patterns of bare Cu_2O nanocubes and Cu_2O@PNIPAM core-shell nanoparticles. The SAED patterns shown in Figure 4.1.2.7a2 and b2 directly demonstrate that with the protection of PNIPAM shells, the nanocubes are still Cu_2O without oxidation, because the spacings are not consistent with the monoclinic structure of CuO. Thus, PNIPAM coating doesn't create additional diffractions spot due to its amorphous structure.

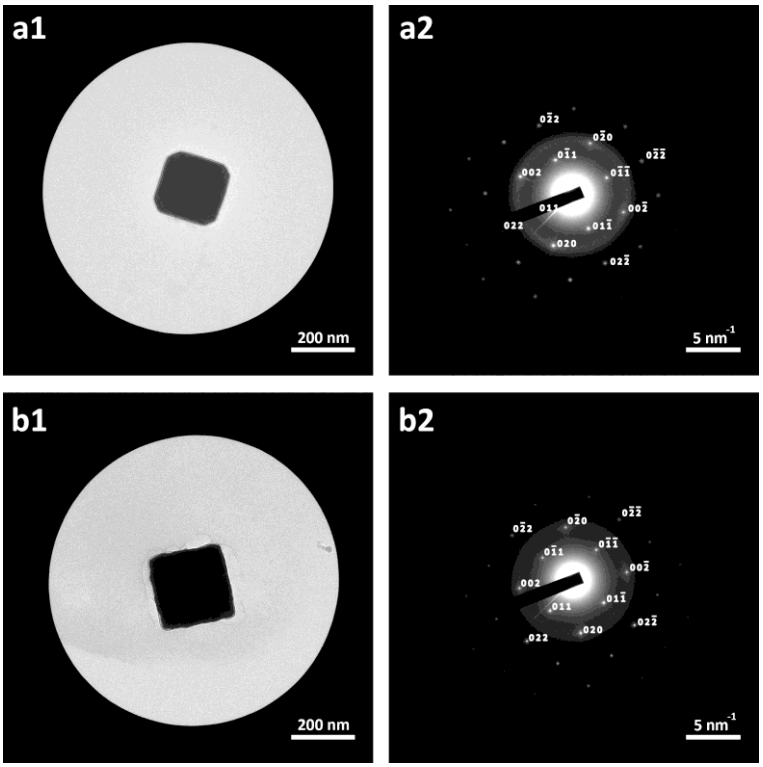

Figure 4.1.2.7 TEM images and their corresponding selected area electron diffraction (SAED) patterns of fresh prepared bare Cu_2O nanocubes (a1 and a2), and Cu_2O@PNIPAM core-shell nanoparticles (b1 and b2).

In order to study the influence of the interlayer on the formation of PNIPAM shell, a series of samples with different amounts of NaSS and PDDA have been synthesized (see table 4.1.2.1**,** figure 4.1.2.8 and figure 4.1.2.9). As shown in figure 4.1.2.8A, when only 1.3g PDDA was added, non-coated Cu_2O nanocubes can be observed in the system. On the contrary, keeping the amount of NaSS constant, increasing the amount of PDDA from 1.3g to 2.6g, the amount

of the PNIPAM grafted on the Cu_2O nanocubes surface was dramatically increased and each of the Cu_2O nanocubes was wrapped with uniform PNIPAM shell (see figure 4.1.2.8 A and 4.1.2.8 B). If the amount of PDDA was continued to increase from 2.6g to 3.9g, a lot of PNIPAM secondary particles have been found in the system, which is due to the excessive PDDA molecules in the system (see Figure 4.1.2.9). The above results indicate that the amount of PDDA chains in the system influences directly the amount of PNIPAM coated on the surface of Cu_2O nanocubes.

Keeping the amount of PDDA unchanged, increasing the molar ratio of NaSS to PDDA from 0.037 to 0.074 leaded to PNIPAM shells with higher density coated on the Cu_2O surface (see figure 4.1.2.8B and 4.1.2.8C). However, if too much NaSS has been adsorbed on the PDDA chains, some of the particles aggregated together due to the weakening of the coulombic repulsions between the particles as shown in Figure 4.1.2.8D.

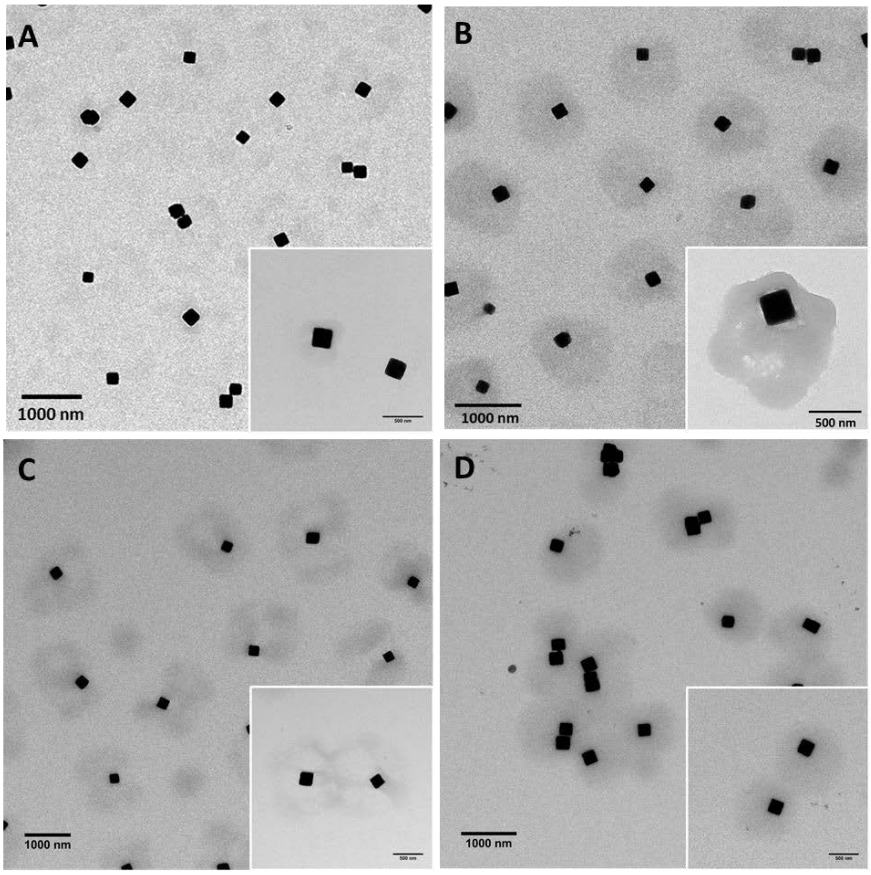

Figure 4.1.2.8 TEM images of the samples in Table 4.1.2.1 with different molar ratio of NaSS and PDDA: (A) N_{NaSS}/N_{PDDA}=0.148, (B) N_{NaSS}/N_{PDDA}=0.074, (C) N_{NaSS}/N_{PDDA}=0.037, (D) N_{NaSS}/N_{PDDA}=0.111.

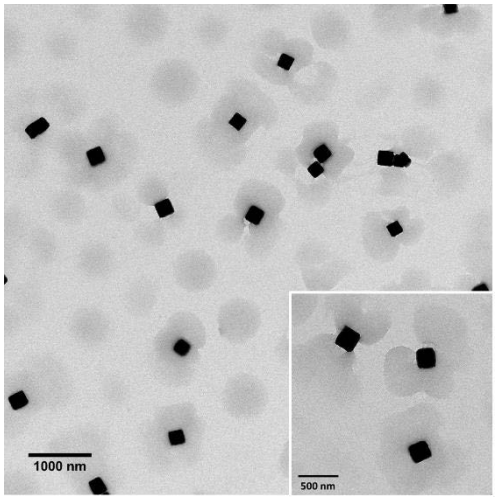

Figure 4.1.2.9 TEM image of the sample C in Table 4.1.2.1 with molar ratio of NaSS and PDDA: N_{NaSS}/N_{PDDA}=0.049.

Table 4.1.2.1. Synthesis of Cu_2O@PNIPAM core-shell nanoparticles with different amounts of NaSS and PDDA.

	PDDA(g)	**NaSS(g)**	**Bis(mol)**	**NIPAM(mol)**	**N_1/N_2***	**Morphology**
A	1.3	0.050	3.31×10^{-5}	2.56×10^{-4}	0.148	Partially uncoated
B	2.6	0.050	3.31×10^{-5}	2.56×10^{-4}	0.074	Homogeneous
C	3.9	0.050	3.31×10^{-5}	2.56×10^{-4}	0.049	Secondary particles
D	2.6	0.025	3.31×10^{-5}	2.56×10^{-4}	0.037	Low density shell
E	2.6	0.074	3.31×10^{-5}	2.56×10^{-4}	0.111	Aggregation

***N_1:**The moles of NaSS; **N_2:** The moles of repeating units of PDDA.

The thickness of the PNIPAM shells can be controlled by using different amount of NIPAM monomers and crosslinkers during the coating process. Consequently, a series of Cu_2O@PNIPAM core-shell nanoparticles have been synthesized as shown in Table 4.1.2.2. The TEM images of each sample and the corresponding size measurements from DLS are shown in Figure 4.1.2.10.

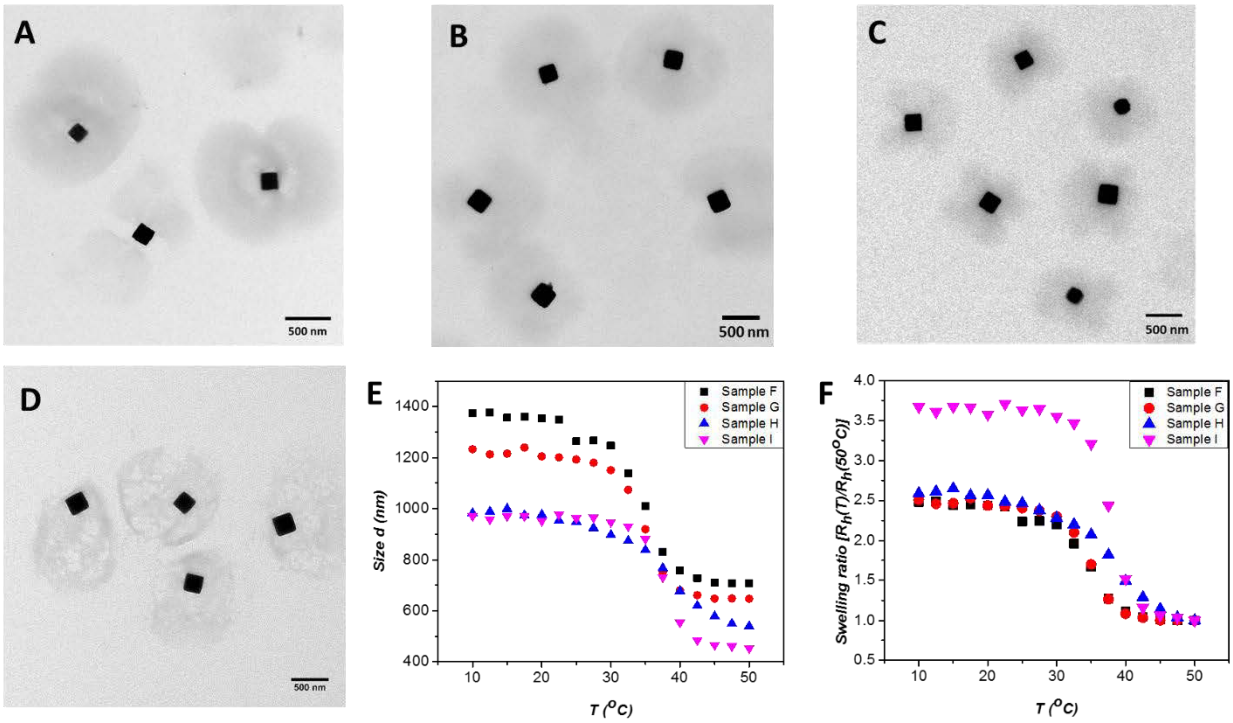

Figure 4.1.2.10 TEM images of Cu_2O@PNIPAM core-shell nanoparticles corresponding to the samples listed in table 4.1.2.2 with different amount of monomers and cross-linkers: (A) Sample F, 3.18×10^{-4}mol NIPAM, 9% Bis (molar ratio), (B) Sample G, 2.56×10^{-4}mol NIPAM, 9% Bis (molar ratio), (C) Sample H, 2.56×10^{-4}mol NIPAM, 13% Bis (molar ratio), (D) Sample I, 2.06×10^{-4}mol NIPAM, 9% Bis (molar ratio). (E) Temperature dependent DLS measurement and (F) Swelling ratio of the Cu_2O@PNIPAM core-shell nanoparticle samples F to I from table 4.1.2.2.

As shown in Figure 4.1.2.10a and b, keeping the other conditions constant, when the amount of NIPAM monomers was decreased from 3.18×10^{-4} mol to 2.56×10^{-4} mol, a decrease in the PNIPAM shell thickness can be observed from the TEM images. The DLS measurement gives similar results, which shows that the hydrodynamic radius of the samples changes from 549 nm to 479 nm. When only the cross-linker content was increased from 9% to 13% (the mole percent ratio with NIPAM), a significant change in the size of the samples can be seen from the TEM images and the radius of the core-shell nanoparticles decreased from 479 nm to 371 nm according to the DLS measurements (see Figure 4.1.2.10b, c and e). When the amount of NIPAM monomers was decreased by 19.4%, both of the thickness and the density of the PNIPAM shell decreased. As shown in Figure 4.1.2.10d, a lot of holes can be seen in the PNIPAM shell due to the further reduction of the NIPAM monomers. The changing of the amount of cross-linker can influence the network rigidity and leads to the changing of the fraction of non-responsive polymer material (pure cross-linker based polymer) in the core-shell nanoparticles, which is similar to the results found for the bare PNIPAM particles.[59]

The influence of temperature on the size of these core-shell nanoparticles was measured by dynamic light scattering (DLS) (see Figure 4.1.2.10). All of the samples show similar volume phase transition temperature at around 33°C, which indicates that the encapsulating of Cu_2O nanocubes does not influence the thermosensitivity of the PNIPAM microgels. Also, with the decreasing of the density and rigidity of the PNIPAM shells, Sample I presents the highest swelling ratio due to its lowest cross-linker density.

Table 4.1.2.2. Synthesis of Cu_2O@PNIPAM core-shell nanoparticles with different amounts of NIPAM monomers and cross-linkers.

	NIPAM (mol)	**Cu_2O cores (mg)**	**PNIPAM shell thickness (15°C/nm)***	**$N_{Cross\text{-}linker}/N_{Monomers}$ (mol/mol)**
F	$3.18*10^{-4}$	6.6	549	9%
G	$2.56*10^{-4}$	6.6	479	9%
H	$2.56*10^{-4}$	6.6	371	13%
I	$2.06*10^{-4}$	6.6	349	9%

* The thickness of PNIPAM shell at 15°C was calculated according to data from the DLS measurement shown in Figure 4.1.2.10.

As shown in Figure 4.1.2.11a, compared to the bare Cu_2O nanocubes, the Cu_2O@PNIPAM core-shell nanoparticles maintained a stronger absorption of light and narrower band gap.[39,174] Moreover, the UV-vis spectra of Cu_2O@PNIPAM core-shell nanoparticles in aqueous solution at different temperatures were recorded as shown in Figure 4.1.2.11b. It can be observed clearly that there is a red shift of the characteristic peak of Cu_2O from 517 nm to 525 nm accompanied with a decrease in absorbance with the increasing of the temperature from 10 °C to 50 °C. On one hand, the shifting to longer wavelengths may be attributed to the increase of local refractive index during the collapse of the PNIPAM shell.[172,175] As a kind of semiconductor materials, the refractive index of Cu_2O is higher than PNIPAM at different temperature, which is the reason that the absorbance decreased with the increasing of the temperature according to the Mie scattering theory.[176,177] On the other hand, the changes of the surface properties of Cu_2O nanocubes may ocurr upon the modification of PNIPAM shells, which will lead to shifting and decreasing of absorption band. However, the details on such changes are difficult to be measured and should be studied further in the future.

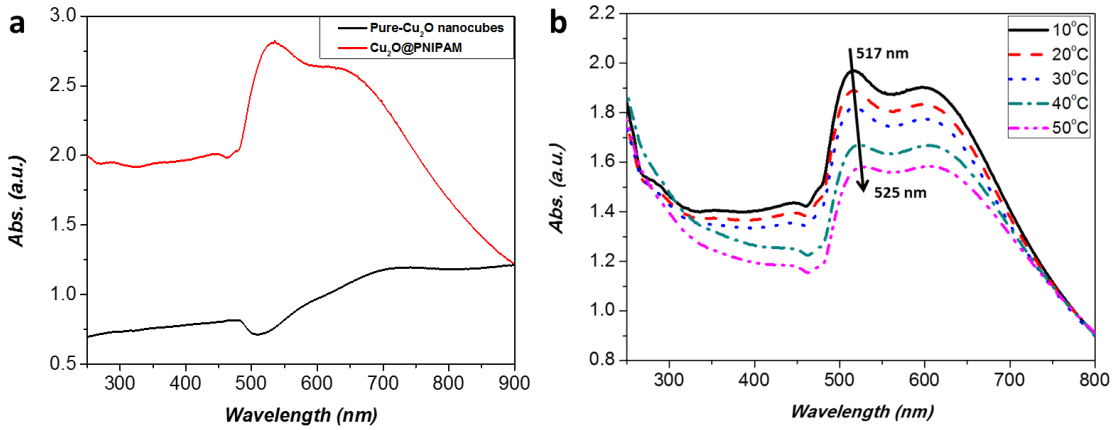

Figure 4.1.2.11 (a) UV-vis spectra of Cu_2O nanocubes (black) and Cu_2O@PNIPAM (red) at room temperature with the solid content of 0.21mg/mL. (b) UV-vis spectra of Cu_2O@PNIPAM core-shell nanoparticles with changing of the temperature.

4.1.3 Stability of Cu_2O@PNIPAM core-shell nanoparticles

According to strong reducing property, Cu_2O is very active in water and easily transforms to CuO. The XRD patterns of Cu_2O nanocubes without PNIPAM shell are presented in Figure 4.1.3.1a. After storing in water in the dark place for 10 days, the peaks at $2\theta=35.5^o$, 38.34^o, 38.66^o and 48.8^o corresponding to the Bragg reflections of CuO have been observed. Also the color of the solution changed from orange to dark green and the cubic structure of the Cu_2O has been destroyed due to the production of CuO (see the photo in Figure 4.1.3.1c). Compared with the fresh prepared Cu_2O nanocubes, none of the Cu_2O nanocubes were oxidized to CuO with the protection of PNIPAM shell after keeping for 10 days under the same condition. The corresponding XRD pattern has been shown in Figure 4.1.3.1d. Moreover, all of the Cu_2O particles maintained cubic structure and no aggregation was observed in the system (see Figure 4.1.3.1f).

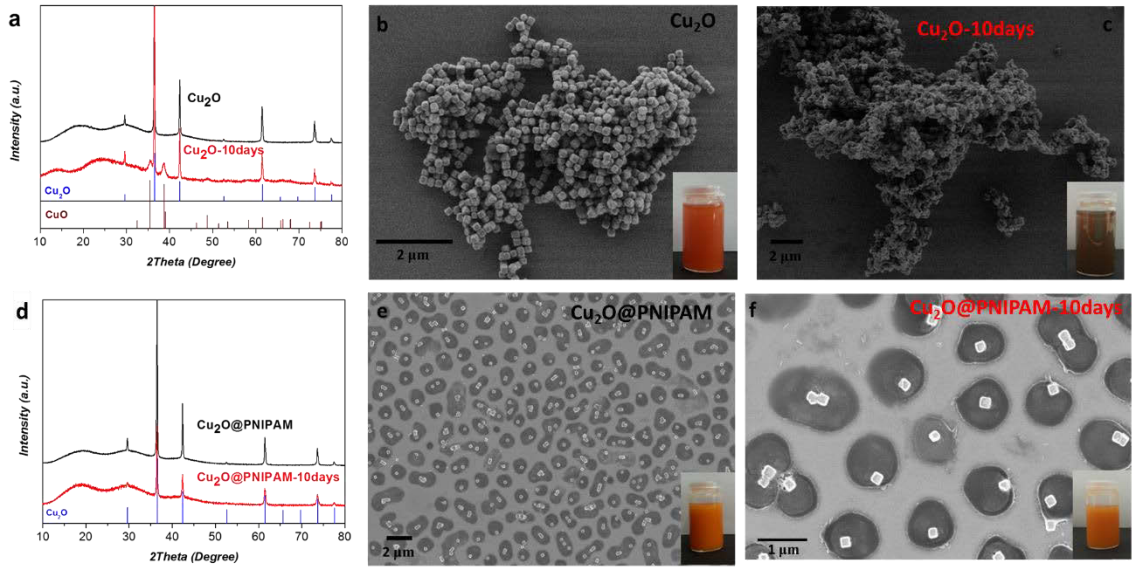

Figure 4.1.3.1 (a) XRD patterns of fresh Cu_2O nanocubes (up) and Cu_2O nanocubes kept in water for 10 days (down). SEM images of (b) fresh Cu_2O nanocubes and (c) Cu_2O nanocubes kept in water for 10 days. (d) XRD patterns of fresh Cu_2O@PNIPAM core-shell nanoparticles (up) and Cu_2O@PNIPAM core-shell nanoparticles in water for 10 days (down). SEM images of (e) fresh Cu_2O@PNIPAM core-shell nanoparticles and (f) Cu_2O@PNIPAM core-shell nanoparticles kept in water for 10 days.

In order to further prove that the stability of Cu_2O nanocubes in water has been greatly enhanced with the protection of PNIPAM shell, Cu_2O@PNIPAM core-shell nanoparticles were kept in water at room temperature for 100 days. Near edge X-ray absorption fine structure (NEXAFS) spectroscopy in combination with transmission X-ray microscopy (TXM) has been used to test the samples for the existence of Cu^{2+} at crystal defect sites or amorphous CuO. The NEXAFS spectroscopy provides the needed chemical sensitivity and the TXM gives the possibility to examine a statistical amount of particles, which can be analyzed on the single particle level. Figure 4.1.3.2a shows a NEXAFS-TXM micrograph of Cu_2O@PNIPAM in false color representation. The red channel is sensitive to Cu_2O, whereas the green channel is sensitive to CuO. The contrast of the PNIPAM shell is too low to be resolved. It is obvious that almost all of the copper containing particles is made of copper-(I)-oxide and only a very small amount of CuO points can be detected, because of which a small shoulder around 930.8 eV can be observed in the spectrum of orange marked particle as shown in Figure 4.1.3.2b. A similar shoulder can be also found in Figure 4.1.3.2d for the fresh prepared Cu_2O nanocubes. Thus, this small amount of CuO should be the side products from the synthesis process of Cu_2O nanocubes, which could not be removed during the washing step or from the preparation process for the measurement. However, this CuO signal became much smaller for both of the

average signals over all particles in field of view of the Cu_2O@PNIPAM core-shell nanoparticles and the bare fresh made Cu_2O nanocubes. Thus the amount of CuO is extremely low in the samples and the PNIPAM shell can effectively protect the Cu_2O nanocubes from oxidation.

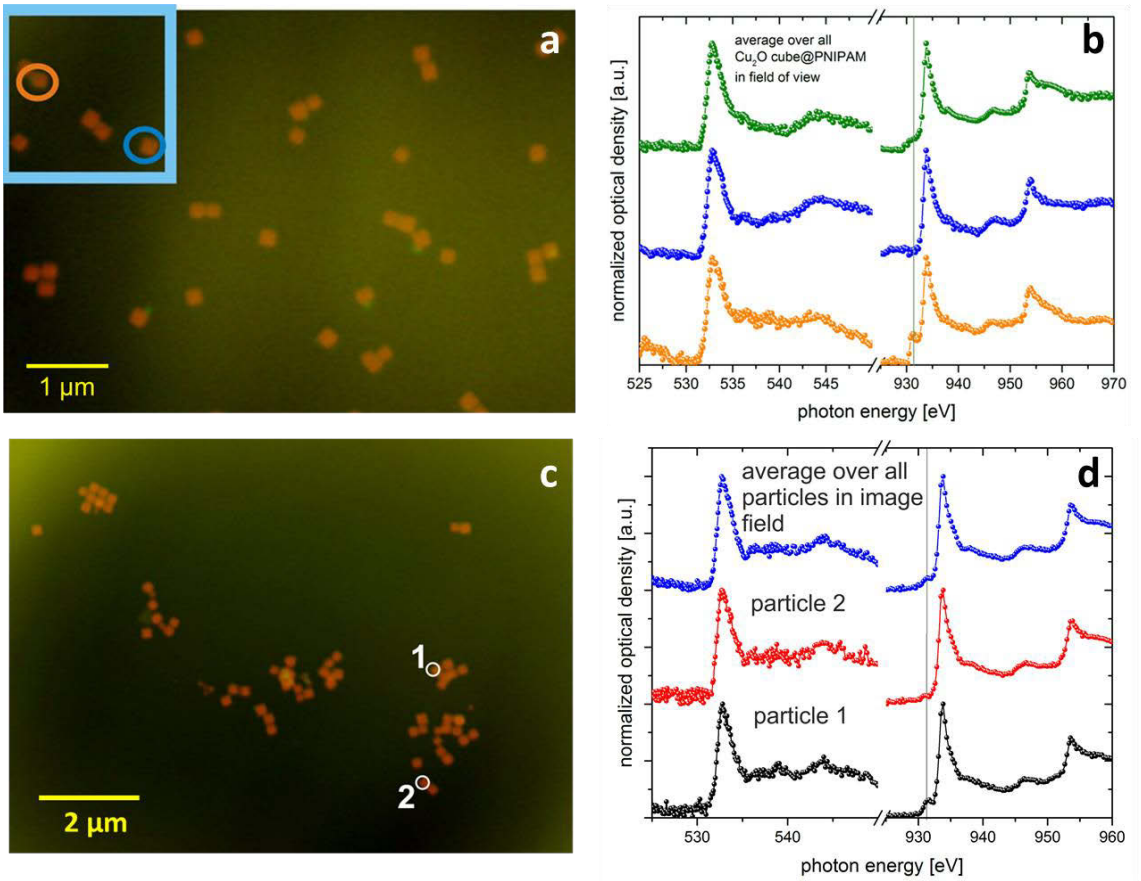

Figure 4.1.3.2 (a) TXM micrograph of the Cu_2O-nanocubes@PNIPAM at two different photon energies: The red channel depicts the nanocubes with Cu_2O, and the green channel refers to CuO. (b) NEXAFS-spectra of the average signals over all Cu_2O@PNIPAM core-shell nanoparticles in field of view (green line) and the marked particles in the inset of micrograph on the left hand side at the O-*K*-edge and the Cu-$L_{2,3}$-edge (blue and orange lines). (c) TXM micrograph of bare Cu_2O nanocubes at two different photon energies: The red channel depicts the nanocubes with Cu_2O, and the green channel refers to CuO. (d) NEXAFS-spectra of the average signals over all Cu_2O nanocubes in field of view (blue line) and the marked particles in the inset of micrograph on the left hand side at the O-*K*-edge and the Cu-$L_{2,3}$-edge (red and black lines).

Figure 4.1.3.3 The photographs of solution of Cu_2O@PNIPAM core-shell nanoparticles (left) and Cu_2O nanocubes (right) after storing for different times.

The colloidal stability of Cu_2O@PNIPAM core-shell nanoparticles have been also measured. As shown in Figure 4.1.3.3, both of the Cu_2O@PNIPAM core-shell nanoparticles and bare Cu_2O nanocubes were kept in water and the photos were taken at different time. Compared with the Cu_2O@PNIPAM core-shell nanoparticles, a significant precipitation happened for the bare Cu_2O nanocubes after 10 mins. After storing in water for the whole night, the core-shell nanoparticles still maintained stability in water without obvious precipitation while all of the bare Cu_2O nanocubes have precipitated, which means that the Cu_2O nanocubes with PNIPAM shells contain a much more stable system than the pure Cu_2O nanocubes due to the hydrophilic property of the PNIPAM shell below the lower critical solution temperature (LCST).

In conclusion, we introduce a novel method to synthesize hybrid core-shell microgels consisting of Cu_2O nanocubes as the core and thermosensitive PNIPAM as the shell. The core-shell nanoreactors present much better colloidal stability than pure Cu_2O nanocubes in water solution. Moreover, the PNIPAM shell can effectively protect the Cu_2O nanocubes from oxidation for months.

4.2 Photocatalytic activity of Cu_2O@PNIPAM core-shell nanoparticles

The photocatalytic activity of Cu_2O@PNIPAM core-shell nanoparticles has been tested for the photodegradation of MO. As shown in Figure 4.2.1b, in the case of Cu_2O@PNIPAM core-shell nanocubes, the peaks at 464 nm and 271 nm decrease gradually with time, which results from the degradation of MO. The theory of the photocatalytic reaction of Cu_2O has been introduced before and the principle schematic was shown in Figure 4.2.1a. Under visible light irradiation, hydroxide radicals were produced on the surface of the Cu_2O nanocubes, which lead to the degradation of dye molecules. The degradation of MO can be also followed by the changing of the colours. After the catalytic reaction, the colour of MO transformed from orange to colorless (see Figure 4.2.1a).

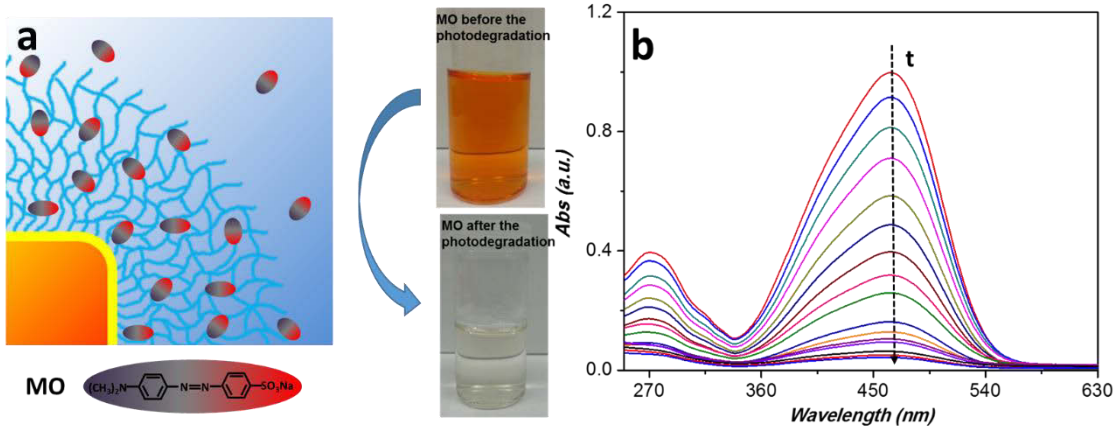

Figure 4.2.1 (a) Illustration of the catalytic process. (b) UV-vis absorption spectra of MO as a function of irradiation time using Cu_2O@PNIPAM core-shell nanoparticles as photocatalyst.

According to the literature, cubic Cu_2O crystals are simply not photocatalytically active.[168] This is due to the reason that compared with the other crystal structures, Cu_2O nanocubes contain mostly {100} facets, which have 100% saturated oxygen bonds. Thus the {100} face is relatively neutral, because of which the cubic Cu_2O crystals are less sensitive to adsorb the negatively charged dye molecules. Surprisingly, after being modified with PNIPAM shell, the photocatalytic activity of Cu_2O nanocubes was enhanced significantly. As shown in Figure 4.2.2, first order reaction kinetic can be applied for the photo-degradation of MO by Cu_2O.[76] To compare the photocatalytic activity of Cu_2O@PNIPAM core-shell particles and the bare Cu_2O nanocubes, the reaction rate was normalized to the total surface of the Cu_2O nanocubes. As shown in Figure 4.2.2a, after irradiation for 4 h, the fraction of the remaining absorption of MO measured at 464 nm was 2.9% for the Cu_2O@PNIPAM core-shell nanoparticles and 99.4% for the pure Cu_2O nanocubes. As expected, the core-shell nanoparticles are much more

photocatalytically active than the pure Cu_2O nanocubes. ($k_{Cu2O\text{-}15°C}$ = 1.16×10^{-4} $Lmin^{-1}m^{-2}$, $k_{Cu2O\text{-}P\text{-}15°C}$=$4.67\times10^{-2}$ $Lmin^{-1}m^{-2}$) Increasing temperature can lead to faster reaction rate for the pure Cu_2O nanocubes, which has been shown as the blue line in Figure 4.2.2a, the value is still very low compared with the core-shell hybrid nanomaterials.

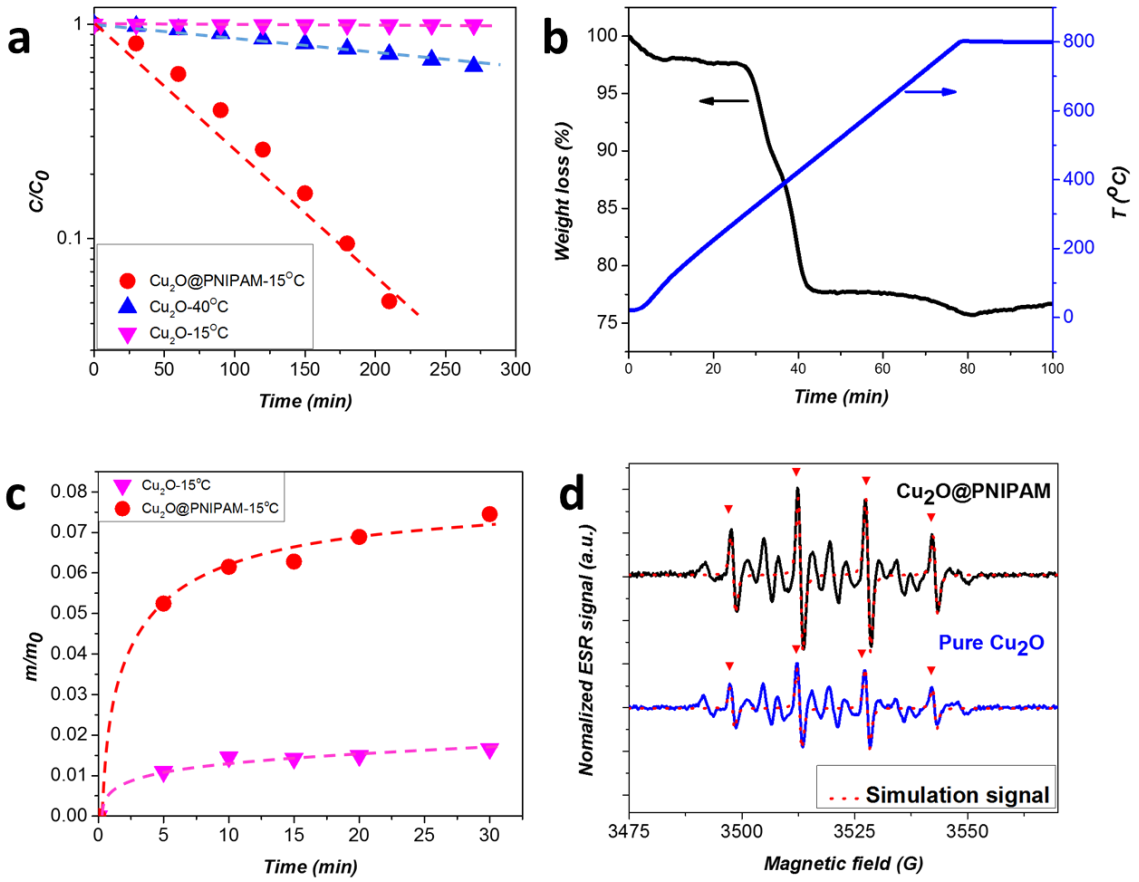

Figure 4.2.2 (a) Kinetic analysis of MO reduced by Cu_2O@PNIPAM core-shell nanoparticles and pure Cu_2O nanocubes at different temperatures. (b) TGA spectra of Cu_2O@PNIPAM core-shell nanoparticles. (c) The Methyl Orange (MO) adsorption curve of pure Cu_2O nanocubes at 15°C (triangles), Cu_2O@PNIPAM core-shell nanoparticles at 15°C (circles), respectively. (d) ESR spectra of aqueous dispersions of Cu_2O@PNIPAM core-shell nanoparticles (upper black trace) and pure Cu_2O nanocubes (lower blue trace) with DMPO spin traps added. Triangles indicate the four ESR lines characteristic DMPO-•OH radicals. The overlaid traces are simulations of the DMPO-•OH signal using the MATLAB library EasySpin.

The significant improvement of photocatalytic efficiency of Cu_2O is caused by the following reasons. At first, from the zeta potential measurement, the chains of PNIPAM shell contained positive charge (13.7 mV), which favors a high binding affinity of the hydrogel shell with negtively charged MO. As shown in Figure 4.2.2c, after mixing with MO solution for 30 min, around 7.5wt. % of MO was adsorbed by Cu_2O@PNIPAM core-shell nanoparticles and only

1.5wt. % of MO was adsorbed by the bare ones. Zeta potential measurements for the core-shell systems at 15 °C showing a decrease of +13.7 mV to -5.3 mV upon adding the negatively charged MO to the suspension, support the picture of MO enrichment in the shell. As we find that the reaction is fully surface-controlled,[178] MO enrichment at the nanocube surface would lead proportionally to a higher surface rate. Secondly, as shown in figure 4.1.2.11a, with the coating of PNIPAM shell, the absorption in the visible range of Cu_2O nanocubes was increased, which leads to a higher concentration of hydroxyl radicals. ESR measurements for the Cu_2O@PNIPAM core-shell nanoparticles and bare Cu_2O nanocubes have been shown in Figure 4.2.2d.[179] 4 peaks labeled in the spectra were assigned to the DMPO-•OH adducts, which were produced by hydroxyl radicals trapped with DMPO. For the core-shell nanoparticles, the DMPO-•OH signal is at least two times stronger than that of the bare Cu_2O nanocubes. This indicates that much more •OH have been effectively generated by Cu_2O@PNIPAM core-shell microgels than by bare Cu_2O nanocubes. Since the hydroxyl radicals are the active species reacting with MO, this should be an important reason for the higher reaction rate of the Cu_2O@PNIPAM core-shell nanoparticles. Also Cu_2O@PNIPAM core-shell nanoparticles were much more stable than pure Cu_2O nanocubes in water solution. At last, as we described before, the surface properties of Cu_2O nanocubes may be changed due to the modification of PNIPAM shells, which will lead to the enhancement of the photocatalytic reaction rate.

The photocatalytic activity of Cu_2O@PNIPAM core-shell nanoparticles at different temperatures has been studied as well. As shown in Figure 4.2.3a, different from the rate constant of bare Cu_2O nanocubes, the reaction rate of Cu_2O@PNIPAM core-shell nanoreactors does not follow a simple Arrhenius law with constant activation energy at different temperatures. When the temperature is lower than the LCST, the reaction rate of core-shell nanoreactor increased with rising temperature. When the temperature of the system was close to the LCST, a dramatic decrease of the reaction rate was observed. Then the reaction rate increased slightly again with further increasing of the temperature. This behavior strongly depended on the the overall physicochemical properties of the Cu_2O@PNIPAM core-shell nanoreactors at different temperatures.

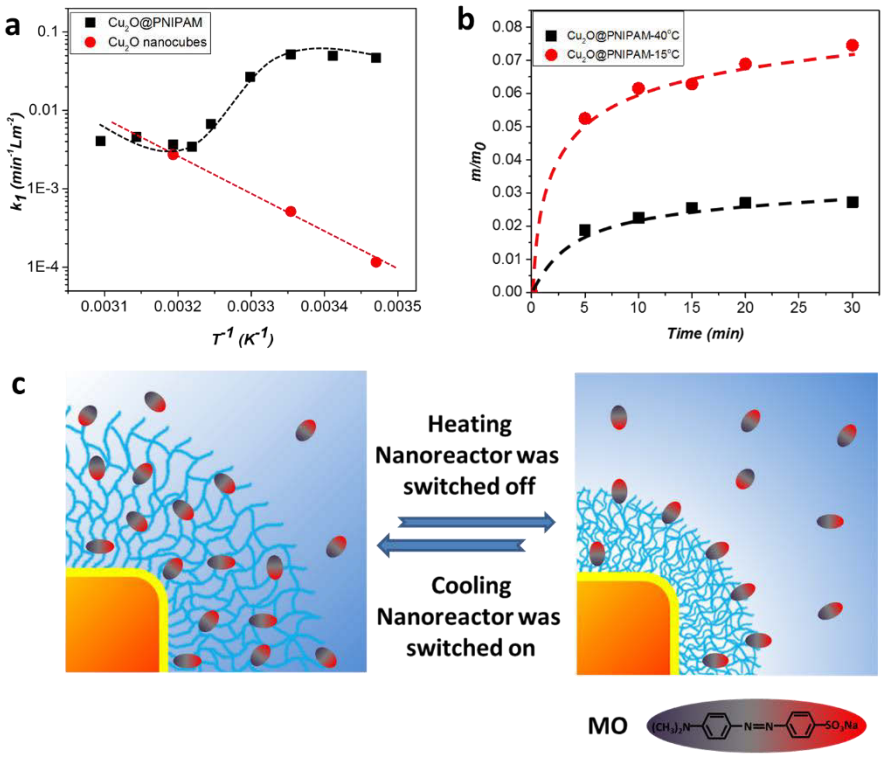

Figure 4.2.3 (a) The reaction rate k_1 (rate constant k_{app} normalized to the surface area of Cu_2O nanocubes) at different temperatures for the bare Cu_2O nanocubes (circles) and the Cu_2O@PNIPAM core-shell nanoreactors system (squares). (b) The Methyl Orange (MO) adsorption curve of Cu_2O@PNIPAM core-shell nanoparticles at 15°C (circles) and 40°C, respectively. (c) Illustration of the catalytic process. At low temperature the network is fully swollen by water and the hydrophilic dye molecules will be enriched within the network. As a consequence of this, the reaction rate for photocatalysis will be increased. In the shrunken state, the increased solvation free enthalpy of the dye molecules decreases their local concentration, and their diffusion coefficient is also reduced due to a tighter polymer network. Together, these effects contribute to a strong decrease of the reaction rate for photocatalysis.

The reasons for the temperature dependant changing of the reaction rate can be qualitatively rationalized by the following reasons. Firstly, as shown in figure 4.1.2.11, we found that the core-shell particles can absorb more light at 15°C than at 40°C. Thus, according to the literature, the core-shell particles can produce more active OH radicals at lower temperature.[180,181] Secondly, at higher temperatures, the PNIPAM shells collapse and become hydrophobic, which likely leads to the decrease of the concentration of MO around the surface of Cu_2O nanocubes (MO has been proved to situate itself at the interface between water and oil in a surfactant-like style, meaning that MO could be mostly located in a thin region constituting the hydrogel/solvent).[182] According to our theory, this depletion of reactants should effectively reduce the rate (see figure 4.2.3c). Hence, the Cu_2O@PNIPAM core-shell nanoreactors contain

higher reaction rate at lower temperature because of the increased OH production and a higher local MO concentration around the surface of Cu_2O nanocubes. However, details of these intricate and very local phenomena are currently difficult to explore and should be interesting for future work. The photocatalytic activity of Cu_2O@PNIPAM core-shell nanoparticals also can be tuned during the reaction. As shown in Figure 4.2.4, compared with the reaction proceed under 15°C, when the temperature was increased to 45°C, the reaction rate slowed down. When the temperature was cooled down back to 15°C, the networks of the PNIPAM swollen and became hydrophilic again, which lead to that the reaction rate became its original appearance.

In summary, the Cu_2O@PNIPAM core-shell nanoreactors show significant enhancement for the photo decomposition of methyl orange under visible light: the reaction rate of the core-shell nanoreactors is 795 times of that of pure Cu_2O nanocubes at 15°C. Moreover, temperature can be used as a trigger to control the photocatalytic activity of the Cu_2O@PNIPAM core-shell microgels as expected from theory. The present work proves that modification of Cu_2O nanocubes with PNIPAM shell will have a great potential for the applications of Cu_2O nanoparticles, which is essential to understand the effect of PNIPAM shell on the properties of metal or metal oxide nanomaterials.

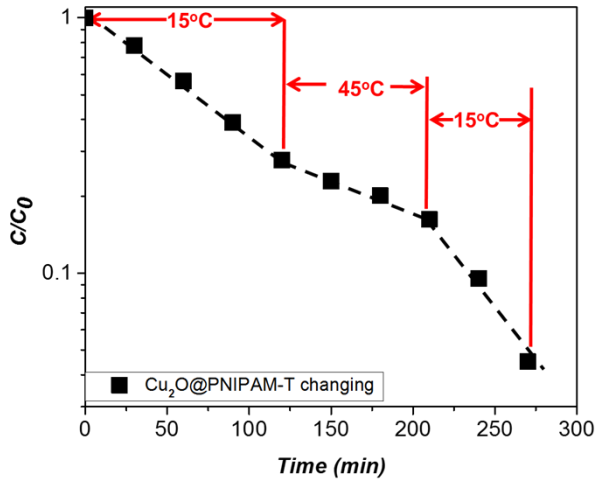

Figure 4.2.4 Kinetic analysis of MO reduced by Cu_2O@PNIPAM core-shell nanoparticles with changing of the temperature.

4.3 Sensitive gas sensors using Cu_2O@PNIPAM core-shell nanoparticles as novel inkjet materials

As introduced before, the colloidal stability of the bare Cu_2O nanocubes was enhanced after the modification of PNIPAM shells. With the protection of PNIPAM shells, the Cu_2O nanocubes can be stored for months without oxidation. Both of these are very important

properties for the ink materials. Moreover, Cu_2O can transform into CuO at temperatures above 250°C,[94] which makes it possible for us to use Cu_2O@PNIPAM core-shell nanoparticles as the novel ink system to prepare CuO gas sensor device.

The procedure for the preparation of CuO gas sensor device by inkjet printing with Cu_2O@PNIPAM core-shell nanoparticles as the ink has been shown in Scheme 4.3.1. Gas sensor device coated with multi-layers of Cu_2O@PNIPAM can be obtained by repeating the inkjet printing process. After heating treatment at 400 °C, all of the Cu_2O nanocubes will transform to CuO and the spaces between each of the CuO nanocubes can be generated because of the thermal removal of the PNIPAM shells, which leads to a larger specific surface area. Thus compared to the device made by bare Cu_2O nanocubes, the sensitivity of the gas sensor device printed by Cu_2O@PNIPAM core-shell nanoparticles should be enhanced.

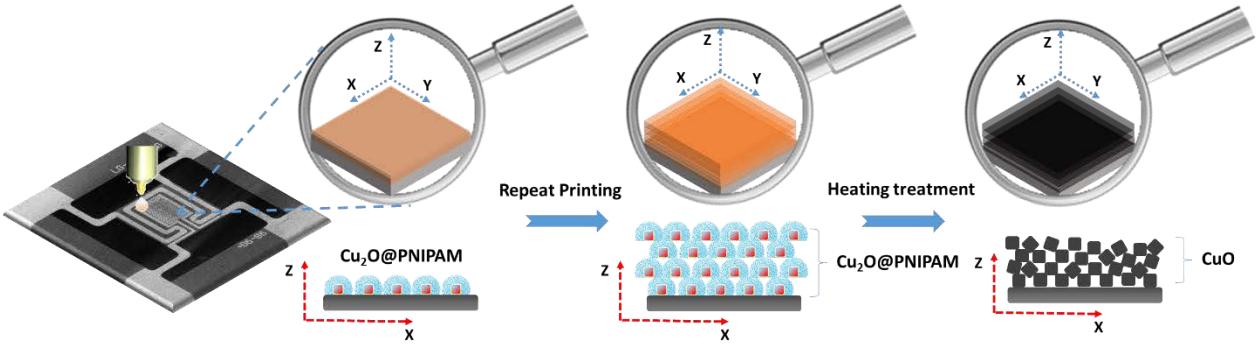

Scheme 4.3.1 Schematic illustration of the inkjet printing procedure used to produce gas sensor device with Cu_2O@PNIPAM core-shell nanoparticles.

The coffee-ring effect is a phenomenon resulting from the aggregation of the nanoparticles along the periphery during drying process on a solid surface, which directly influences the quality of printing.[164,183] As shown in the photograph in Figure 4.3.1a, without modification of PNIPAM shells, the bare Cu_2O nanocubes aggregated to form a coffee-ring after drying, which is undesired for realizing uniform, high-resolution patterns. On the contrast, Cu_2O@PNIPAM core-shell nanoparticles spontaneously formed an array with almost constant surface-to-surface distance between them after drying at room temperature (see Figure 4.3.1b). Moreover, with the coating of PNIPAM shells, the coffee-ring formed from the bare Cu_2O nanocubes disappeared and a uniform film was obtained. The iridescent color of the film with the changing

of incident and observation angles indicates the ordering structure of the core-shell nanoparticles on the substrate.

As shown in Figure 4.3.2, after the high temperature treatment, the PNIPAM shells were completely burned off which leaded to the space between each of the particle and the cubic shapes were perfectly preserved. The XRD patterns of the Cu_2O@PNIPAM core-shell nanoparticles after high temperature treatment are presented in Figure 4.3.2a. The original Cu_2O signals disappear completely, while the peaks corresponding to the (110), (002) and (111) planes of CuO appear according to the JCPDS card (No 45-0937, red signals in Figure 4.3.2b). This further proves that all of the Cu_2O nanoparticles have been transformed to CuO nanoparticles via heating. These results make it possible to prepare mono-disperse CuO nanocubes with constant distance between each other.

During the inkjet printing process, the viscosity, density and surface tension of the ink will directly influence the basic properties of the droplets at a given voltage which dictate the resolution of the printed patterns. The inverse (Z) of the Ohnesorge number is defined to represent the relationship between the fluid ink physical properties and the printability of the system which has been introduced in the theory part.

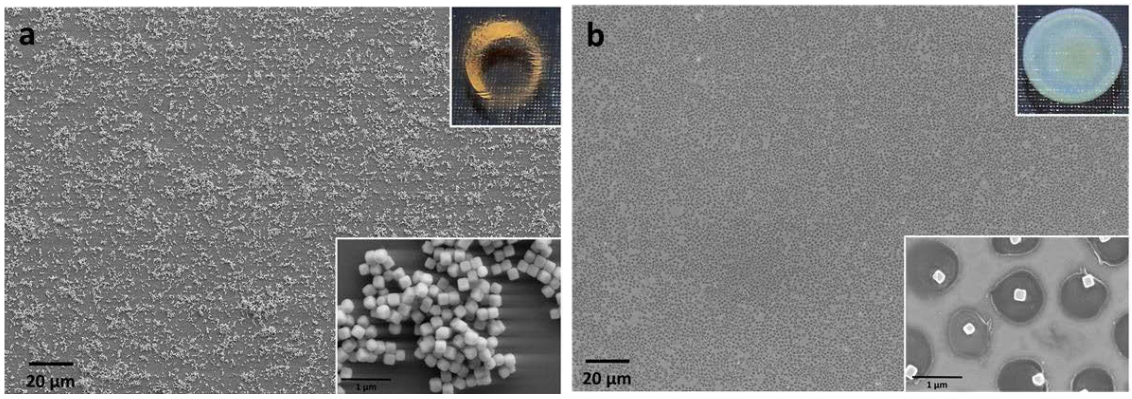

Figure 4.3.1 SEM images of (a) bare Cu_2O nanocubes and (b) Cu_2O@PNIPAM core-shell nanoparticles with the same solid content of 0.026 wt.%. The insert images show the photographs of the films of bare Cu2O nanocubes and Cu2O@PNIPAM core-shell nanoparticles with the same solid content of 0.026 wt. % on PS substrates.

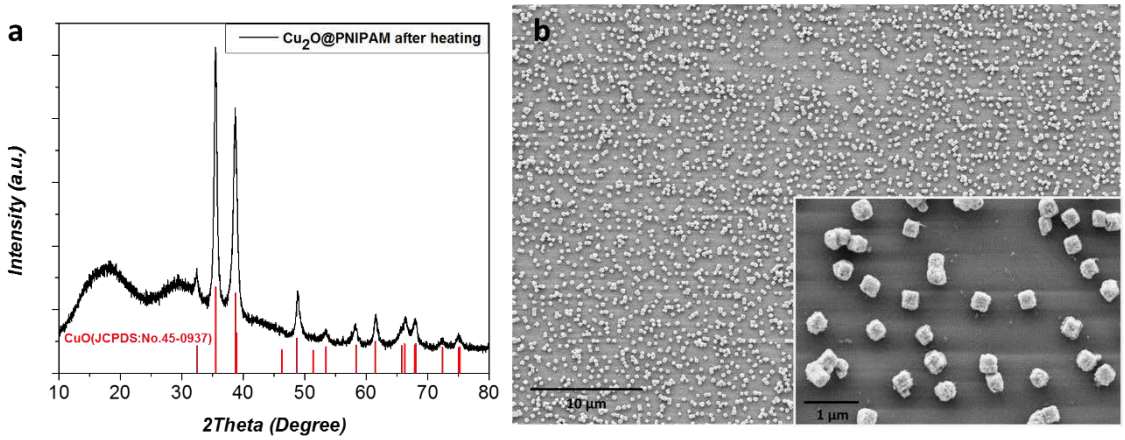

Figure 4.3.2 (a) XRD patterns and (b) SEM image of the Cu_2O@PNIPAM core-shell nanoparticles after heat treatment.

$$Z = \frac{\sqrt{a\rho\gamma}}{\eta} = Oh^{-1} \qquad \textbf{(4.3.1)}$$

where a is the radius of the printing orifice, ρ is the density of the ink, γ is the surface tension and η is the viscosity. Since in our work, the printing nozzle was not replaced, the properties of the ink will dominate the behavior of the droplets. Although the jettability range of Z is different for different ink materials, the printable range of Z is normally considered within $1<Z<14$.[164] If the value of Z is too high, a large number of satellite droplets will be formed, whereas if it is too low, the ink will need more energy to form a new drop near the nozzle tip, which will prevent the separation of a drop. According to the literature,[103] for the same ink system, the Z value of the ink is closer to the maximum value of the printable range, it is easier to form single droplets at higher frequencies and the travel velocity of the droplet will be increased, because of which the minimum stand-off distance between the nozzle and the substrate (MSD) will become shorter and the positioning error of the printing process will become smaller. The relevant physical parameters and corresponding Z values of the bare Cu_2O nanocubes and Cu_2O@PNIPAM core-shell nanoparticles with different solid content at 20°C have been listed in Table 4.3.1.

With the same solid content of 1.5 wt. %, the Cu_2O@PNIPAM core-shell nanoparticles contain lower surface tension and higher viscosity compared to the bare Cu_2O nanocubes, which leads to a lower Z value in the printable range. When the solid content of the bare Cu_2O nanocubes was increased from 1.5 wt. % to 8 wt. %, the Z value of the solution was adjusted within a reasonable range. Moreover, as shown in Figure 4.3.3, after being kept at room temperature for 30 mins, the droplet of the bare Cu_2O nanocubes with solid content of 1.5 wt.-% became

inhomogeneous and the upper portion of the droplet began to be clear. At the same time, the droplets of Cu_2O@PNIPAM core-shell nanoparticles solution with solid content of 1.5 wt. % and the pure Cu_2O nanocubes solution with solid content of 8 wt. % were still homogeneous. Thus, these two samples solution have been used as the ink to prepare the gas sensor devices by inkjet printing.

Table 4.3.1 The relevant physical parameters and corresponding Z values of the bare Cu_2O nanocubes and Cu_2O@PNIPAM core-shell nanoparticles with different solid content at 20°C (the diameter of the printing orifice is 25μm).

Sample	Viscosity η(mPa•s)	Density ρ (g/cm^3)	Surface tension γ (mNm^{-1})	Z (1/Oh)
Cu_2O nanocubes (1.5 wt.-%)	1.33	1.015	69.2	22.3
Cu_2O@PNIPAM (1.5 wt.-%)	1.83	1.015	42.7	12.7
Cu_2O nanocubes (8 wt.-%)	2.22	1.08	61	12.9

As shown in Figure 4.3.4a and c, the particles were printed on the interdigitated electrode structures, which form part of a micromachined hotplate device to do the gas sensor measurement. Before the heating treatment, although most of the particles were buried inside the PNIPAM shells which can be observed as the black layer covered on the electrode in Figure 4.3.4a, it is still possible to see that the Cu_2O@PNIPAM core-shell nanoparticles were uniformly dispersed on the surface of the device.

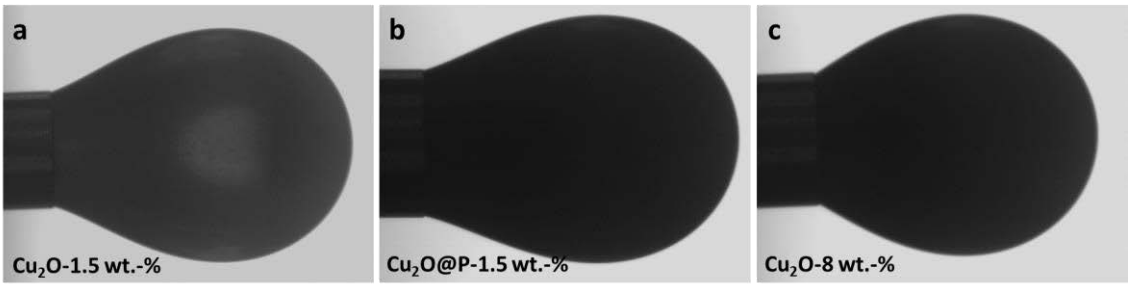

Figure 4.3.3 The photos of the droplets kept for 30 min for different samples: (a) bare Cu_2O nanocubes with 1.5 wt.% solid content, (b) Cu_2O@PNIPAM core-shell nanoparticles with 1.5 wt.% solid content and (c) bare Cu_2O nanocubes with 8 wt.% solid content.

After the high temperature treatment at 400 °C for one hour in the air, the PNIPAM shells were burned off and a clear and uniform layer of CuO was presented (see Figure 4.3.4b). From the insert SEM image in Figure 4.3.4b, the spaces generated from the removal of PNIPAM shells between each of the CuO nanocubes can be observed clearly. Moreover, due to the protection of PNIPAM during the high temperature treatment, the cubic shape of the nanoparticles was perfectly preserved. In contrast, without the modification of PNIPAM shell, the pure Cu_2O nanocubes aggregated together before heating treatment and many blank areas without particles can be found on the surface of the device (see Figure 4.3.4c). After high temperature treatment, a lot of large particles were found in the system as shown in the insert SEM image in Figure 4.3.4d, which indicates that the cubic structures have been destroyed. This phenomenon can be rationalized by the generation of CuO nanostructures. Without the PNIPAM shells, the Cu_2O nanocubes aggregated together and during the process of the transition from Cu_2O to CuO, the aggregated Cu_2O nanocubes regrow into larger CuO nanoparticles, which destroys the cubic nanostructures.

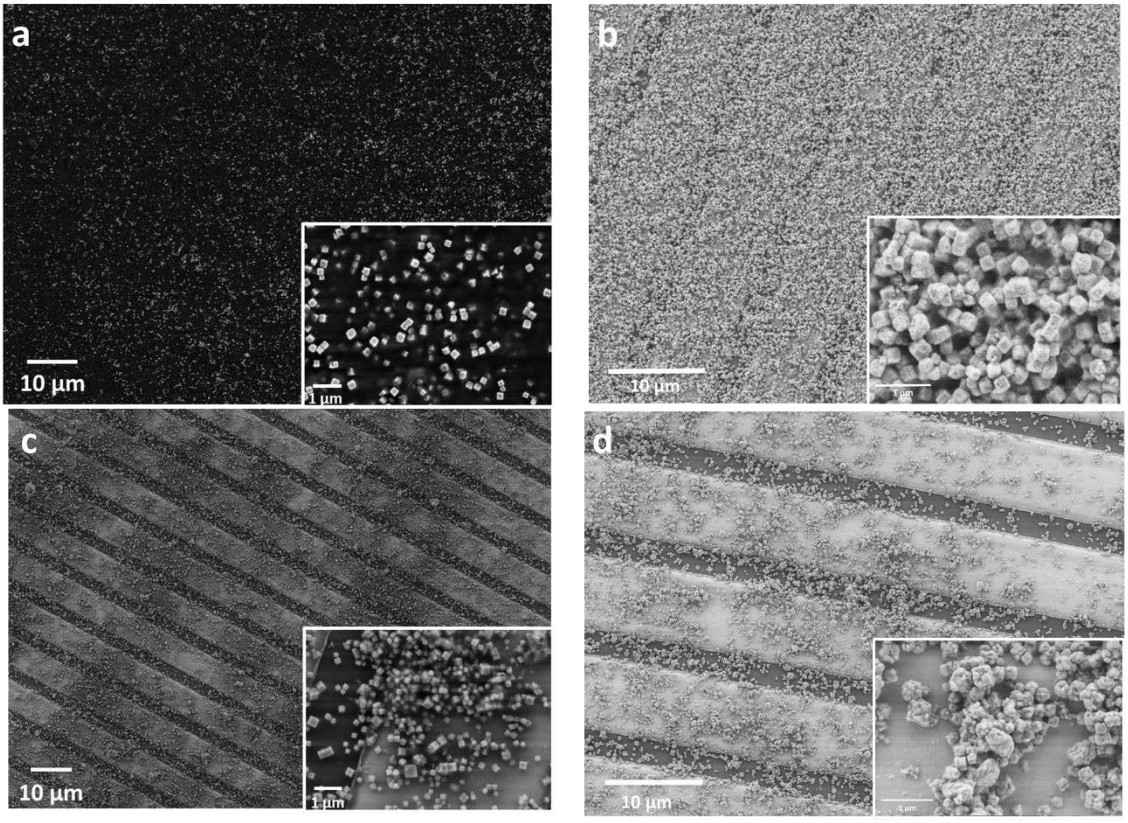

Figure 4.3.4 (a,b) SEM images of gas sensor device of Cu_2O@PNIPAM core-shell nanoparticles before and after heating treatment. (c,d) SEM images of gas sensor device of Cu_2O nanocubes before and after heating treatment.

Figure 4.3.5 shows the sensing response of the CuO gas sensor devices made from the bare Cu_2O nanocubes and the Cu_2O@PNIPAM core-shell nanoparticles, respectively. At a typical elevated temperature of 300 °C, the sensors were exposed to varying levels of 0.5 -10 ppm NO_2 in dry synthetic air. At the given temperature, both of the devices show a typical p-type sensing behavior with respect to the oxidizing nature of NO_2. The device prepared from the core-shell nanoparticles features a faster response and recovery characteristic upon alternating NO_2 exposure and purging with synthetic air. The baseline resistance is distinctly below the MΩ range, favorable for dedicated circuitry. This can be explained as the follows: with the regular and ordered intra-particle arrangement, the gas sensor device made from the core-shell particles promotes the current flow. On the contrary, the bare particles aggregated into larger yet sparser and random bulky particles during the heating treatment which resulted in a higher baseline resistance. The experiments were conducted for different operation temperatures. Figure 4.3.5a shows the response characteristic of three similar sensing elements made from the core-shell nanoparticles at operation temperatures of 300°C and 350°C, which is defined as the ratio of baseline resistance in dry synthetic air and the resistance upon NO_2 exposure (R_0/R). The concentration dependent response follows a typical power law $R_0/R = 1+A*C_{NO2}^{b}$,[184] with an exponent b=0.35 for both temperatures. The comparison reveals a significant temperature dependence in sensitivity.

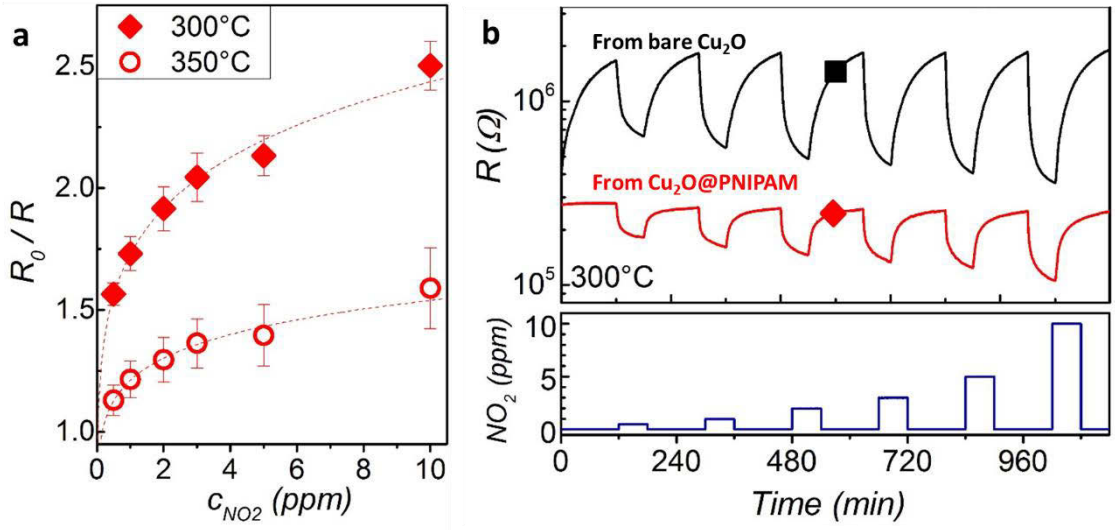

Figure 4.3.5 (a) Response characteristics of core-shell nanoparticle sensing devices for operation temperatures at 300°C and 350°C can be described by a typical power-law and reveal a distinct temperature dependency of sensitivity. (b) Comparison of the sensing characteristics of bare CuO nanocubes and CuO nanocubes from Cu_2O@PNIPAM core-shell nanoparticles gas sensors towards increasing NO_2 levels.

5. In-situ generation of Au nanoparticles in the PVCL- α-CD microgels

5.1 Synthesis and Characterization of PVCL-α-CD-Au hybrid microgels

Due to the availability of free spaces in the swollen networks of the microgels, PVCL can provide excellent nucleation and growth environment for nanoparticles without aggregation.[58] Moreover, because the amide group of PVCL can transform to enol structure under alkaline conditions, PVCL can be used for in-situ synthesis of gold nanoparticles without additional strong reducing agent.[152–154] This process has been shown in Figure 5.1.1. PVCL was obtained by compolymerization of *N*-vinylcaprolactam (VCL) with toacetoxyethyl methacrylate (AAEM) using *N*,*N*'-methylene-bis-acrylamide as crosslinker. After being mixed with $HAuCl_4$ solution for several hours, gold precusor can be adsorbed on the polymer chains. Then NaOH solution was added into the mixture to adjust the pH of the solution to 10. At this pH value, the amide group can transform to enol structure with a hydroxyl group. Like long-chain alcohols, this kind of functional group can work as the reducing agent for the synthesis of Au nanoparticles.

As shown in Figure 5.1.2a, monodisperse Au nanoparticles have been prepared via the reduction of $HAuCl_4$ by PVCL microgels without adding any other reducing agent. The obtained Au nanoparticles are rather uniform in size and shape. The formation of the Au nanoparticles can be also followed by the color change from light yellow to wine-red of the solution.

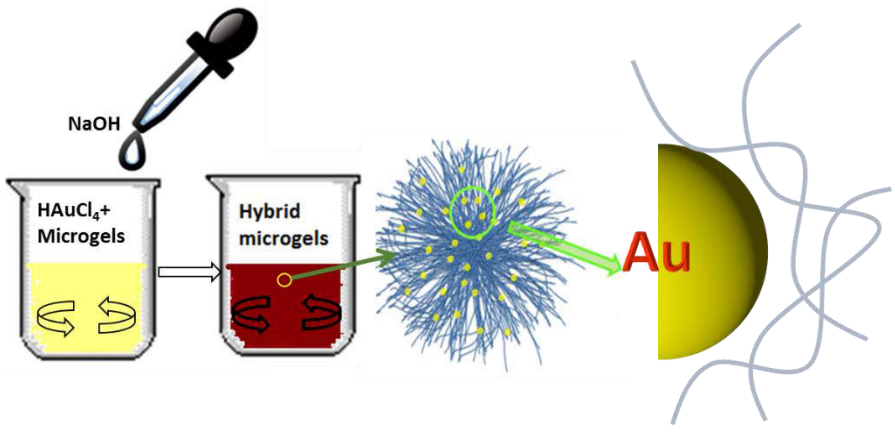

Figure 5.1.1 Schematic illustration of the procedure used to synthesize PVCL-Au hybrid microgels.

As shown in the UV-vis spectra in Figure 5.1.2b, the presence of a clear plasmon absorption peak at around 530 nm further confirms the formation of Au nanoparticles in the PVCL microgels. In a control experiment, no reduction of Au has taken place in the reaction solution in the absence of microgel particles. The color of the $HAuCl_4$ and NaOH mixture was kept light yellow after days and no obvious absorbance can be found in the UV-vis spectra (Figure 5.1.2b). In addition, it can be seen from the TEM image that lots of Au nanoparticles are formed outside microgels. This is due to the reason that the interaction between the polymer chains of PVCL and the Au nanoparticles is not strong enough to immobilize all of the Au nanoparticles inside the microgels.

Considering that the hydroxyl groups in the molecular structure of the cyclodextrins can provide an efficient capping on the surface of Au nanoparticles based on the Au-COO^- interaction,[185,186] PVCL microgels functionalized with different amount of α-cyclodextrin units have been synthesized for the preparation of novel hybrid microgels. The PVCL-α-CD microgels were fabricated according to the literature from Pich and his co-works.[187] Firstly, α-CD has been modified with acrylate. Then different amount of α-CD acrylate was grafted into the PVCL networks by copolymerization.

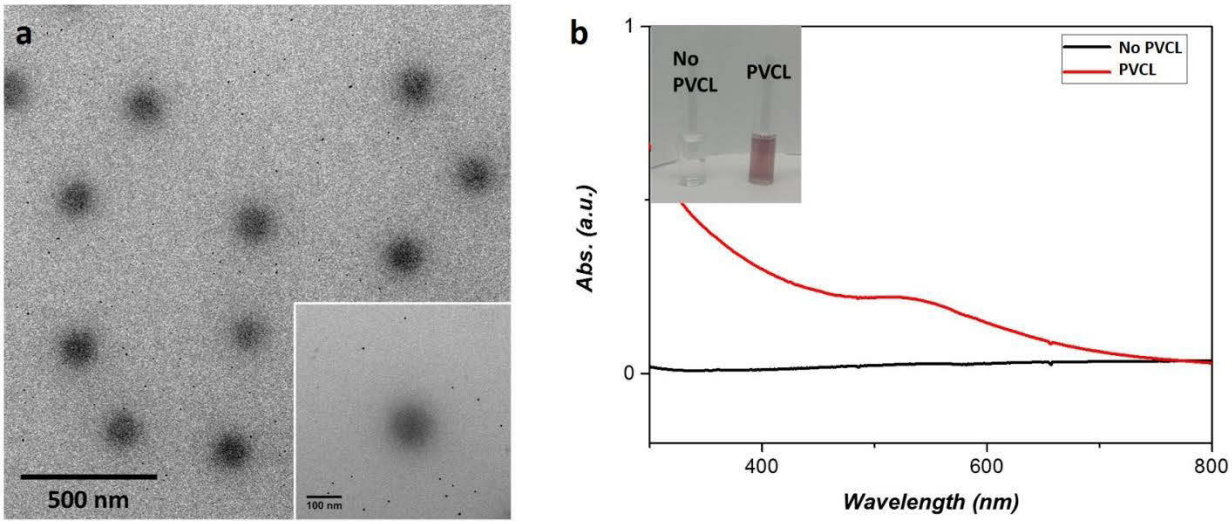

Figure 5.1.2 (a) TEM image of PVCL-Au hybrid microgels, (b) UV-vis absorption spectra of the $HAuCl_4$ and NaOH mixture solution (mixing for 72 hours) with and without PVCL microgels.

Two samples with different α-cyclodextrin contents were prepared. The amount of α-CD in the microgels was determined to be 1.03 and 13.08 wt.-% by FI-IR spectra (see Figure 5.1.3a and b), respectively. The band at 1032 cm^{-1} relates to the C-O-C vibrations of the glucose units of CD, which indicates the incorporation of CD in PVCL. Figure 5.1.3b shows that with the

increase of the concentration of CD in PVCL, the intensity of the band at 1032 cm^{-1} increases as well.

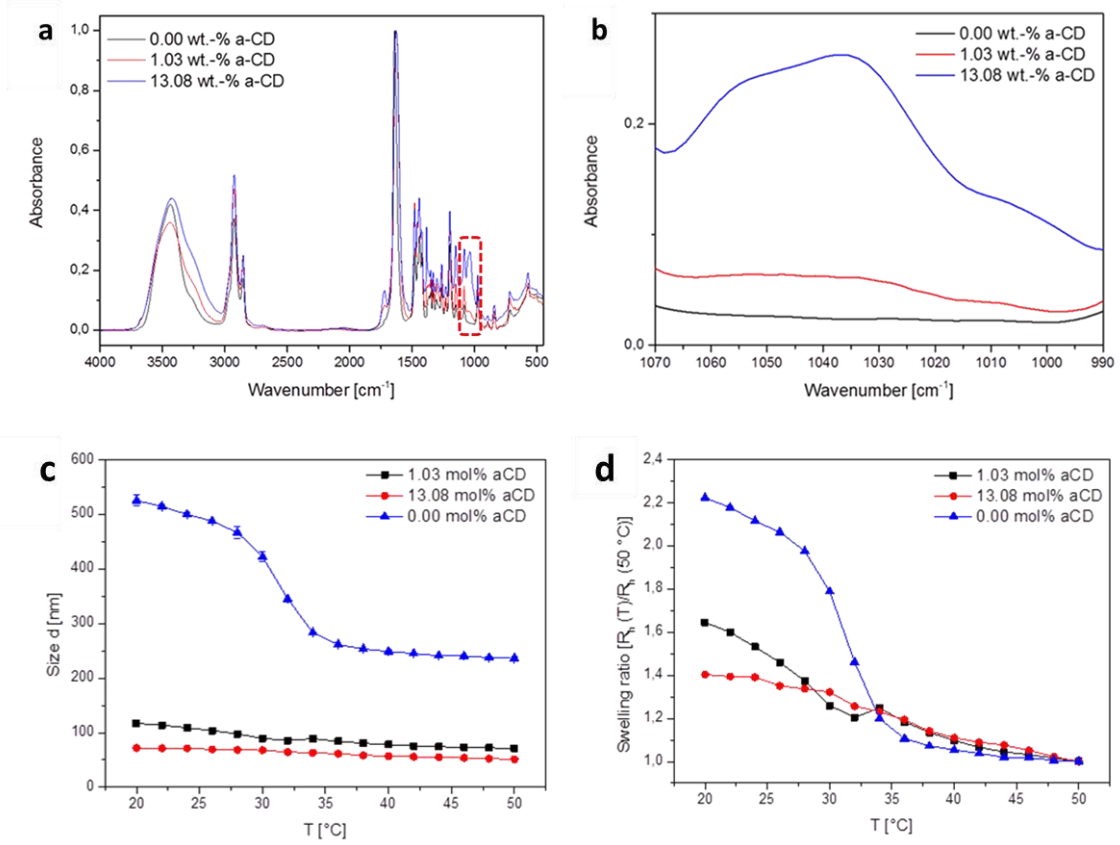

Figure 5.1.3 FT-IR spectra of pure PVCL, PVCL-α-CD(1.03 wt.-%) and PVCL-α-CD(13.08 wt.-%), (a) whole spectrum, (b) absorbance of C-O-C group of cyclodextrin around 1034 cm^{-1}. (c) Temperature dependent DLS measurement of pure PVCL, PVCL-α-CD(1.03 wt.-%) and PVCL-α-CD(13.08 wt.-%), (d) Swelling ratio of pure PVCL, PVCL-α-CD(1.03 wt.-%) and PVCL-α-CD(13.08 wt.-%).

The synthesized polymer particles show a decrease in size with higher CD contents, compared with the decrease of swelling ratio (see Figure 5.1.3 c and d). This phenomenon can be explained as the follows: the α-CD grafted into the network of microgels can be considered as the crosslinker point. With the increasing amount of α-CD inside the microgels, the crosslinking degree of the PVCL microgels increases, which leads to the increasing of the rigidity of the microgels. Since the amount of monomers used for the polymerization is the same, the microgels with higher rigidity contain lower swelling radio and smaller size at different temperatures. As shown in Figure 5.1.3d, the sample with 13.08 wt. % α-CD has the lowest swelling radio. The variation of the size of the microgels can be observed for both CD modified PVCL microgels in Figure 5.1.3c, which means the increasing amount of α-CD will not influence the themorsensitivity of the microgels.

The PVCL- α-CD (13.08 wt. %) was used as an "active" nanoreactor for the in situ generation of Au nanoparticles by direct reduction of hydrochloroauric acid in an alkaline aqueous solution. The process is the same with the PVCL without functionalizing α-CD. As shown in Figure 5.1.4a, monodisperse Au nanoparticles with an average diameter of 5~6 nm have been prepared via the reduction of $HAuCl_4$ by PVCL-CD microgels without adding any other reducing agent. The obtained Au nanoparticles, which are rather uniform in size and shape, are homogeneously immobilized in the PVCL-CD microgel carriers. A same conclusion can be drawn from the color changing of the solution and the UV-vis spectra of the hybrid microgels (see Figure 5.1.4 b). The presence of a clear plasmon peak at around 530 nm in the UV-vis spectra and the red color of the solution confirm the generation of the Au nanoparticles. Compared to the PVCL microgels without CD modification, in PVCL-CD-Au composite particles all of the Au nanoparticles are homogeneously distributed within the CD modified PVCL microgels and no secondary particles were found in the system. This is due to the reason that α-CD can provide an efficient capping on the surface of Au nanoparticles according to the Au-COO^- interaction. The interactions between the hydroxyl groups of α-CD and the Au surface were measured by FT-IR on a Si crystal. KBr pellets were avoided to minimize the water content of the sample. As shown in Figure 5.1.4c, a shift of 9 cm^{-1} to lower wavenumbers of the OH-absorption band is observed for PVCL- α-CD-Au, which represents the chemisorption between α-CD and Au according to the literature reports.[185,186]

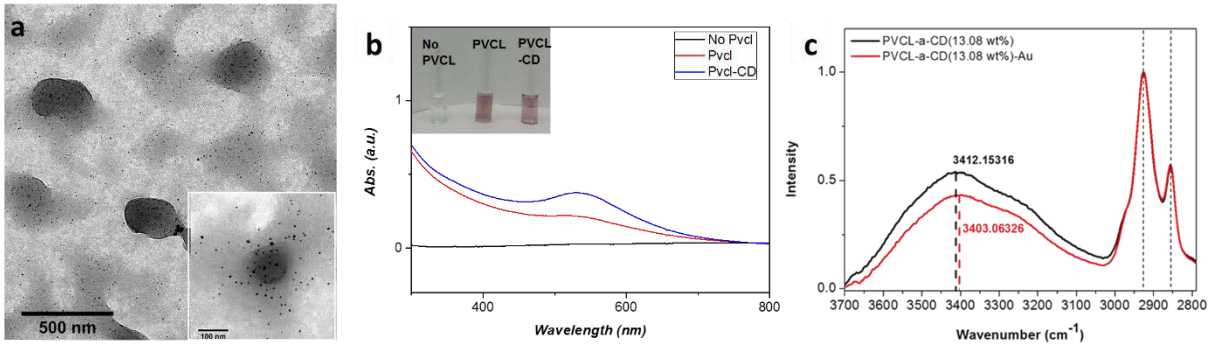

Figure 5.1.4 TEM images of (a) PVCL-α-CD(13.08 wt.-%)-Au microgel nanoparticles, (b) UV-vis spectra of the $HAuCl_4$ and NaOH mixture solutions with different amounts of PVCL and α-CD inside. The insert image is the photograph of the $HAuCl_4$ and NaOH mixture solutions with and without PVCL and α-CD inside. (c) FT-IR spectra of PVCL-α-CD(13.08 wt.-%) and PVCL-α-CD(13.08 wt.-%)-Au in the range of 3700-2750 cm^{-1}.

The effect of CD amount incorporated in the PVCL microgels on the formation of Au nanoparticles has been also studied. Comparing the TEM images shown in Figure 5.1.5a and

b, it can be seen that no obvious change in shape and morphology of the Au nanoparticles has been found by decreasing the CD concentration from 13.08 wt.-% to 1.03 wt.-%. Au nanoparticles with diameter of 5.5±0.3 nm have been generated in the PVCL-α-CD(1.03 wt.-%) microgel particles. Almost all of the Au nanoparticles are immobilized within the microgels.

The XRD patterns of these two PVCL-CD-Au samples are presented in Figure 5.1.5c. The peaks at 2θ = 38.34°, 44.22°, 64.88° and 77.76° correspond to (111), (200), (220) and (311) Bragg reflections of gold, which means the gold nanoparticles synthesized are face-centered cubic (*fcc*) structure. An estimation of mean size of Au nanoparticles was performed from the full width at half maximum of the (111) Bragg reflection using the Debye-Scherrer equation, which is 4.7 nm for PVCL-α-CD(13.08 wt.-%)-Au and 4.2 nm for PVCL-α-CD(1.03 wt.-%)-Au, respectively. This agrees well with the particle size determined from the TEM images.

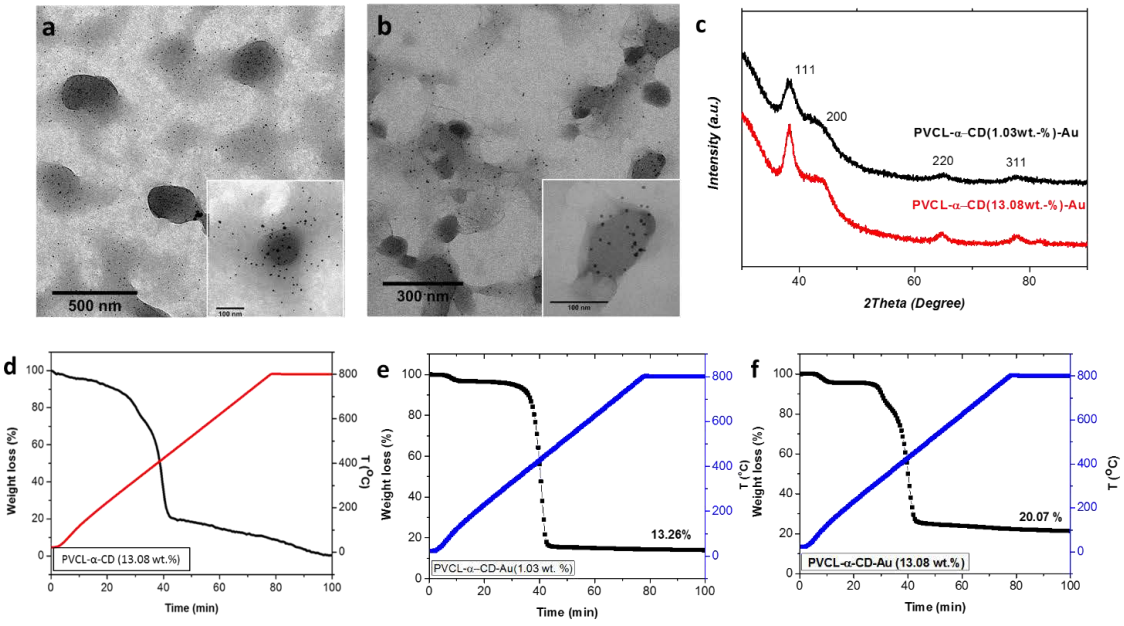

Figure 5.1.5 TEM images of (a) PVCL-α-CD(13.08 wt.-%)-Au microgel nanoparticles, (b) PVCL-α-CD(1.03 wt.-%)-Au microgel nanoparticles. (c) XRD patterns of PVCL-α-CD(1.03 wt.-%)-Au (black) and PVCL-α-CD(13.08 wt.-%)-Au (red). TGA spectra of (d) PVCL-α-CD (13.08 wt.-%) microgel, (e) PVCL-α-CD-Au (1.03 wt.-%), (f) PVCL-α-CD-Au (13.08 wt.-%).

Both TEM images and XRD patterns demonstrate that the Au nanoparticles reduced by PVCL microgels with different amount of CDs contain almost the same size and crystal mode. The amount of Au nanoparticles immobilized inside the microgels can be determined by TGA measurement. As shown in Figure 5.1.5 d to f, the amount of Au nanoparticles generated in the microgel is decreased from 20.07 wt.-% to 13.26 wt.-% when decreasing the CD concentration from 13.08 wt.-% to 1.03 wt.-%.

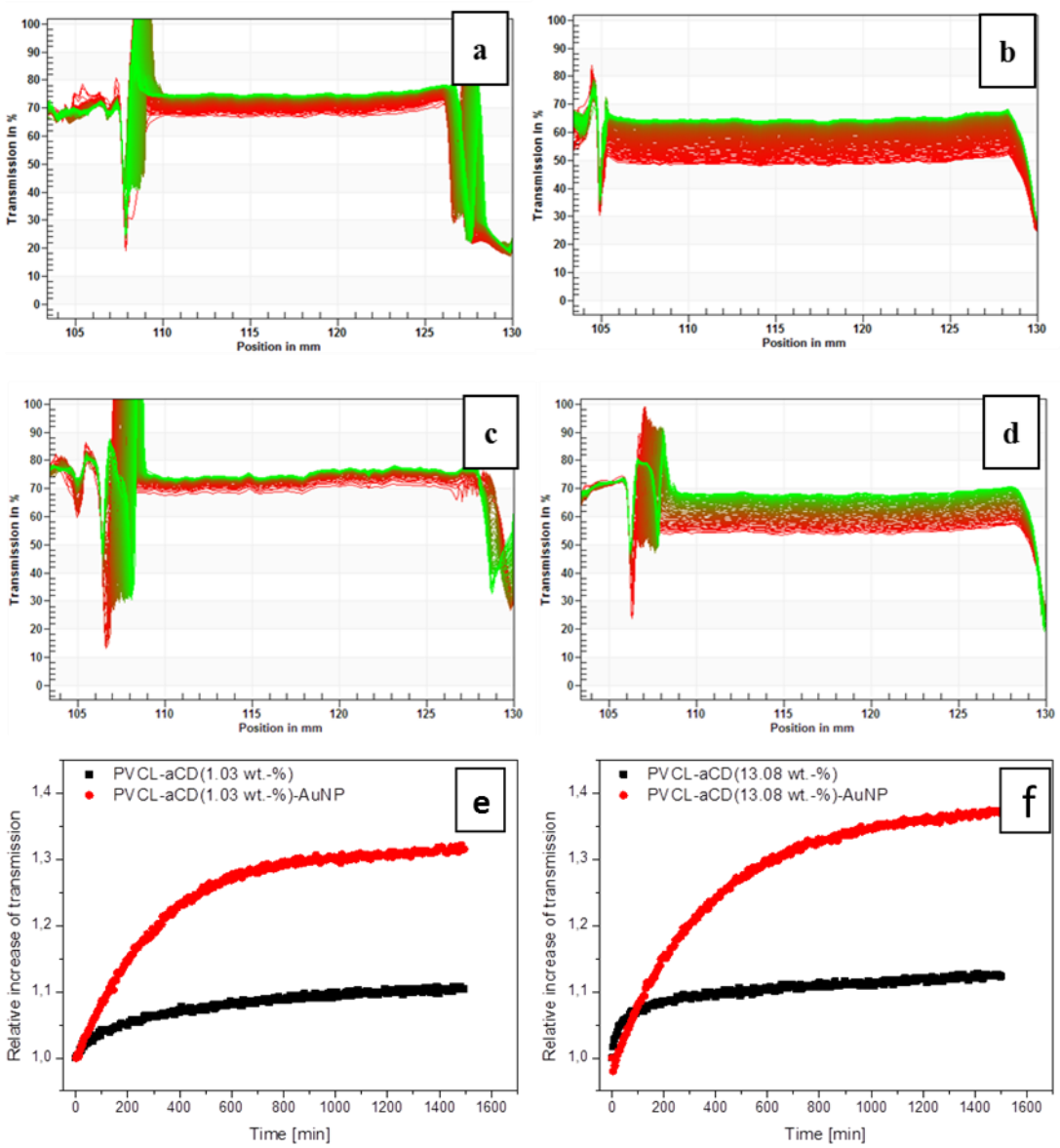

Figure 5.1.6 Raw data of LUMiSizer measurements of PVCL-α-CD(1.03 wt.-%) without (a) and loaded with Au-nanoparticles (b) and of the pure and loaded samples of PVCL-α-CD(13.08 wt.-%) (c and d). Relative increase of transmission of PVCL-α-CD(1.03 wt.-%) (e) and PVCL-α-CD(13.08 wt.-%) (f) without and loaded with Au-nanoparticles.

The colloidal stability of the hybrid microgels have also been studied by comparing the Au-loaded sample with its unloaded pure reference sample at 20 °C. As shown in Figure 5.1.6, the sedimentation velocity of both particle dispersions with and without gold nanoparticles was determined to measure the colloidal stability. The samples show a good colloidal stability in general as they do not precipitate completely with a relative low sedimentation velocity. Only a small decrease in stability has been observed for the microgels loaded with gold nanoparticls. For the hybrid microgels containing 1.03 wt.-% α-CD, the sedimentation velocity increased

from 0.0466 µm/s for unloaded microgels to 0.0522 µm/s for particles loaded with gold. For the other sample which contains 13.08 wt.-% α-CD, the sedimentation velocity increased from 0.0623 µm/s to 0.1147 µm/s. This demonstrates that the microgel dispersion does not lose its stability after deposition of gold nanoparticles, which is important for its use as catalyst system.

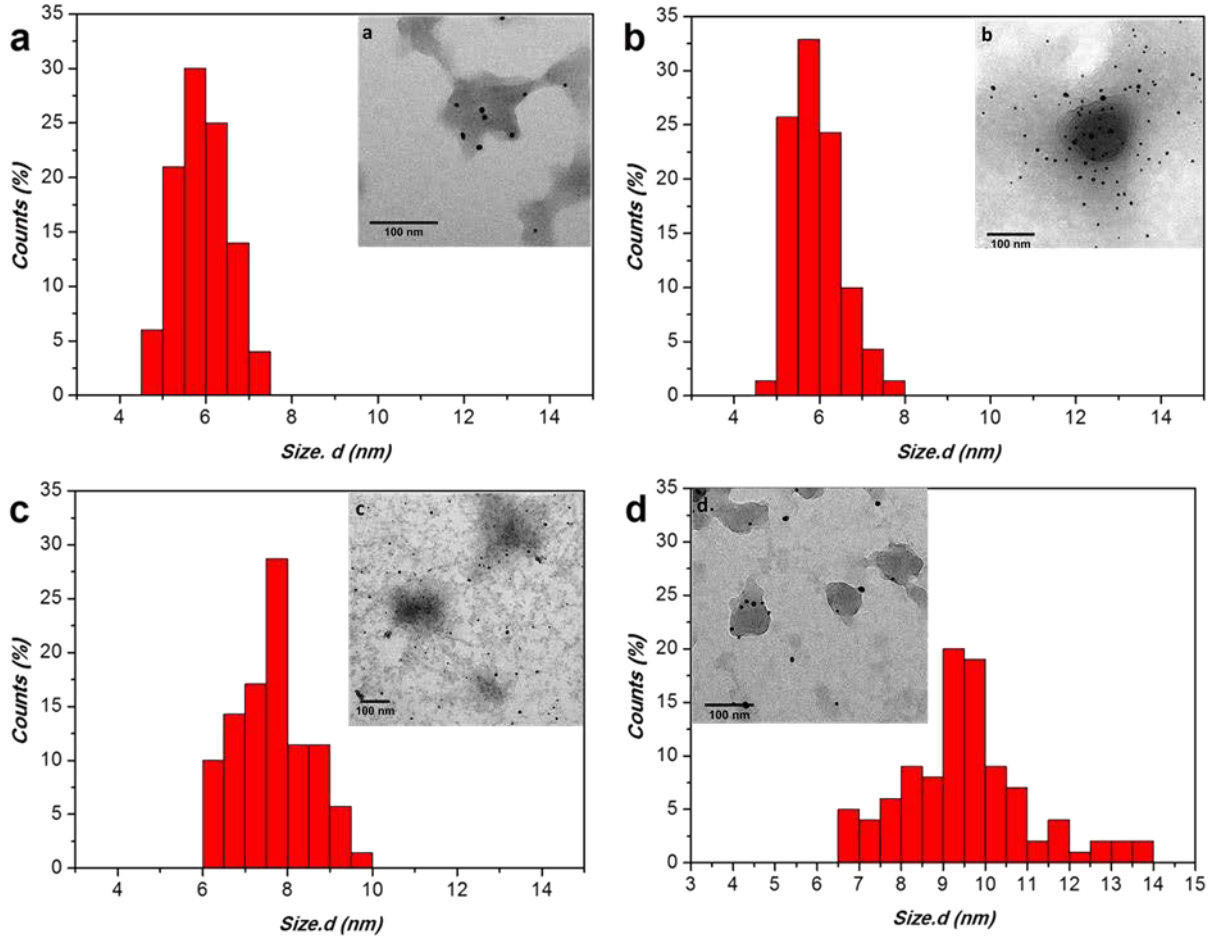

Figure 5.1.7 TEM images and size distribution of PVCL-CD-Au microgel particles synthesized with different amount of 0.01 M $HAuCl_4$: (a) 0.1 ml, (b) 0.2 ml, (c) 0.3 ml and (d) 0.4 ml.

Gold nanoparticles can be effectively immobilized inside the PVCL-α-CD microgels because of the chemisorption between cyclodextrins and gold nanoparticles via hydroxyl groups. The size of the Au nanoparticles can be controlled by changing the amount of Au precursors. As shown in Figure 5.1.7 and Table 5.1, keeping the amount of CDs incorporated in the microgels unchanged (13.08 wt.%), increasing of the amount of $HAuCl_4$ from 0.1 ml to 0.4 ml leads to an increase in the Au nanoparticle size from 6 nm to 9 nm. The UV-vis spectra of the PVCL-CD-Au nanoparticles prepared at different $HAuCl_4$ concentrations show us the same result. From the UV-vis spectra presented in Figure 5.1.8, it is found that the surface plasmon resonance (SPR) band of the Au nanoparticles red-shifted from 529 nm to 532 nm with band

broadening when the $HAuCl_4$ concentration was increased from 4×10^{-4} M to 1.6×10^{-3} M, which indicates the size of the gold nanoparticles becomes bigger. In addition, there is a continuous increase of the absorption intensity of the absorption band, which is in good agreement with the finding that the amount of the Au nanoparticles increased with increasing $HAuCl_4$ concentration as shown in table 5.1.

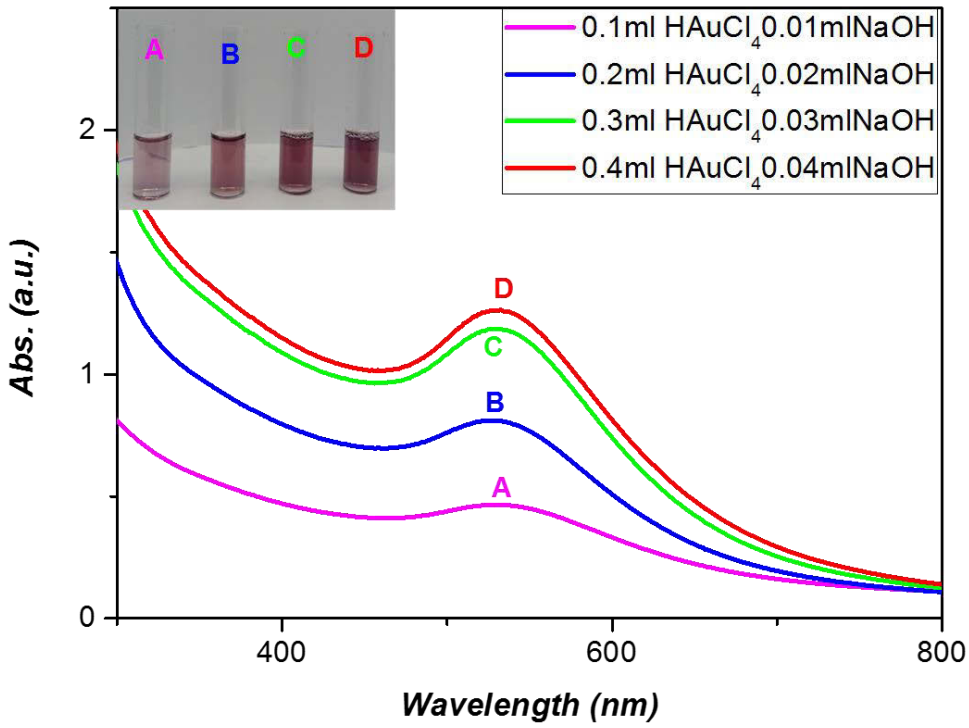

Figure 5.1.8 UV-vis spectra of PVCL-α-CD-Au microgel particles solutions with different amounts of $HAuCl_4$. The insert image is the photograph of the PVCL-α-CD-Au microgel particle solutions with different amount of $HAuCl_4$.

Moreover, when the amount of $HAuCl_4$ is increased to 0.4 ml, some secondary Au nanoparticles have been found in the system as shown in Figure 5.1.7d. This can be explained as the follows. As shown in Figure 5.1.9, α-CDs were adsorbed on the surface of Au nanoparticles due to the chemisorption with Au-COO^-, because of which α-CDs can be considered as the surfactant for the generation of Au nanoparticles. Since the ratio of the α-CDs in the hybrid microgels is constant, the excess gold nanoparticles will release from the hybrid microgels due to less interaction between the gold nanoparticles and the microgels. Thus, sample 2 in table 5.1 was selected for the following experiments, which shows the smallest size of Au nanoparticles and no secondary particles in the system.

Table 5.1 Synthesis of PVCL-CD-Au hybrid particles with different concentration of $HAuCl_4$ in the presence of PVCL- α-CD (13.08 wt.-%) microgels (Solid content 1.06 wt.-%).

Number	$HAuCl_4$ (0.01M)	NaOH (1.0M)	PVCL-α-CD	Au loading (wt.-%) (from TGA)	d_{Au} (nm) (from TEM)
1	0.1 ml	0.01 ml	1 ml	16.98	6.0±0.3
2	0.2 ml	0.02 ml	1 ml	20.07	5.9±0.3
3	0.3 ml	0.03 ml	1 ml	19.85	7.7±0.4
4	0.4 ml	0.04 ml	1 ml	21.52	9.4±0.5

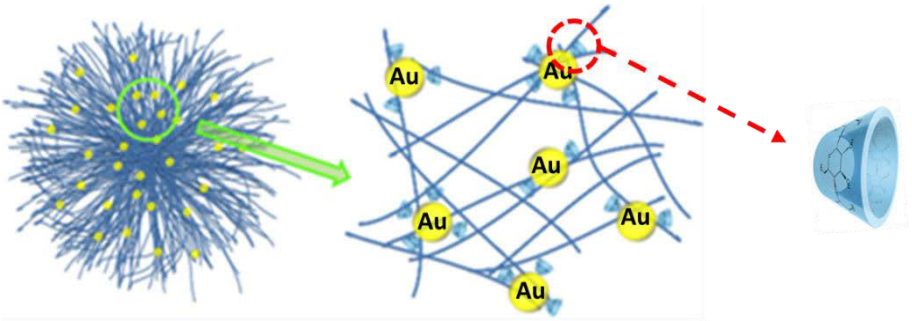

Figure 5.1.9 Schematic overview of the immobilization of Au-nanoparticles in α-CD modified PVCL microgel.

As discussed above, PVCL-α-CD microgels exhibit thermosensitive properties (see in Figure 5.1.3 c). Figure 5.1.10 shows the hydrodynamic radii of the microgel particles before and after Au loading as a function of temperature. The Au-loaded microgel particles show similar volume phase transition temperature (VPTT) behavior as that of the bare PVCL- α-CDs networks. This result indicates that the immobilization of Au nanoparticles does not influence the thermosensitive properties of PVCL-α-CDs microgels and proves additionally good distribution of Au in the microgels. Moreover, a much sharper volume transition at 27.5°C can be observed for the PVCL-α-CD-Au particles. As we described above, α-CDs can be considered as the crosslinker points in the microgels. When the gold nanoparticles were fabricated inside the microgels, the amount of α-CDs as crosslinking units was decreased, which leads to a sharper volume transition at 27.5°C.[6]

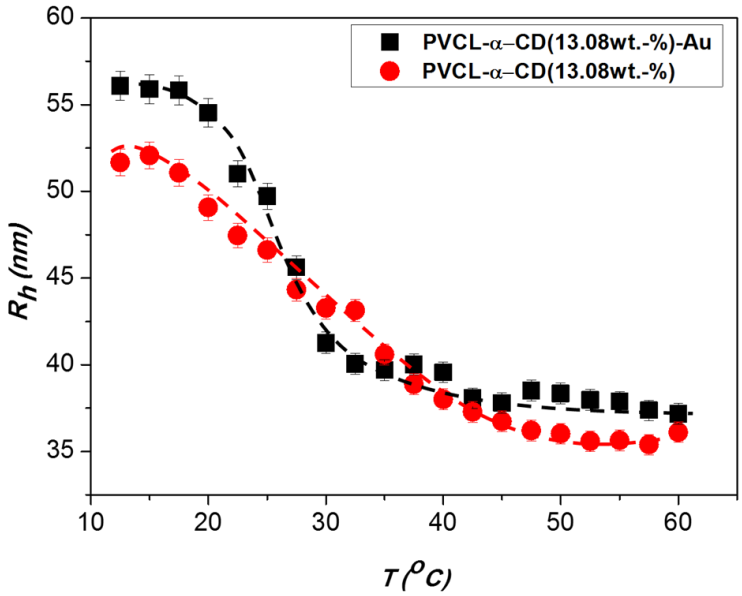

Figure 5.1.10 Hydrodynamic radius of PVCL-α-CD(13.08 wt.-%) microgels with and without Au nanoparticles as a function of temperature in aqueous solution.

5.2 Catalytic activity of hybrid microgels

As stated in the introduction part, stimuli-responsive microgels loaded with different kinds of metallic nanoparticles can be used as nanoreactor for different catalytic reactions. Here, we have demonstrated for the first time that the thermo-sensitive PVCL microgels modified with CD molecules can work efficiently as reducing agent and capping agent for the synthesis of gold nanoparticles. Moreover, because of the different complexation abilities of CDs with aromatic nitro compounds with various structures, the Au nanoparticles could show specific/selective binding abilities to certain reagents resulting in enhanced catalytic activity.

5.2.1 Catalytic reduction of 4-nitrophenol

The catalytic reduction of 4-nitrophenol by borohydride has been chosen as the model reaction to test the catalytic activity of the PVCL-CD-Au hybrid microgels. The reduction of 4-nitrophenol (Nip) is one of the most often used reactions.[13,31] It can be easily monitored by UV-vis spectroscopy accurately. Firstly the Nip was mixed with excessive borohydride and then different amount of hybrid microgels as the catalyst was added into the mixture. The kinetics of 4-nitrophenol reduction in the presence of hybrid microgels was followed by UV-vis spectroscopy. As shown in Figure 5.2.1.1 b, after the addition of PVCL-α-CD(13.08 wt.-%)-Au hybrid microgels, the peak at 400 nm, which represents the 4-nitrophenate ions, decreases gradually with time and a new peak appears at 290 nm, which comes from the product 4-aminophenol. Because the BH_4^- is more than needed, the reaction follows a pseudo-first order

reaction. The ratio of the concentration c of the 4-nitrophenol at time t to its original concentration c_0 can be directly given by the ratio of the respective absorbance A/A_0. As shown in Figure 5.2.1.1 a, linear relations between $\ln(c/c_0)$ versus time have been obtained in the presence of different amount of PVCL-α-CD(13.08 wt.-%)-Au catalyst. The apparent rate constant k_{app} is taken from the slope of these linear sections.[128]

Because the catalytic reaction happens on the surface of the Au nanoparticles, the catalytic activity depends on the total surface S of the Au nanoparticles immobilized every unit volume of the PVCL-CD microgels. Thus, in order to exclude the influence of particle size, a kinetic constant k_1 can be defined through normalization to the total surface of the nanoparticles in the system[129]:

$$\frac{dc_{Nip}}{dt} = -k_{app}c_{Nip} = -k_1 S c_{Nip} \qquad \textbf{(5.2.1)}$$

where c_{Nip} is the concentration of 4-nitrophenol and S is the total surface of the nanoparticles in the reaction mixture, respectively. Here the normalized rate constants k_1 can be used for direct comparison.

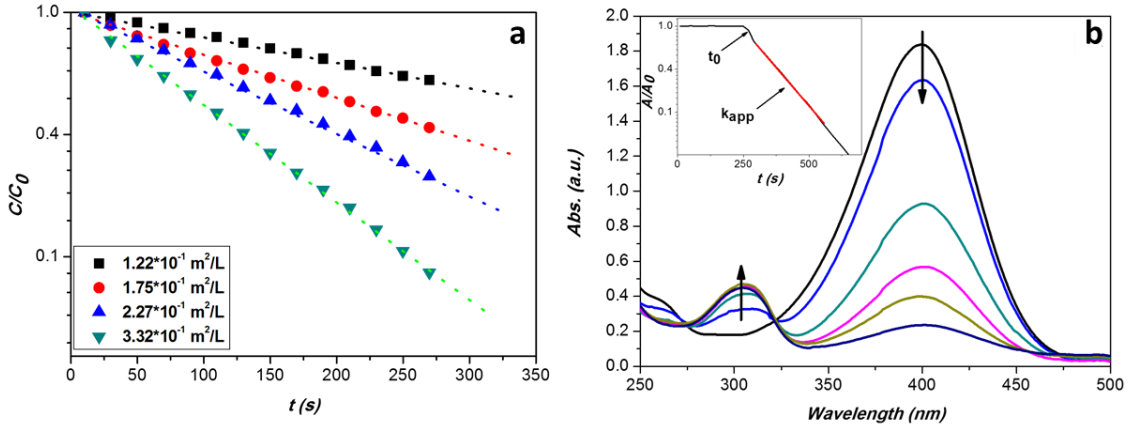

Figure 5.2.1.1 (a) Kinetic analysis of the reduction of Nip using different amount of PVCL-α-CD(13.08 wt.-%)-Au hybrid microgel particles as catalyst at room temperature. (b) UV-vis absorption spectra of Nip reduced by sodium borohydride using PVCL-α-CD(13.08 wt.-%)-Au particles as catalyst at room temperature. The inset shows typical time dependence of the absorption of 4-nitrophenolate ions at 400 nm.

As shown in Figure 5.2.1.2 b, k_1 of 0.025 $Ls^{-1}m^{-2}$ has been determined for the PVCL-α-CD(13.08 wt.-%)-Au particles. In comparison, CTAB-stabilized Au nanoparticles (see Figure 5.2.1.2 a) and PVCL-α-CD(1.03 wt.-%)-Au have been also used as the catalysts for the same

reaction. As shown in Figure 5.2.1.2 b, both of the PVCL-α-CD(13.08 wt.-%)-Au and the PVCL-α-CD(1.03 wt.-%)-Au contains a higher reaction rate than that of CTAB-stabilized Au nanoparticles and the reaction rate of the hybrid microgels modified with more α-CDs is slightly faster than that of the microgels modified with less α-CDs. The related reaction rate and particle size have been listed in table 5.2.

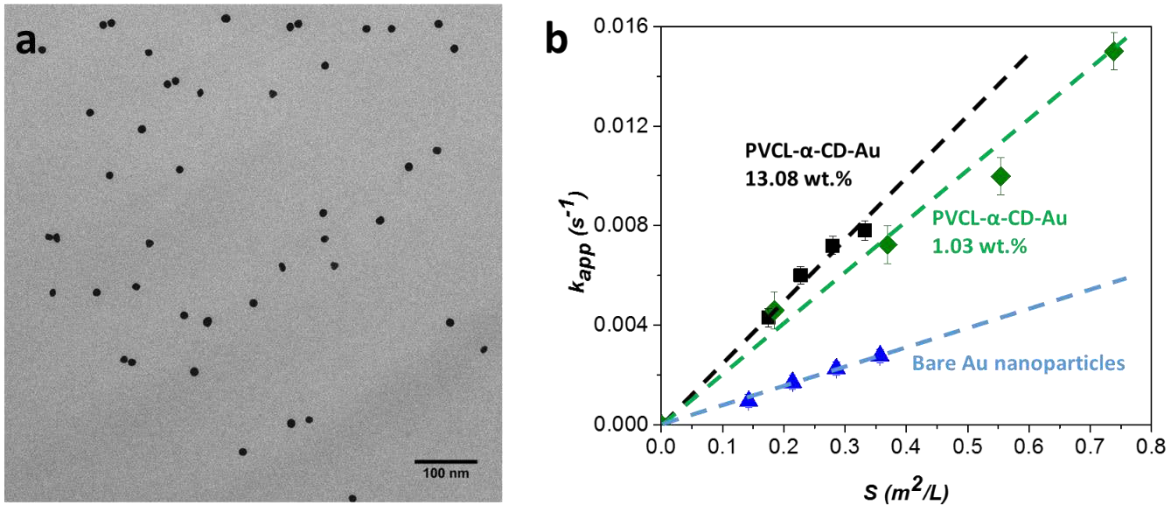

Figure 5.2.1.2 (a)TEM image of CTAB-stabilized Au nanoparticles with radius of around 5 nm. (b) Rate constant (k_{app}) as a function of surface area of Au nanoparticles normalized to the unit volume of the system: PVCL-α-CD(13.08 wt.-%)-Au (squares), PVCL-α-CD(1.03 wt.-%)-Au (diamonds) and bare Au nanoparticles (triangles) at room temperature.

As we described before, the size and crystal form of the Au nanoparticles in these two hybrid microgels systems are similar. The only difference between hybrid microgel systems is the amount of the CDs grafted in the PVCL microgels. Since nitrophenol has been proved to have complexation with cyclodextrin in aqueous solution,[6] which will lead to the increase of the concentration of Nip around the surface of Au nanoparticles, the amount of α-CDs grafted in the system will directly affect the catalytic reaction rate with Nip.

The complexation between α-CD and Nip can be easily monitored by UV-vis spectroscopy accurately. Such guest-host complex leads to the shift of the peak of Nip in the UV-vis spectra due to the transfer of the chromophore of the Nip from a polar aqueous environment to a hydrophobic environment within the α-CD cavity. In our study, UV-vis spectra have been taken by mixing Nip solution with different target systems. As shown in Figure 5.2.1.3 a and Figure 5.2.1.3 b, the characteristic peak of Nip did not shift after mixing with bare PVCL microgels and CTAB-Au, which means there is no complexation between Nip and targets.

Table 5.2 Rate constant k_1 of different catalysts for the reduction of 4-nitrophenol (Nip)

Sample	Reduction of Nip k_1 ($Ls^{-1}m^{-2}$)	d_{Au} (nm) (from TEM)
PVCL-α-CD(13.08 wt.-%)-Au	0.025	5.9±0.3
PVCL-α-CD(1.03 wt.-%)-Au	0.020	5.5±0.3
CTAB-stabilized Au	0.008	10.9±0.4

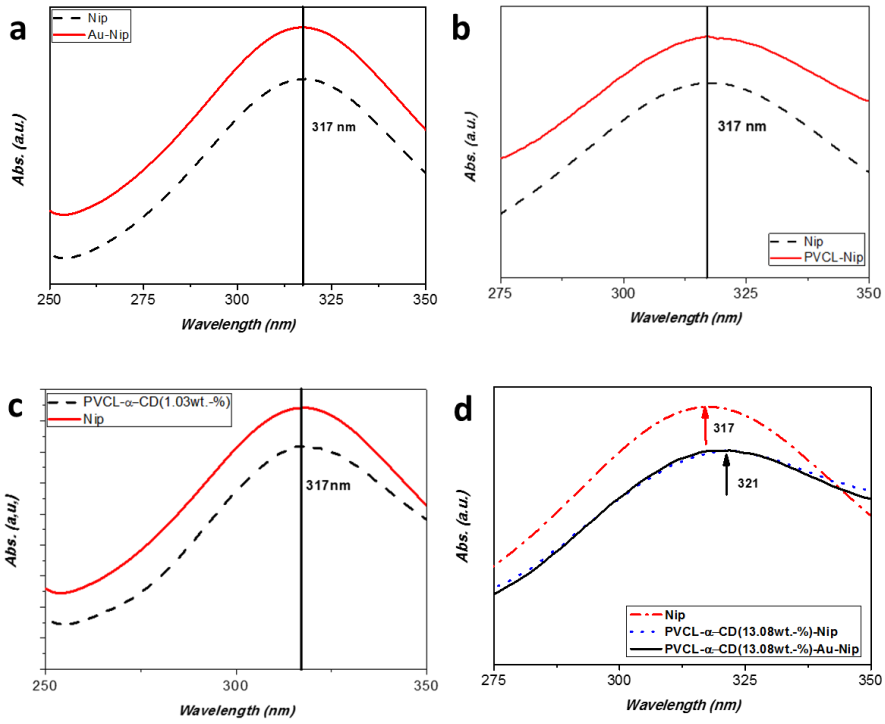

Figure 5.2.1.3 (a) The UV-vis spectra of 4-nitrophenol: Black, pure 4-nitrophenol; Red, mix with CTAB-stabilized Au nanoparticles with radius of around 5 nm. (b) UV-vis spectra of Nip mixed with PVCL (solid line) and pure Nip (dash line). (c) UV-vis spectra of Nip mixed with PVCL-α-CD(1.03 wt.-%) microgels (dash line) and pure Nip (solid line). (d) UV-vis spectra of Nip mixed with PVCL-α-CD(13.08 wt.-%)-Au microgels(solid line); PVCL-α-CD(13.08 wt.-%) microgels (dot line) and pure Nip (dash dot line). Concentrations: Nip: 10^{-5} mol/L; microgels: 0.203 mg/ml.

In comparison, the characteristic peak of Nip shifted from 317 nm to 321 nm when PVCL microgel modified with 13.08 wt.-% α-CD is added as shown in Figure 5.2.1.3 d. Similar shift can be also found for the PVCL-α-CD(13.08 wt.-%) microgels after the immobilization of Au nanoparticles. Moreover, when the amount of α-CDs in the PVCL microgels is too less, this

shift of the characteristic peak disappears as shown in Figure 5.2.1.3 c for the PVCL-α-CD (1.03 wt.-%), which means the complexation is weakened with the decreasing of the amount of α-CDs in the system.

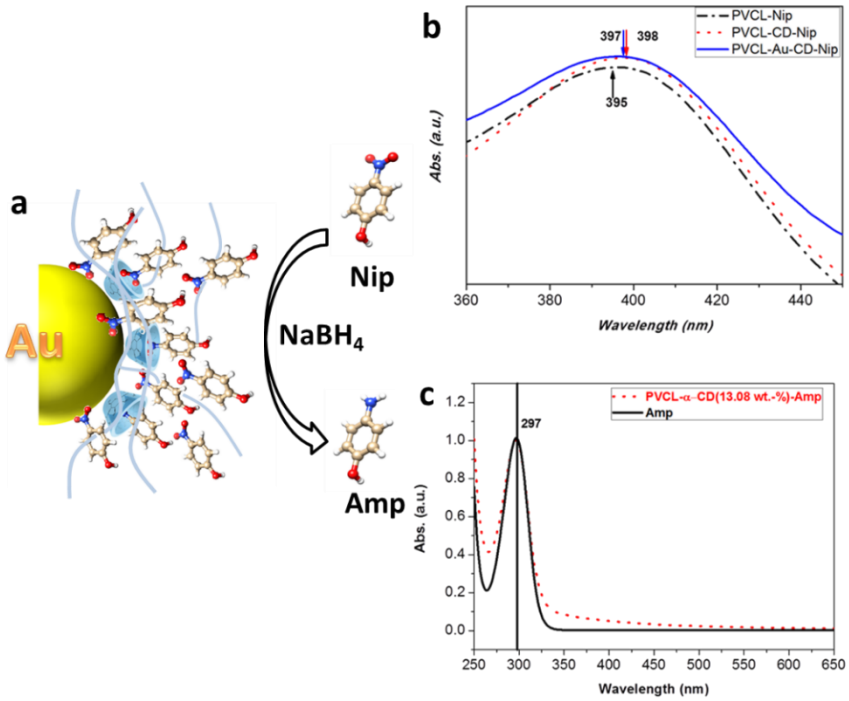

Figure 5.2.1.4 (a) Schematic illustration of the reducing procedure of Nip by PVCL-α-CD-Au hybrid microgels. (b) UV-vis spectra of Nip mixed with PVCL (dash dot); PVCL-α-CD(13.08 wt.-%)-Au microgels (solid line); PVCL-α-CD(13.08 wt.-%) microgels (dotted line). Concentrations: Nip: 10^{-5}mol/L; microgels: 0.203mg/ml; pH=10. (c) UV-vis spectra of Amp mixed with PVCL-α-CD (13.08 wt.-%) (dot line) and pure Amp (solid line).

Since the catalytic reaction of Nip is carried out under alkaline conditions, the complexation between α-CDs and PVCL-α-CD-Au (13.08 wt.-%) hybrid microgels has been also measured at high pH value. As shown in Figure 5.2.1.4 b, a similar red-shift of approximate 3 nm was found in the UV-vis spectra when PVCL modified with α-CD(13.08 wt.-%) was mixed with Nip at pH 10, which means such kind of complexation still exists under alkaline condition that the reduction of Nip starts with. In addition, according to the literature, the complexation between α-CD and 4-aminophenol (Amp), which is the reduction product, is not so stable as the Nip. As shown in Figure 5.2.1.4 c, no shift of the characteristic peak can be observed for the 4-aminophenol solution mixed with the PVCL-α-CD (13.08 wt.-%) microgels, which demonstrates that it is hard for the α-CDs to form host-guest complex with 4-aminophenol. This indicates that the product cannot occupy the cavities of α-CDs to influence the reaction speed.

The mechanism of the reaction process has been shown in Figure 5.2.1.4 a, the complexation of 4-nitophenol with α-CDs that are attached on the Au particle surface favors the adsorption of 4-nitrophenol to the surface of Au nanoparticles. This will increase the local concentration of 4-nitrophenol on the gold nanoparticles surface, which leads to the increase of the rate constant. This effect will be more obvious when more CDs are incorporated into the PVCL microgels. That is why PVCL-α-CD(13.08 wt.-%)-Au particles show higher catalytic activity compared to PVCL-α-CD(1.03 wt.-%)-Au particles and both of the hybrid microgels show higher reaction rate than CTAB-Au nanoparticles.

5.2.2 Catalytic activity for the different target compounds with hybrid microgels as the catalyst

As introduced in the theory part, because the molecular structures of the CDs are truncated cone-shaped with a hollow, trapered cavity of 7.9 Å depth. For different kinds of CDs, the top and bottom diameters of the cavity are different, which have been shown in figure 5.2.2.1. Due to the hydrophobic central cavity, CDs can be used as the receptor to bind with various organic molecules to form inclusion complexes.[188] Besides the hydrophobic interaction, steric effects are considered as another possible driving forces of the cyclodextrins inclusion complexation.

In order to further prove that the CD modified microgels contain certain catalytic selectivity for the target compounds, the catalytic reduction of 2,6-dimethyl-4-nitrophenol (DMNip) by sodium borohydride in the presence of PVCL-α-CD(13.08 wt.-%)-Au microgels has been studied. DMNip has the similar structure with Nip but greater steric hindrance, which may weaken the ability of α-CDs to form host-guest complex with DMNip molecules.

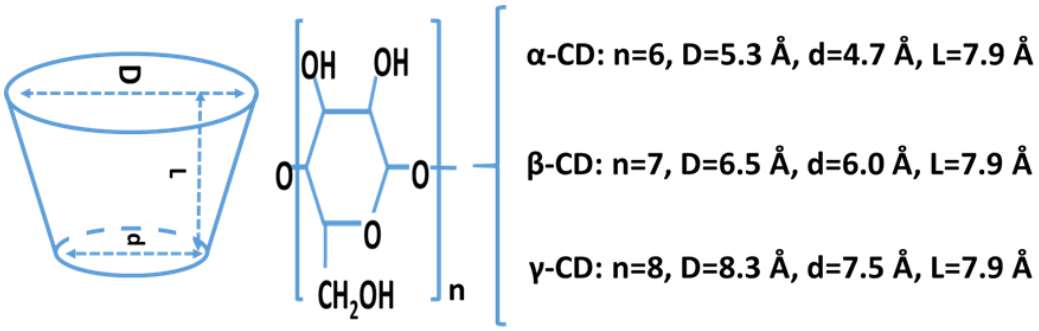

Figure 5.2.2.1 Structure and size of different kinds of cyclodextrin.

As shown in Figure 5.2.2.2 a, there is no obvious shift for the characteristic peak of DMNip when it is mixed with PVCL-α-CD(13.08 wt.-%) microgels with and without loading of Au nanoparticles. This means the complexation between DMNip and hybrid microgels is too weak

to be determined, which is in a good agreement with our speculation above. The reduction of DMNip by $NaBH_4$ using PVCL-α-CD(13.08 wt.-%) microgels as the catalyst has been monitored by UV-vis spectroscopy. The characteristic absorption peak of DMNip at 431 nm weakens with reaction time and the absorption peak of 2,6-dimethyl-4-aminophenol (DMAmp) at 293 nm increases gradually, which indicates the reduction of DMNip to DMAmp as shown in Figure 5.2.2.2 b.

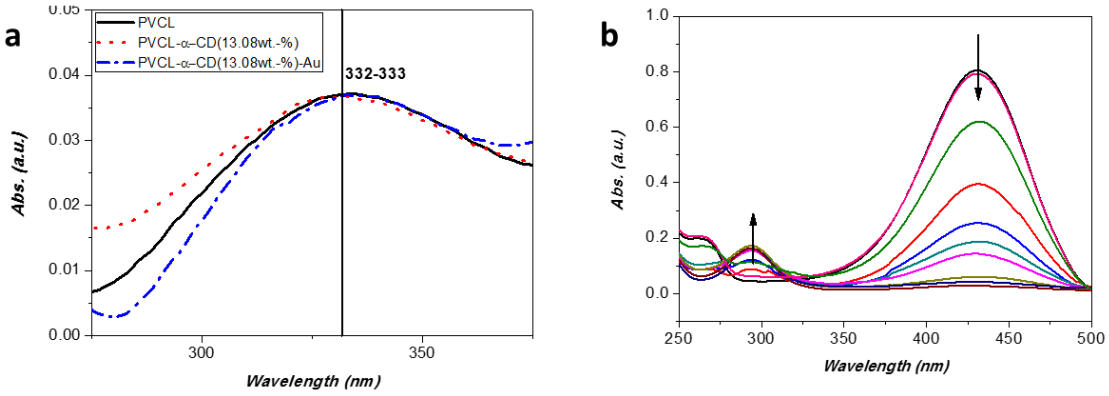

Figure 5.2.2.2 (a) The UV-vis spectra of DMNip: Black, mix with PVCL microgels; Red, mix with PVCL-α-CD(13.08 wt.-%) microgels; Blue, mix with PVCL-α-CD(13.08 wt.-%)-Au microgels. Concentrations: DMNip: 10^{-5}mol/L; microgels: 0.203mg/ml. (b) UV-vis absorption spectra of DMNip reduced by sodium borohydride using PVCL-α-CD(13.08 wt.-%)-Au particles as catalyst.

In order to compare the selectivity of PVCL-α-CD-Au hybrid microgels for Nip and DMNip during the catalytic reaction, the reaction constants k_1 of different catalysts have been shown in Figure 5.2.2.3. A linear relation between k_{app} and the surface S of the Au nanocatalysts can be observed for both reduction of Nip and DMNip. The catalytic reaction rates have been summarized in Table 5.3, which makes it easier to compare the reaction rate from different systems directly. First of all, the Au nanoparticles immobilized in the PVCL-α-CD microgels show much higher catalytic activity than that of other catalyst systems for both catalytic reactions. This demonstrates that PVCL-α-CD microgels can work efficiently as reducing and capping agents for the generation of Au nanoparticles with high catalytic activity. More interestingly, it is clearly to see that the rate constant for the reduction of DMNip (k_1 = 0.018 $Ls^{-1}m^{-2}$) is slower than that of Nip (k_1 = 0.025 $Ls^{-1}m^{-2}$) when PVCL-α-CD(13.08 wt.-%)-Au is used as catalyst. This is opposite to the result of the CTAB-stabilized Au nanoparticles, which do not have complexation with Nip as shown in Figure 5.2.1.3 in the last section. With CTAB-Au nanoparticles as the catalyst, the catalytic reduction of Nip (k_1 = 0.008 $Ls^{-1}m^{-2}$) is slower than that of DMNip (k_1= 0.014 $Ls^{-1}m^{-2}$). Similar result has also been reported by K. S. Suslick

that the reaction rate of Nip is slower than that of DMNip when using Au nanoparticles encapsulated in porous carbon as catalyst.[189]

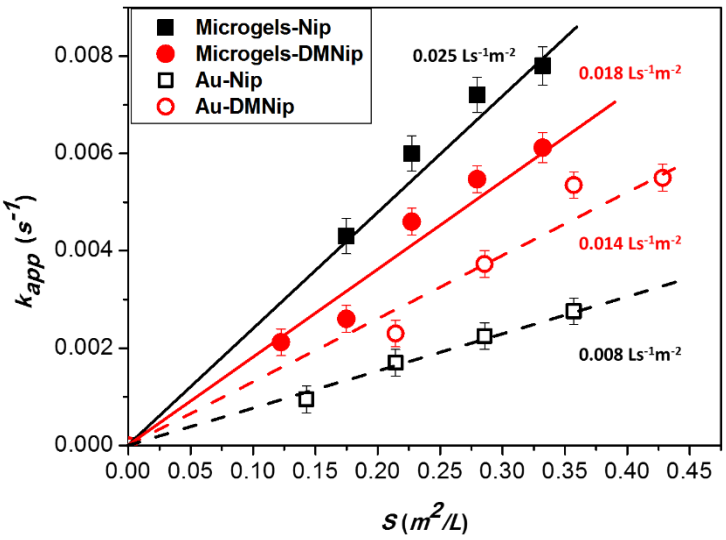

Figure 5.2.2.3 Rate constant k_{app} of the PVCL-α-CD(13.08 wt.-%)-Au and pure Au nanoparticles for the catalytic reduction of 4-nitrophenol (Nip) and 2,6-dimethyl-4-nitrophenol(DMNip) by sodium borohydride as a function of surface area S of Au nanoparticles normalized to the unit volume of the system.

The enhancement in the catalytic reduction of Nip and DMNip in the presence of PVCL-α-CD(13.08 wt.-%)-Au nanoparticles compared to other catalyst systems is due to the following reasons. Firstly, the hybrid microgel contains a good colloidal stability (see figure 5.1.6), which is usually not available in the other systems. Sencondly, without using any surfactant during the synthesis process of Au nanoparticles, the surface activity of Au nanoparticles will not be influenced by the covering of the surfactant. At last, because of the complexation of Nip with α-CDs, the local concentration of Nip on the Au nanoparticle surface increased. However, for the DMNip, this complex interaction is much weaker due to higher steric hindrance. As shown in Figure 5.2.2.2a, the complexation between PVCL-α-CD and DMNip is too weak to be seen from the UV-vis spectra, which may lead to a lower concentration of DMNip around the surface of Au nanoparticles than Nip. That's why the reaction rate of DMNip is slower compared to that of Nip, which is opposite to the results of the other systems. This indicates that dependent on the complexability of the compounds with the α-CDs, the incorporation of α-CDs into the microgels will provide Au nanoparticles with different binding abilities to certain compounds leading to selective enhanced catalytic activity.

Table 5.3 Rate constant k_1 of different catalysts for the reduction of 4-nitrophenol (Nip) and 2,6-dimethyl-4-nitrophenol (DMNip).

Sample	Reduction of Nip k_1 ($Ls^{-1}m^{-2}$)	Reduction of DMNip k_1 ($Ls^{-1}m^{-2}$)	d_{Au} (nm) (from TEM)
PVCL-α-CD(13.08 wt.-%)-Au	0.025	0.018	5.9±0.3
CTAB-stabilized Au	0.008	0.014	10.9±0.4
USP* Au/C[189]	$2.76*10^{-4}$	$3.31*10^{-4}$	31

*USP: Ultrasonis Spray Pyrolysis

In conclusion, we reported the first time that Au nanoparticles can be fabricated in-situ within the PVCL-α-CD hybrid microgels without adding any reducing agents and surfactants. Moreover, the size and loading amount of the Au nanoparticles can be controlled by changing the $HAuCl_4$ amount in the reaction. The presence of α-CD which acts as the surfactant in the microgels allows the homogeneous distribution of Au nanoparticles in the colloidal polymer networks. In addition, the immobilization of Au nanoparticles does not influence the thermosensitive properties of the PVCL-α-CD microgels. The hybrid particles still preserve good colloidal stability after loading of the Au nanoaprticles. The PVCL-α-CD-Au composite particles can work efficiently as catalyst for the reduction of aromatic nitro-compounds. Most importantly, due to the complexation between α-CDs and specific compounds, the synthesized hybrid microgels show different catalytic activity for the target compounds in the catalytic reactions. A significant enhancement in the catalytic activity has been observed for the reduction of Nip, which is different from the reduction of DMNip. Considering the selective binding/complexation properties of CDs with a variety of different guest molecules together with the reducing and stabilizing properties of the PVCL-α-CD microgels, the novel hybrid microgels developed in this thesis could create new opportunities for functional nanomaterials with possible applications in catalysis.

6. Summary

This work is divided into two main parts: first, Cu_2O@PNIPAM core-shell nanoparticles have been synthesized by a novel method. The corresponding photocatalitic activity and fluid properties for the fabrication of gas sensor devices have been studied. In the second part, Au nanoparticles have been synthesized in-situ within the α-CD modified PVCL microgels, which show different catalytic activity for the target compounds during the catalytic reactions.

Cu_2O@PNIPAM core-shell nanoparticle has been synthesized consisting of Cu_2O nanocubes as the core and thermosensitive PNIPAM as the shell. Various factors affecting the coating of the PNIPAM shell have been studied and the thickness of the PNIPAM shell can be controlled by using different amounts of monomer and cross-linker. The colloidal stability of the Cu_2O nanocubes has been significantly enhanced after the modification of PNIPAM shell. In addition, with the protection of PNIPAM shell, the Cu_2O nanocubes can be kept in water for months without oxidation. Compared to the bare Cu_2O nanocubes, the core-shell nanoreactors show much higher catalytic activity for the photo decomposition of methyl orange under visible light, which is 450 times of that of pure Cu_2O nanocubes at 15°C. Moreover, the photocatalytic activity of the Cu_2O@PNIPAM core-shell microgels can be tuned by the thermosensitive PNIPAM shells as expected from theory.

The significant inprovement on fluid properties of Cu_2O nanocubes after modification of PNIPAM shells makes it possible to use the aqueous solution of Cu_2O@PNIPAM core-shell nanoparticles as novel ink materials with low solid content (1.5wt. %) for the high resolution inkjet printing. No additional surfactants and organic solvents is required. Moreover, after burning off the PNIPAM shell, the CuO gas sensor devices made of core-shell nanoparticles contain larger surface area than that from the bare ones, which leads to higher gas sensitivity. The present work proves that modification of Cu_2O nanocubes with PNIPAM shell will have a great potential for the applications of Cu_2O nanoparticles, which is essential to understand the effect of PNIPAM shell on the properties of metal or metal oxide nanomaterials.

The second part of this thesis is the in-situ synthesis of Au nanoparticles in the presence of PVCL-CD microgels without adding any reducing agents and surfactants. The size and loading degree of the Au nanoparticles within the microgels can be controlled by changing the amount of $HAuCl_4$. Au nanoparticles are homogeneously distributed in the colloidal polymer due to the presence of α-CD in the microgels. The immobilization of Au nanoparticles does not influence the swelling-deswelling properties of the PVCL-α-CD microgels. Moreover, the

hybrid particles still preserve good colloidal stability after deposition of Au-nanoparticles. Most importantly, a significant enhancement in the catalytic activity has been observed for the reduction of Nip, while no obvious effect has been found for the reduction of DMNip due to the different complexes ability of α-CDs with specific compounds. Thus, the novel hybrid microgels developed in the present study could create new opportunities for functional nanomaterials with possible applications in selective catalysis.

7. Experimental

7.1 Materials

Copper chloride ($CuCl_2$), sodium dodecyl sulfate (SDS), sodium hydroxide (NaOH), sodium ascorbate, poly(diallyldimethylammonium chloride) (20 wt.% in H_2O) (PDDA), 4-styrenesulfonic acid sodium salt hydrate (NaSS), methyl orange (MO), 5,5-dimethyl-pyrrdine N-oxide (DMPO), N-isopropylacrylamide (NIPAM), N,N'-methylene-bis-acrylamide (BIS), Gold(III) chloride trihydrate ($HAuCl_4 \cdot 3H_2O$), sodium borohydride ($NaBH_4$), solid cetyltrimethylammonium bromide (CTAB), ascorbic acid (AA), acetoacetoxyethyl methacrylate (AAEM), N-vinylcaprolactam (VCL), 2,2'-Azobis(2-methylpropionamidin) dihydrochloride (AMPA), trisodium citrate, 2,6-dimethyl-4-nitrophenol (DMNip) and 4-nitrophenol (Nip) were supplied by Aldrich. 2,2'-azobis(2-methylpropionamidine dihydrochloride) (V50) was supplied by Fluka.VCL was purified by distillation in vacuo. All of the reactants were used without further purification. Water was purified by a Milli-Q system.

7.2 Synthesis procedures

7.2.1 Synthesis of the Cu_2O nanoparticles

7.2.1.1 Synthesis of Cu_2O nanocubes

Cu_2O nanocubes with size of 259±19 nm were synthesized by seed-mediated reaction modified with the method reported by Michael H. Huang's group.[28166] The process was shown in Figure 7.2.1.1. Briefly, at first, a volume of 10 mL aqueous solution containing 10^{-3} M $CuCl_2$ and $3.3*10^{-2}$ M sodium dodecyl sulfate (SDS) was prepared. Then 250 μL of 0.2 M sodium ascorbate and 500 μL of 1 M NaOH solution was added sequentially with shaking for 5 s to prepare the seeds solution. 1 mL of this seeds solution was transferred to 9 mL solution containing 10^{-3} M $CuCl_2$ and $3.3*10^{-2}$ M SDS with shaking for 10 s as the seeds solution for the next step. The same process was repeated for three times. In the last step, the volume of the reaction solution was scaled up to 81 mL. 9 mL seeds solution from the previous step was transferred into it. After shaking for 15 s, 2.25 mL of 0.2 M sodium ascorbate and 4.5 mL of 1M NaOH was added separately with shaking for 8 s. After standing at room temperature in a dark place for 2 h, the color of the solution became orange due to the formation of Cu_2O nanocubes. Then, the Cu_2O nanocubes were washed by centrifugation with the speed at 3500 rpm in water for 20 min and dispersed into 10 mL H_2O.

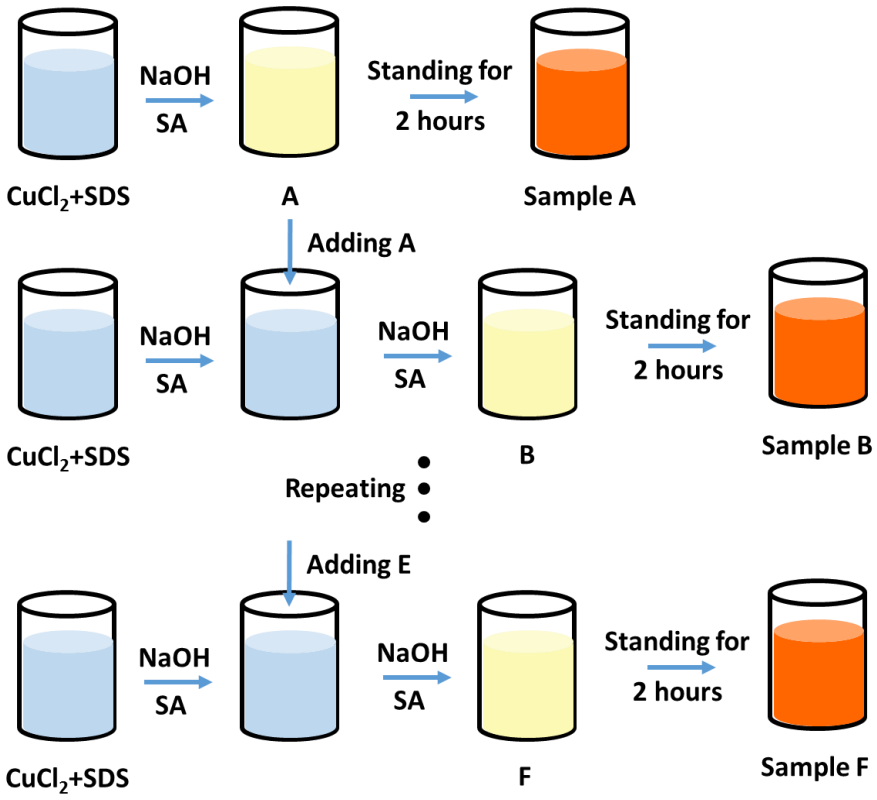

Figure 7.2.1.1 Schematic illustration of the procedure used to grow Cu_2O nanocubes of different sizes.

7.2.1.2 Synthesis of Cu_2O nanospheres

Cu_2O nanospheres with radii ranging from 123 nm to 163 nm were prepared according to a typical procedure[171] with different amount of surfactants. In a typical synthesis procedure, 30 ml 0.02M $Cu(NO_3)_2 \cdot 3H_2O$ was prepared and kept stirring for about 30 min at 250 rpm. Meanwhile 0.5 g Polyvinylpyrrolidone (PVP, average MW=55000) were dissolved in the 20 ml water. After complete dissolution the PVP solution was added dropwise to the $Cu(NO_3)$ solution and the reaction mixture was then stirred for another 2 hours. Then 45.2 μL of hydrazine solution (35% N_2H_4 in water) was added to the reaction mixture drop-wisely. The color of the solution changed into orange immediately after the introduction of N_2H_4, which indicates the production of Cu_2O nanoparticles. The resulting solution was kept stirring for 20 min at room temperature and was then washed with H_2O and EtOH several times by centrifugation and redispersion

7.2.1.3 Synthesis of $Cu_2O@SiO_2$ core-shell nanoparticles

Firstly, Cu_2O nanocubes were modified with a thin layer of SiO_2 as the follows. An amount of 1.4 mg Cu_2O nanocubes were dispersed into 30 ml H_2O and then 0.16 ml (3-Aminopropy)triethoxysilane (APTES) solution (0.001M) was added under the nitrogen condition. After stirring at 600 rpm for 15 min, 0.81 ml Na_2SiO_3 solution (0.088M, pH=10.8)

was added drop by drop and the mixture was vigorously stirred for another 24 hours, followed by centrifugation and dispersing into 10 ml H_2O.

In the second step, the thick silica shell was modified under stöber conditions. Typically, another 90 ml ethanol was added into 10 ml of the above Cu_2O@thin-SiO_2 water solution. 0.05 ml~5 ml NH_3H_2O (30%) solution was used to adjust pH of the mixture. Then, 30 µl TEOS was dissolved in 5 ml of ethanol and added slowly to the solution. After stirring for 24 hours, the samples were centrifuged and dispersed in ethanol for five times.

7.2.1.4 Synthesis of Cu_2O@PNIPAM core-shell nanoparticles

In the first step, Cu_2O nanocubes were modified with PDDA and NaSS as the follows. 2.6 g PDDA was diluted with 27.5 mL H_2O and then 10 mL NaSS (0.024 M) solution was added with the rate of 20 mL/h. After stirring for another 2 hours at a speed of 500 rpm, 10 mL Cu_2O （3.63×10^{-3} M）nanocubes solution was added into the mixed solution slowly. The excess PDDA and NaSS were removed by centrifugation (3500 rpm, 15 min) and the modified Cu_2O nanocubes were dispersed into 5 mL H_2O. The Cu_2O@PNIPAM core-shell nanoparticle was prepared by precipitation polymerization. Under continuous vigorous stirring and nitrogen atmosphere, 5 ml solution containing the modified Cu_2O nanocubes was heated to 75 °C. Thereafter, 1 mL V50 (0.018M) solution was added drop by drop as the initiator. The polymerization was started immediately with the addition of 29 mg NIPAM and 5.1 mg BIS (dissolved in 1 mL H_2O). The orange solution became turbid after 10 min and the reaction was run for 2 h. The composite particles were then purified by centrifugation and redispersion in water several times.

7.2.2 Synthesis of PVCL-α-CD-Au microgel particles

7.2.2.1 Synthesis of PVCL-α-CD microgel

The synthesis of the aqueous microgel dispersion was done using precipitation polymerization according to the literature.[187] Acrylate modified α-cyclodextrin with an average substitution degree of three was prepared according to the literature[37,38] and used for the synthesis of CD-modified microgels. The monomers, 2.06 g (14.72 mmol) VCL, 0.05 g AAEM (0.23 mmol), 0.02 g BIS (0.13 mmol) and 0.05 g (0.04mmol) or 0.30 g (0.26mmol) α-CD acrylate, respectively, were dissolved in 147 mL of water and added to a double-wall glass reactor with KPG-stirrer. The reaction mixture was purged with nitrogen at 70 °C under stirring (200 rpm). Afterwards, 0.02 g (0.07 mmol) AMPA in 3 mL degased water was added. After some minutes, a turbid dispersion was formed and the reaction was carried out for 8 h. Obtained microgels

were purified by dialysis using cellulose membranes with a MWCO of 12,000 – 14,000 Da. The dialysis was carried out for three days. To determine the actual α-CD content, a freeze-dried sample was analyzed by FTIR-spectroscopy.

7.2.2.2 Synthesis of PVCL-α-CD-Au microgel particles

The procedure for the synthesis of the PVCL-α-CD-Au microgel particles is introduced as the follows. In the first step, an aqueous $HAuCl_4$ solution (0.2 mL, 0.01 M) was added to 4.8 mL PVCL-α-CD solution (2.12 mg/mL) under vigorous stirring for 30 min. After that, 0.02 mL NaOH solution (1.0M) was added to the above mixture for the reduction of $HAuCl_4$ in the presence of PVCL-α-CD microgels. The color of the solution changed slowly from light yellow to wine-red. The reaction lasted for 72 hours under magnetic stirring at room temperature. After the reaction, the products were cleaned by dialysis.

7.2.2.3 Synthesis of CTAB-Au nanoparticles

Au nanoparticles with radius around 5nm were prepared according to the seeds growing method.[190] The seeds solution was prepared by adding 0.6 mL of ice-cold, freshly prepared 0.1 M $NaBH_4$ solution into a 20 mL aqueous solution containing $2.5*10^{-4}$ M $HAuCl_4$ and $2.5*10^{-4}$ M trisodium citrate solution and stirring for 4 hours at room temperature. Then 7.5 mL of growth solution (containing $2.5*10^{-4}$M $HAuCl_4$ and 0.08M solid cetyltrimethylammonium bromide) was mixed with 0.05 mL of freshly prepared 0.1 M ascorbic acid solution. Afterwards, 2.5 mL of seed solution was added while stirring. The stirring continued for 10 min after the solution turned into wine red. The Au nanoparticles were washed by centrifugation twice before the catalytic reaction.

7.2.3 Catalytic reactions

7.2.3.1 Photocatalytic measurements

For testing the photocatalytic activity, 10 mL Cu_2O@PNIPAM nanoparticles (0.10 wt. %) were dispersed into 90 mL of an aqueous solution containing 15.6 mg/L methyl orange. The samples were first stirred in the dark for 30 min in order to reach the equilibrium of the adsorption of MO into the Cu_2O@PNIPAM core-shell nanoparticles. A 500 W Xenon lamp was used as the light source, which was placed 20 cm away from the samples. UV-vis absorption spectra of the samples were taken every 30 min by removing the cap to withdraw the solution. The temperature of the reaction was controlled by a water bath with an accuracy of ± 0.2°C. The reaction rate k can be defined through normalization of k_{app} to the total surface of the Cu_2O nanocubes in the system. TGA and TEM results have been used to obtain the amount and size

of Cu_2O nanocubes in the core-shell nanoparticles. For the calculation of the surface area (*S*) of the Cu_2O nanocubes in the core-shell nanoparticles, the density of Cu_2O (6.00 g cm^{-3}) was used.

7.2.3.2 Catalytic reduction of 4-nitropenol and 2,6-dimethyl-4-nitrophenol

The catalytic activity was investigated as follows. Sodium borohydride solution (0.5ml, 0.1M) was added to a Nip solution (4.5ml, 0.11mM) contained in a glass vessel. The solution was purged with N_2 to get rid of oxygen from the solution. Then a given amount of PVCL-α-CD-Au particles was added. Immediately after adding the composite particles, UV-vis spectra of the reaction were taken every 20s in the range of 250-550nm. The catalytic process for DMNip is conducted the same as that of 4-nitropenol as mentioned above.

7.2.4 Inkjet printing

For inkjet deposition a Dimatix DMP-2831 printer system is used. Prior to the printing procedure the Cu_2O and Cu_2O@PNIPAM particle solutions are shortly redispresed using ultra sonic treatment for 30 s. 1 ml of the dispersion is transferred into the printer cartridge via a syringe and deposited onto MEMS sensing chips with a nozzle voltage of 37 ±2V, a droplet firing frequency of 2 kHz, a droplet pitch of 20 µm and a total area of 120 µm * 60 µm. Samples with varying amounts of superposed Cu_2O and Cu_2O@PNIPAM layers have been prepared, starting with a minimum of four stacked prints.

7.3 Characterization

7.3.1 SEM

SEM measurements were operated with SEM LEO GEMINI 1530 in secondary electron mode at 2kV. The samples for the SEM analysis were prepared by dropping 100µL sample solution with solid content of 0.026 wt.% on the silicon wafer and drying at room temperature.

7.3.2 TEM and Cryo-TEM

The sample solutions for the TEM measurement were diluted to 0.1 to 0.2 wt.% and dropped on copper grids. The TEM images were done with JEOL JEM-2100 at 200kV. Cryo-TEM specimens were vitrified by plunging the samples into liquid ethane using an automated plunge freezer (Vitrobot Mark IV, FEI). The lacey carbon copper grids (200 mesh, Science Services) have been pretreated by 10 seconds of glow discharge and equilibrated for 5 minutes at 15 °C or 50 °C inside the plunge freezer. Approximately 5 µl of a pre-temperatured 0.025 wt. % solution was given on the TEM grid and equilibrated at the adjusted temperature for 2 minutes in a water-saturated atmosphere. After blotting the liquid the specimen were vitrified, inserted into a pre-cooled Gatan 914 sample holder and transferred into a JEOL JEM-2100, operating at 200kV.

7.3.3 XRD

XRD measurements were performed in a Bruker D8 diffractometer in the locked coupled mode (2θ ranging from 10° to 80°) with Cu $K\alpha_1$ radiation, the incident wavelength is 1.5406 Å. For the accomplished measurements the acceleration voltage is set to 40 kV and the filament current to 40 mA.

7.3.4 UV-vis spectroscopy

The UV-vis spectra were measured by a Lambda 650 spectrometer supplied by Perkin-Elmer, of which the visible spectra is generated by a tungsten-halogen-lamp and the UV-range is from a deuterium lamp. The temperature of sample environment is controlled by a thermostat (Julabo F30-C) with an accuracy of ±0.1 ºC. Before the measurement, the absorption of distilled water was substracted and the sample solution was placed in a quartz glass cuvette. The extinction was recorded by PerkinElmer WinLab.

7.3.5 Thermogravimetric Analysis (TGA)

TGA using a Netsch STA 409PC LUXX. Fifteen milligrams of dried samples were filled in the crucible and heated to 800 °C under a constant argon flow (30 mL/min) with the heating rate of 10 K•min^{-1}. Then the samples were hold at this temperature for one hour. The weight loss was attributed to the polymer and the remaining weight to the metal content of the sample.

7.3.6 FT-IR

FTIR were carried out at a FT-IR Nexus (Thermo Nicolet). For quantitative measurements about 1 mg of sample was weighed, mixed with KBr and pressed to a pellet. The C-O-C-absorption at 1034 cm^{-1} band was used for integration and to calculate the CD amount according to a calibration line.

7.3.7 Near edge X-ray absorption fine structure – transmission X-ray microscopy (NEXAFS-TXM)

Sample preparation for NEXAFS-TXM: The carbon coated copper grids have been pretreated by 10 s of glow discharge. Approximately 5 µl of a 0.1 wt% dispersion of the particles was deposited on a TEM copper grid with a carbon support film (200 meshes, Science Services, Munich, Germany). The grids were dried at room temperature. The NEXAFS-TXM spectra were recorded on the O-*K*-edge and the Cu-$L_{2,3}$-edge with the HZB-TXM which is installed at the undulator beamline U41-FSGM at the electron storage ring BESSY II, Berlin, Germany. It provides a high spatial resolution close to 10 nm (half-pitch) and a spectral resolution up to $E/\Delta E \approx 10^4$. Typical spectra are presented for each set of measurements. The TXM allows measurements to be taken at room or liquid nitrogen temperature in a vacuum of 1.3×10^{-9} bar. The spectra were recorded at room temperature in transmission mode by taking a sequence of images over a range of photon energies covering the investigated absorption edges with a calculated $E/\Delta E > 5800$ for the Cu-$L_{2,3}$-edge and $E/\Delta E > 12000$ for the O-*K*-edge. Note that the exit slit of the monochromator was set to 9 µm for the Cu-L2,3-edge and 7 µm for the O-*K*-edge resulting in the given calculated monochromaticy values. The exposure time for one image with 1340×1300 pixels was 40 s for the Cu-$L_{2,3}$-edge and 4 s for the O-*K*-edge to achieve a sufficient signal to noise ratio in the images. Taking an image stack with up to 226 images at different energies needs inherently about 45 to 120 min because of all necessary movements, exposure time, and camera read out time and image storage. The NEXAFS spectra were normalized since the photon flux varies as a function of photon energy (hν) and time in the object field (x, y). The normalization was performed by dividing the intensity I(x, y, hν) recorded on a single nanostructure by the intensity I_0 (x+Δx, y+Δy, hν) recorded in its sample

free proximity at position (x+Δx, y+Δy). Both I(x, y, hν) and I_0(x, y, hν) were recorded within the same image stack since bare regions in the vicinity of the nanostructures permit the measurement of I_0.

7.3.8 Electron spin resonance (ESR)

Continuous wave ESR (cwESR) spectra were obtained on a Bruker ESP 300 spectrometer with a Bruker ER-4122 super high quality factor (SHQ) resonator at room temperature. During the ESR measurements samples immersed in the ESR resonator were illuminated through a 250 W cold halogen lamp (Schott KL 2500 LCD). For spin trapping 5,5-dimethyl-pyrroline N-oxide (DMPO) was used. A 50 μL aqueous solution of 50 mg/mL DMPO was mixed with 50 μL of Cu_2O nanoparticle solution with a concentration of 0.20 mg/mL for the Cu_2O@PNIPAM core-shell microgels and 0.15 mg/mL for the pure Cu_2O nanocubes, respectively, in order to ensure an equal amount of Cu_2O in both samples. 20 μL of the mixed sample solution was filled into a Q-band ESR sample tube (inner diameter 1 mm). The resonator was critically coupled yielding quality factors of 4000-5000. Magnetic field modulation for phase-sensitive detection by means of a lock-in amplifier was employed at a frequency of 100 kHz and a peak-to-peak amplitude of 1 G. An incident microwave power of 2 mW was used for all measurements. Spectra were normalized by resonator quality and sample volume.

7.3.9 Determination of the surface area (S) of the Au or Cu_2O nanoparticles

For the calculation of the surface area (S) of the metal nanoparticles, the density of Au (19.3g/cm^3) and Cu_2O (6 g/cm^3) was used. TGA and TEM results have been used to obtain the amount and size of Au and Cu_2O particles (assuming spherical shape of the Au nanoparticles). The size distribution of Au and Cu_2O nanoparticles was measured using Image J software based on their TEM images. At least 100 units were counted.

7.3.10 Dynamic light scattering

The hydrodynamic radius of the samples as a function of temperature was conducted by Zetasizer (Malvern Zetasizer Nano ZS ZEN 3500). The detector was fixed at a scattering angle 173° and the wavelength of the laser is 532 nm. 1 ml 0.01-0.001 wt.% sample solution was measured by using a disposable PS cuvette. Each measurement has been repeated three times and the dispersion has been left for 30 min prior measurement to attain thermal equilibrium.

7.3.11 Zeta-potential measurement

Zeta-potential measurement has been conducted with a Malvern Zetasizer Nano ZS. The cuvette (Malvern disposable folded capillary cell, DTS1070) was filled with 1 ml of an

approximately 0.01 wt. % dispersion in water. The scattering angle was fixed at 17° and the wavelength of the laser was 532 nm. Each measurement was repeated three times and the samples were left for 30 min before measurement to attain thermal equilibrium.

7.3.12 Fluid properties characterization

Surface-tension

Surface-tension was measured at room temperature by Contact Angle System OCA20 from dataphysics using pedant drop configuration.

Rheological measurements

Rheological measurements have been performed with a stress-controlled rheometer (Physica MCR 301, Anton Paar) equipped with cone−plate geometry (CP50). Shear steady tests were done with shear rate increased process from 10^{-3} to 10^{3} s^{-1} and the decreased process from 10^{3} to 10^{-3} s^{-1}.

Colloidal stability measurements

Colloidal stability was analyzed using a LUMiSizer® from L.U.M. GmbH. The samples were measured at 4000 rpm over 300 cycles each 30 seconds to determine the sedimentation velocity.

Bibliography

(1) Sanchez C.; Julian, B.; Belleville, P.; Popall, M. Applications of hybrid organic-inorganic nanocomposites. *J. Mater. Chem.* **2005**, *15*, 3559-3592.

(2) Karg, M.; Hellweg, T. Smart Inorganic/organic Hybrid Microgels: Synthesis and Characterisation. *J. Mater. Chem.* **2009**, *19*, 8714.

(3) Bonaccorso, F.; Colombo, L.; Yu, G.; Stoller, M.; Tozzini, V.; Ferrari, a C.; Ruoff, R. S.; Pellegrini, V. 2D Materials. Graphene, Related Two-Dimensional Crystals, and Hybrid Systems for Energy Conversion and Storage. *Science.* **2015**, *347*, 1246501.

(4) Yin, P. T.; Shah, S.; Chhowalla, M.; Lee, K. B. Design, Synthesis, and Characterization of Graphene-Nanoparticle Hybrid Materials for Bioapplications. *Chem. Rev.* **2015**, *115*, 2483–2531.

(5) Jia, H.; Roa, R.; Angioletti-Uberti, S.; Henzler, K.; Ott, A.; Lin, X.; Möser, J.; Kochovski, Z.; Schnegg, A.; Dzubiella, J.; *et al.* Thermosensitive Cu2O-PNIPAM Core-Shell Nanoreactors with Tunable Photocatalytic Activity. *J. Mater. Chem. A* **2016**, *4*, 9677-9684.

(6) Jia, H.; Schmitz, D.; Ott, A.; Pich, A.; Lu, Y. Cyclodextrin Modified Microgels as "nanoreactor" for the Generation of Au Nanoparticles with Enhanced Catalytic Activity. *J. Mater. Chem. A* **2015**, *3*, 6187–6195.

(7) Gensel, J.; Dewald, I.; Erath, J.; Betthausen, E.; Müller, A. H. E.; Fery, A. Reversible Swelling Transitions in Stimuli-Responsive Layer-by-Layer Films Containing Block Copolymer Micelles. *Chem. Sci.* **2013**, 325–334.

(8) Stuart, M. a C.; Huck, W. T. S.; Genzer, J.; Müller, M.; Ober, C.; Stamm, M.; Sukhorukov, G. B.; Szleifer, I.; Tsukruk, V. V; Urban, M.; *et al.* Emerging Applications of Stimuli-Responsive Polymer Materials. *Nat. Mater.* **2010**, *9*, 101–113.

(9) Zhang, J.; Zhang, M.; Tang, K.; Verpoort, F.; Sun, T. Polymer-Based Stimuli-Responsive Recyclable Catalytic Systems for Organic Synthesis. *Small* **2014**, *10*, 32–46.

(10) Tripathi, B. P.; Dubey, N. C.; Simon, F.; Stamm, M. Thermo Responsive Ultrafiltration Membranes of Grafted poly(N-Isopropyl Acrylamide) via Polydopamine. *RSC Adv.* **2014**, *4*, 34073–34083.

(11) Angioletti-Uberti, S.; Lu, Y.; Ballauff, M.; Dzubiella, J. Theory of Solvation-Controlled Reactions in Stimuli-Responsive Nanoreactors. *J. Phys. Chem. C* **2015**, *119*, 15723-15730.

(12) Wu, S.; Dzubiella, J.; Kaiser, J.; Drechsler, M.; Guo, X.; Ballauff, M.; Lu, Y. Thermosensitive Au-PNIPA Yolk-Shell Nanoparticles with Tunable Selectivity for Catalysis. *Angew. Chemie - Int. Ed.* **2012**, *5*, 2229–2233.

(13) Lu, Y.; Mei, Y.; Drechsler, M.; Ballauff, M. Thermosensitive Core-Shell Particles as Carriers for Ag Nanoparticles: Modulating the Catalytic Activity by a Phase Transition in Networks. *Angew. Chemie - Int. Ed.* **2006**, *45*, 813–816.

(14) Contreras-Cáceres, R.; Abalde-Cela, S.; Guardia-Girós, P.; Fernández-Barbero, A.; Pérez-Juste, J.; Alvarez-Puebla, R. A.; Liz-Marzán, L. M. Multifunctional Microgel Magnetic/optical Traps for SERS Ultradetection. *Langmuir* **2011**, *27*, 4520–4525.

(15) Das, M.; Mordoukhovski, L.; Kumacheva, E. Sequestering Gold Nanorods by Polymer Microgels. *Adv. Mater.* **2008**, *20*, 2371–2375.

(16) Suzuki, D.; Nagase, Y.; Kureha, T.; Sato, T. Internal Structures of Thermosensitive Hybrid Microgels Investigated by Means of Small-Angle X-Ray Scattering. *J. Phys. Chem. B* **2014**, *118*, 2194–2204.

(17) Pich, A.; Hain, J.; Lu, Y.; Boyko, V.; Prots, Y.; Adler, H. J. Hybrid Microgels with ZnS Inclusions. *Macromolecules* **2005**, *38*, 6610–6619.

(18) Janine Dubbert, Katja Nothdurft, Matthias Karg, W. R. Core-Shell-Shell and Hollow Double-Shell Microgels with Advanced Temperature Responsiveness. *Macromol. Rapid Commun.* **2015**, 159–164.

(19) Kuang, M.; Wang, D.; Moehwald, H. Fabrication of Thermoresponsive Plasmonic Microspheres with Long-Term Stability from Hydrogel Spheres. *Adv. Funct. Mater.* **2005**, *15*, 1611–1616.

(20) Pérez-Juste, J.; Pastoriza-Santos, I.; Liz-Marzán, L. M. Multifunctionality in Metal@microgel Colloidal Nanocomposites. *J. Mater. Chem. A* **2013**, 1, 20–26.

(21) Wiese, S.; Spiess, A. C.; Richtering, W. Microgel-Stabilized Smart Emulsions for Biocatalysis. *Angew. Chemie - Int. Ed.* **2013**, *52*, 576–579.

(22) Lu, Y.; Yuan, J.; Polzer, F.; Drechsler, M.; Preussner, J. In Situ Growth of Catalytic Active Au− Pt Bimetallic Nanorods in Thermoresponsive Core− Shell Microgels. *ACS Nano* **2010**, *4*, 7078-7086.

(23) Zhu, Y.; Fan, L.; Yang, B.; Du, J. Multifunctional Homopolymer Vesicles for Facile Immobilization of Gold Nanoparticles and Effective Water Remediation. *ACS Nano* **2014**, *8*, 5022–5031.

(24) Wang, Z.; Tan, B.; Hussain, I.; Schaeffer, N.; Wyatt, M. F.; Brust, M.; Cooper, A. I. Design of Polymeric Stabilizers for Size-Controlled Synthesis of Monodisperse Gold Nanoparticles in Water. *Langmuir* **2007**, *23*, 885–895.

(25) Palioura, D.; Armes, S. P.; Anastasiadis, S. H.; Vamvakaki, M. Metal Nanocrystals Incorporated within pH-Responsive Microgel Particles. *Langmuir* **2007**, *23*, 5761–5768.

(26) Antonietti, M.; Groehn, F.; Hartmann, J.; Bronstein, L. Nonclassical Shapes of Noble-Metal Colloids by Synthesis in Microgel Nanoreactors. *Angew. Chem.* **1997**, *36*, 2080–2083.

(27) Xu, S.; Zhang, J.; Paquet, C.; Lin, Y.; Kumacheva, E. From Hybrid Microgels to Photonic Crystals. *Adv. Funct. Mater.* **2003**, *13*, 468–472.

(28) Horecha, M.; Kaul, E.; Horechyy, A.; Stamm, M. Polymer Microcapsules Loaded with Ag Nanocatalyst as Active Microreactors. *J. Mater. Chem. A* **2014**, *2*, 7431-7438.

(29) Contreras-Cáceres, R.; Pacifico, J.; Pastoriza-Santos, I.; Pérez-Juste, J.; Fernández-Barbero, A.; Liz-Marzán, L. M. Au@pNIPAM Thermosensitive Nanostructures: Control over Shell Cross-Linking, Overall Dimensions, and Core Growth. *Adv. Funct. Mater.* **2009**, *19*, 3070–3076.

(30) Suzuki, D.; Kawaguchi, H. Hybrid Microgels with Reversibly Changeable Multiple Brilliant Color. *Langmuir* **2006**, *22*, 3818–3822.

(31) Lu, Y.; Proch, S.; Schrinner, M.; Drechsler, M.; Kempe, R.; Ballauff, M. Thermosensitive Core-Shell Microgel as a “nanoreactor” for Catalytic Active Metal Nanoparticles. *J. Mater. Chem.* **2009**, *19*, 3955.

(32) Lu, Y.; Mei, Y.; Ballauff, M.; Drechsler, M. Thermosensitive Core-Shell Particles as Carrier Systems for Metallic Nanoparticles. *J. Phys. Chem. B* **2006**, *110*, 3930–3937.

(33) Busbee, B. D.; Obare, S. O.; Murphy, C. J. An Improved Synthesis of High-Aspect-Ratio Gold Nanorods. *Adv. Mater.* **2003**, *15*, 414–416.

(34) Moessner, S.; Spatz, J. P.; Moeller, M.; Aberle, T.; Schmidt, J.; Burchard, W. Solution Behavior of Poly(styrene)-block-poly(2-vinylpyridine) Micelles Containing Gold Nanoparticles. *Macromolecules* **2000**, *33*, 4791–4798.

(35) Aslam, M.; Fu, L.; Su, M.; Vijayamohanan, K.; Dravid, V. P. Novel One-Step Synthesis of Amine-Stabilized Aqueous Colloidal Gold Nanoparticles. *J. Mater. Chem.* **2004**, *14*, 1795.

(36) Kim, K.; Kim, K. L.; Choi, J. Y.; Lee, H. B.; Shin, K. S. Surface Enrichment of Ag Atoms in Au/Ag Alloy Nanoparticles Revealed by Surface-Enhanced Raman Scattering of 2,6-Dimethylphenyl Isocyanide. *J. Phys. Chem. C* **2010**, *114*, 3448–3453.

(37) Carregal-Romero, S.; Buurma, N. J.; Pérez-Juste, J.; Liz-Marzán, L. M.; Hervés, P. Catalysis by Au@pNIPAM Nanocomposites: Effect of the Cross-Linking Density. *Chem. Mater.* **2010**, *22*, 3051–3059.

(38) Tang, F.; Ma, N.; Tong, L.; He, F.; Li, L. Control of Metal-Enhanced Fluorescence with pH- and Thermoresponsive Hybrid Microgels. *Langmuir* **2012**, *28*, 883–888.

(39) Yu, E.; Galiana, I.; Martinez-Manez, R.; Stroeve, P.; Marcos, M. D.; Aznar, E.; Sancenon, F.; R. Murguia, J.; Amoros, P. Poly(N-Isopropylacrylamide)-Gated Fe3O4/SiO2 Core Shell Nanoparticles with Expanded Mesoporous Structures for the Temperature Triggered Release of Lysozyme. *Colloids Surfaces A Physicochem. Eng. Asp.* **2015**, 135, 652–660.

(40) Barthet, C.; Andrew, J.; Mickey; Dean, B.; Cairns; Steven, P.; Armes. Synthesis of Novel Polymer-Silica Colloidal Nanocomposites via Free-Radical Polymerization of Vinyl Monomers. *Adv. Mater.* **1999**, *11*, 408–410.

(41) Tan, L.; Liu, J.; Zhou, W.; Wei, J.; Peng, Z. A Novel Thermal and pH Responsive Drug Delivery System Based on ZnO@PNIPAM Hybrid Nanoparticles. *Mater. Sci. Eng. C* **2014**, *45*, 524–529.

(42) Cao, Y. X.; Wang, M.; Wang, J. T.; Li, C. H. Thermoresponsive CdS@PNIPAM Core-Shell Nanocomposite. *J. Mater. Sci.* **2011**, *46*, 6461–6464.

(43) Baker, W. O. Microgel, a New Macromolecule. Relation to Sol and Gel as Structural

Elements of Synthetic Rubber. *Rubber Chem. Technol.* **1949**, *41*, 511–520.

(44) Bromberg, L.; Temchenko, M.; Hatton, T. A. Smart Microgel Studies. Polyelectrolyte and Drug-Absorbing Properties of Microgels from Polyether-Modified Poly(acrylic Acid). *Langmuir* **2003**, *19*, 8675–8684.

(45) Neyret, S.; Vincent, B. The Properties of Polyampholyte Microgel Particles Prepared by Microemulsion Polymerization. *Polymer (Guildf).* **1997**, *38*, 6129–6134.

(46) Kaneda, I.; Vincent, B. Swelling Behavior of PMMA-G-PEO Microgel Particles by Organic Solvents. *J. Colloid Interface Sci.* **2004**, *274*, 49–54.

(47) Boyko, V.; Pich, A.; Lu, Y.; Richter, S.; Arndt, K. F.; Adler, H. J. P. Thermo-Sensitive poly(N-Vinylcaprolactam-Co-Acetoacetoxyethyl Methacrylate) Microgels: 1 - Synthesis and Characterization. *Polymer (Guildf).* **2003**, *44*, 7821–7827.

(48) Sawai, T.; Yamazaki, S.; Ishigami, Y.; Ikariyama, Y.; Aizawa, M. Electrical Control of Reversible Microgel Flocculation and Its Estimated Performance as a Display Device. *J. Electroanal. Chem.* **1992**, *322*, 1–7.

(49) Fernández-Nieves, A.; Fernández-Barbero, A.; Nieves, F. J. de las; Vincent, B. Motion of Microgel Particles under an External Electric Field. *J. Phys. Condens. Matter* **2000**, *12*, 3605–3614.

(50) Fernández-Nieves, A.; Márquez, M. Electrophoresis of Ionic Microgel Particles: From Charged Hard Spheres to Polyelectrolyte-like Behavior. *J. Chem. Phys.* **2005**, *122*, 084702.

(51) Nayak, S.; Lee, H.; Chmielewski, J.; Lyon, L. A. Folate-Mediated Cell Targeting and Cytotoxicity Using Thermoresponsive Microgels. *J. Am. Chem. Soc.* **2004**, *126*, 10258–10259.

(52) Nolan, C. M.; Reyes, C. D.; Debord, J. D.; García, A. J.; Lyon, L. A. Phase Transition Behavior, Protein Adsorption, and Cell Adhesion Resistance of Poly(ethylene Glycol) Cross-Linked Microgel Particles. *Biomacromolecules* **2005**, *6*, 2032–2039.

(53) Retama, J. R.; Lopez-Ruiz, B.; Lopez-Cabarcos, E. Microstructural Modifications Induced by the Entrapped Glucose Oxidase in Cross-Linked Polyacrylamide Microgels Used as Glucose Sensors. *Biomaterials* **2003**, *24*, 2965–2973.

(54) Guo, Z.; Sautereau, H.; Kranbuehl, D. E. Structural Evolution and Heterogeneities Studied by Frequency-Dependent Dielectric Sensing in a Styrene/dimethacrylate Network. *Macromolecules* **2005**, *38*, 7992–7999.

(55) Beljonne, D.; Curutchet, C.; Scholes, G. D.; Silbey, R. J. Microgel Collodial Crystals. *J. Phys. Chem. B* **2009**, *113*, 6583–6599.

(56) Jones, C. D.; Lyon, L. A. Photothermal Patterning of Microgel/gold Nanoparticle Composite Colloidal Crystals. *J. Am. Chem. Soc.* **2003**, *125*, 460–465.

(57) Pelton, R. Temperature-Sensitive Aqueous Microgels. *Adv. Colloid Interface Sci.* **2000**, *85*, 1–33.

(58) Lyon, L. A.; Meng, Z.; Singh, N.; Sorrell, C. D.; St. John, A. Thermoresponsive Microgel-Based Materials. *Chem. Soc. Rev.* **2009**, *38*, 865-874.

(59) Ramos, J.; Imaz, A.; Forcada, J. Temperature-Sensitive Nanogels: poly(N-Vinylcaprolactam) versus poly(N-Isopropylacrylamide). *Polym. Chem.* **2012**, *3*, 852-856.

(60) Clarke, K. C.; Lyon, L. A. Modulation of the Deswelling Temperature of Thermoresponsive Microgel Films. *Langmuir* **2013**, *29*, 12852–12857.

(61) Nayak, S.; Gan, D.; Serpe, M. J.; Lyon, L. A. Hollow Thermoresponsive Microgels. *Small* **2005**, *1*, 416–421.

(62) Wang, F.; Du, J. Disclosing the Nature of Thermo-Responsiveness of poly(N-Isopropyl Acrylamide)-Based Polymeric Micelles: Aggregation or Fusion? *Chem. Commun.* **2015**, *51*, 11198–11201.

(63) Lin, M.; Chen, G.; Jiang, M. Direct and Indirect Core–shell Inversion of Block Copolymer Micelles. *Polym. Chem.* **2014**, *5*, 234-240.

(64) Makino, K.; Fujita, Y.; Takao, K. ichi; Kobayashi, S.; Ohshima, H. Preparation and Properties of Thermosensitive Hydrogel Microcapsules. *Colloids Surfaces B Biointerfaces* **2001**, *21*, 259–263.

(65) Pich, A.; Karak, A.; Lu, Y.; Ghosh, A. K.; Adler, H. J. P. Preparation of Hybrid Microgels Functionalized by Silver Nanoparticles. *Macromol. Rapid Commun.* **2006**, *27*, 344–350.

(66) Krauss, I. J.; Mandal, M.; Danishefsky, S. J. Total Synthesis of (+)-Isomigrastatin. *Angew. Chemie - Int. Ed.* **2007**, *46*, 5576–5579.

(67) Conte, M.; Carley, A. F.; Hutchings, G. J. Reactivation of a Carbon-Supported Gold Catalyst for the Hydrochlorination of Acetylene. *Catal. Letters* **2008**, *124*, 165–167.

(68) Schrinner, M.; Proch, S.; Mei, Y.; Kempe, R.; Miyajima, N.; Ballauff, M. Stable Bimetallic Gold-Platinum Nanoparticles Immobilized on Spherical Polyelectrolyte Brushes: Synthesis, Characterization, and Application for the Oxidation of Alcohols. *Adv. Mater.* **2008**, *20*, 1928–1933.

(69) Ballauff, M.; Lu, Y. "Smart" Nanoparticles: Preparation, Characterization and Applications. *Polymer (Guildf).* **2007**, *48*, 1815–1823.

(70) Hellweg, T.; Dewhurst, C. D.; Eimer, W.; Kratz, K. PNIPAM-Co-Polystyrene Core-Shell Microgels: Structure, Swelling Behavior, and Crystallization. *Langmuir* **2004**, *20*, 4330–4335.

(71) Hoppe, C. E.; Lazzari, M.; Pardiñas-Blanco, I.; López-Quintela, M. A. One-Step Synthesis of Gold and Silver Hydrosols Using poly(N-Vinyl-2-Pyrrolidone) as a Reducing Agent. *Langmuir* **2006**, *22*, 7027–7034.

(72) Zhou, M.; Wang, B.; Rozynek, Z.; Xie, Z.; Fossum, J. O.; Yu, X.; Raaen, S. Minute Synthesis of Extremely Stable Gold Nanoparticles. *Nanotechnology* **2009**, *20*, 505606.

(73) Agrawal, G.; Schürings, M. P.; van Rijn, P.; Pich, A. Formation of Catalytically Active Gold–polymer Microgel Hybrids via a Controlled in Situ Reductive Process. *J. Mater. Chem. A* **2013**, *1*, 13244-13251.

(74) Jiang, T.; Xie, T.; Yang, W.; Fan, H.; Wang, D. Photoinduced Charge Transfer Process in P-Cu2O/n-Cu2O Homojunction Film and Its Photoelectric Gas-Sensing Properties. *J. Colloid Interface Sci.* **2013**, *405*, 242–248.

(75) Sui, Y.; Zeng, Y.; Fu, L.; Zheng, W.; Li, D.; Liu, B.; Zou, B. Low-Temperature Synthesis of Porous Hollow Structured Cu2O for Photocatalytic Activity and Gas Sensor Application. *RSC Adv.* **2013**, *3*, 18651-18660.

(76) Dong, C.; Zhong, M.; Huang, T.; Ma, M.; Wortmann, D.; Brajdic, M.; Kelbassa, I. Photodegradation of Methyl Orange under Visible Light by Micro-Nano Hierarchical Cu 2O Structure Fabricated by Hybrid Laser Processing and Chemical Dealloying.

ACS Applied Materials and Interfaces, **2011**, *3*, 4332–4338.

(77) Huang, W. C.; Lyu, L. M.; Yang, Y. C.; Huang, M. H. Synthesis of Cu2O Nanocrystals from Cubic to Rhombic Dodecahedral Structures and Their Comparative Photocatalytic Activity. *J. Am. Chem. Soc.* **2012**, *134*, 1261–1267.

(78) Brittman, S.; Yoo, Y.; Dasgupta, N. P.; Kim, S. I.; Kim, B.; Yang, P. Epitaxially Aligned Cuprous Oxide Nanowires for All-Oxide, Single-Wire Solar Cells. *Nano Lett.* **2014**, *14*, 4665–4670.

(79) Poizot, P.; Laruelle, S.; Grugeon, S.; Dupont, L.; Tarascon, J.-M. Nano-Sized Transition-Metal Oxides as Negative-Electrode Materials for Lithium-Ion Batteries. *Nature* **2000**, *407*.

(80) Deng, S.; Tjoa, V.; Fan, H. M.; Tan, H. R.; Sayle, D. C.; Olivo, M.; Mhaisalkar, S.; Wei, J.; Sow, C. H. Reduced Graphene Oxide Conjugated Cu2O Nanowire Mesocrystals for High-Performance NO2 Gas Sensor. *J. Am. Chem. Soc.* **2012**, *134*, 4905–4917.

(81) Tian, Q.; Wu, W.; Sun, L.; Yang, S.; Lei, M.; Zhou, J.; Liu, Y. Tube-Like Ternary Fe2O3@SnO2@Cu2O Sandwich Heterostructures: Synthesis and Enhanced Photocatalytic Properties. *ACS Appl. Mater. Interfaces* **2014**, *6*, 13088–13097.

(82) Hua, Q.; Cao, T.; Gu, X.; Lu, J.; Jiang, Z.; Pan, X.; Luo, L.; Li, W.; Huang, W. Crystal-Plane-Controlled Selectivity of Cu2O Catalysts in Propylene Oxidation with Molecular Oxygen. *Angew. Chemie - Int. Ed.* **2014**, *126*, 4956–4961.

(83) Pengcheng Dai, Wei Li, Jin Xie, Yumin He, James Thorne, Gregory McMahon, Jinhua Zhan, D. W. Forming Buried Junctions to Enhance the Photovoltage Generated by Cuprous Oxide in Aqueous Solutions. *Angew. Chemie - Int. Ed.* **2014**, *53*, 13493–13497.

(84) Kuo, C. H.; Huang, M. H. Morphologically Controlled Synthesis of Cu2O Nanocrystals and Their Properties. *Nano Today* **2010**, *5*, 106–116.

(85) Ho, J. Y.; Huang, M. H. Synthesis of Submicrometer-Sized Cu2O Crystals with Morphological Evolution from Cubic to Hexapod Structures and Their Comparative Photocatalytic Activity. *J. Phys. Chem. C* **2009**, *113*, 14159–14164.

(86) Paracchino, A.; Laporte, V.; Sivula, K.; Grätzel, M.; Thimsen, E. Highly Active Oxide

Photocathode for Photoelectrochemical Water Reduction. *Nat. Mater.* **2011**, *10*, 456–461.

(87) Morales-Guio, C. G.; Tilley, S. D.; Vrubel, H.; Grätzel, M.; Hu, X. Hydrogen Evolution from a copper(I) Oxide Photocathode Coated with an Amorphous Molybdenum Sulphide Catalyst. *Nat. Commun.* **2014**, *5*, 3059.

(88) Zhang, Z.; Dua, R.; Zhang, L.; Zhu, H.; Zhang, H.; Wang, P. Carbon-Layer-Protected Cuprous Oxide Nanowire Arrays for Efficinet Water Reduction. *ACS Nano* **2013**, *7*, 1709–1717.

(89) Zhang, Z.; Wang, P. Highly Stable Copper Oxide Composite as an Effective Photocathode for Water Splitting via a Facile Electrochemical Synthesis Strategy. *J. Mater. Chem.* **2012**, *22*, 2456.

(90) Yang, H.; Min, Y.; Kim, Y.; Jeong, U. Preparation of Cu2O@SiO2 Particles and Their Evolution to Hollow SiO2 Particles. *Colloids Surfaces A Physicochem. Eng. Asp.* **2013**, *420*, 30–36.

(91) Su, X.; Zhao, J.; Zhao, X.; Guo, Y.; Zhu, Y.; Wang, Z. A Facile Synthesis of Cu(2)O/SiO(2) and Cu/SiO(2) Core-Shell Octahedral Nanocomposites. *Nanotechnology* **2008**, *19*, 365610.

(92) Álvarez-Puebla, R. a.; Contreras-Cáceres, R.; Pastoriza-Santos, I.; Pérez-Juste, J.; Liz-Marzán, L. M. Au@pNIPAM Colloids as Molecular Traps for Surface-Enhanced, Spectroscopic, Ultra-Sensitive Analysis. *Angew. Chemie - Int. Ed.* **2009**, *48*, 138–143.

(93) Angioletti-Uberti, S.; Lu, Y.; Ballauff, M.; Dzubiella, J. Theory of Solvation-Controlled Reactions in Stimuli-Responsive Nanoreactors. *J. Phys. Chem. C* **2015**, *119*, 15723–15730.

(94) Henzler, K.; Heilemann, A.; Kneer, J.; Guttmann, P.; Jia, H.; Bartsch, E.; Lu, Y.; Palzer, S. Investigation of Reactions between Trace Gases and Functional CuO Nanospheres and Octahedrons Using NEXAFS-TXM Imaging. *Sci. Rep.* **2015**, *5*, 17729.

(95) Seerden, K.; Reis, N.; Evans, J.; Grant, P.; Halloran, J.; Derby, B. Ink-Jet Printing of Wax-Based Alumina Suspensions. *J. Am. Ceram. Soc.* **2001**, *84*, 2514–2520.

(96) Wang, T.; Derby, B. Ink-Jet Printing and Sintering of PZT. *J. Am. Ceram. Soc.* **2005**,

88, 2053–2058.

(97) Small, W. R.; In Het Panhuis, M. Inkjet Printing of Transparent, Electrically Conducting Single-Walled Carbon-Nanotube Composites. *Small* **2007**, *3*, 1500–1503.

(98) Marjanovic, N.; Hammerschmidt, J.; Perelaer, J.; Farnsworth, S.; Rawson, I.; Kus, M.; Yenel, E.; Tilki, S.; Schubert, U. S.; Baumann, R. R. Inkjet Printing and Low Temperature Sintering of CuO and CdS as Functional Electronic Layers and Schottky Diodes. *J. Mater. Chem.* **2011**, *21*, 13634-13639.

(99) Kukkola, J.; Jansson, E.; Popov, A.; Lappalainen, J.; Mäklin, J.; Halonen, N.; Tóth, G.; Shchukarev, A.; Mikkola, J. P.; Jantunen, H.; *et al.* Novel Printed Nanostructured Gas Sensors. *Procedia Eng.* **2011**, *25*, 896–899.

(100) Kukkola, J.; Mohl, M.; Leino, A.-R.; Tóth, G.; Wu, M.-C.; Shchukarev, A.; Popov, A.; Mikkola, J.-P.; Lauri, J.; Riihimäki, M.; *et al.* Inkjet-Printed Gas Sensors: Metal Decorated WO3 Nanoparticles and Their Gas Sensing Properties. *J. Mater. Chem.* **2012**, *22*, 17878-17886.

(101) Shen, W.; Zhang, X.; Huang, Q.; Xu, Q.; Song, W. Preparation of Solid Silver Nanoparticles for Inkjet Printed Flexible Electronics with High Conductivity. *Nanoscale* **2014**, *6*, 1622–1628.

(102) Torrisi, F.; Hasan, T.; Wu, W.; Sun, Z.; Lombardo, A.; Kulmala, T. S.; Hsieh, G.-W.; Jung, S.; Bonaccorso, F.; Paul, P. J.; *et al.* Inkjet-Printed Graphene Electronics. *ACS Nano* **2012**, *6*, 2992–3006.

(103) Jang, D.; Kim, D.; Moon, J. Influence of Fluid Physical Properties on Ink-Jet Printability. *Langmuir* **2009**, *25*, 2629–2635.

(104) S. Brett Walker and Jennifer A. Lewis. Supporting Information for Reactive Silver Inks for Patterning High-Conductivity Features at Mild Temperatures. *J. Am. Chem. Soc.* **2012**, *134*, S1–S6.

(105) Huang, Q.; Shen, W.; Song, W. Synthesis of Colourless Silver Precursor Ink for Printing Conductive Patterns on Silicon Nitride Substrates. *Appl. Surf. Sci.* **2012**, *258*, 7384–7388.

(106) van den Berg, A. M. J.; de Laat, A. W. M.; Smith, P. J.; Perelaer, J.; Schubert, U. S. Geometric Control of Inkjet Printed Features Using a Gelating Polymer. *J. Mater.*

Chem. **2007**, *17*, 677-683.

(107) Lu, Y.; Ballauff, M. Thermosensitive Core-Shell Microgels: From Colloidal Model Systems to Nanoreactors. *Prog. Polym. Sci.* **2011**, *36*, 767–792.

(108) Chen, H.; Li, W.; Zhao, H.; Gao, J.; Zhang, Q. Thermo-Induced Formation of Physical "Cross-Linking Points" of PNIPAM-G-PEO in Semidilute Aqueous Solutions. *J. Colloid Interface Sci.* **2006**, *298*, 991–995.

(109) Scherzinger, C.; Holderer, O.; Richter, D.; Richtering, W. Polymer Dynamics in Responsive Microgels: Influence of Cononsolvency and Microgel Architecture. *Phys. Chem. Chem. Phys.* **2012**, *14*, 2762-2768.

(110) Cho, C. S.; Cheon, J. B.; Jeong, Y. I.; Kim, I. S.; Kim, S. H.; Akaike, T. Novel Core-Shell Type Thermo-Sensitive Nanoparticles Composed of Poly (γ-Benzyl L-Glutamate) as the Core and Poly (N-Isopropylacrylamide) as the Shell. *Macromol. Rapid Commun.* **1997**, *18*, 361–369.

(111) Jones, C. D.; Lyon, L. A. Dependence of Shell Thickness on Core Compression in Acrylic Acid Modified Poly(N -Isopropylacrylamide) Core/Shell Microgels. *Langmuir* **2003**, *19*, 4544–4547.

(112) Wu, C.; Wang, X. Globule-to-Coil Transition of a Single Homopolymer Chain in Solution. *Phys. Rev. Lett.* **1998**, *80*, 4092–4094.

(113) Heskins, M.; Guillet, J. E. Solution Properties of Poly(N-Isopropylacrylamide). *J. Macromol. Sci. Part A - Chem.* **1968**, *2*, 1441–1455.

(114) Neely, W. B. Solution Properties of Polysaccharides. IV. Molecular Weight and Aggregate Formation in Methylcellulose Solutions. *J. Polym. Sci. Part A Gen. Pap.* **1963**, *1*, 311–320.

(115) Katsumoto, Y.; Tanaka, T.; Sato, H.; Ozaki, Y. Conformational Change of Poly (N - Isopropylacrylamide) during the Coil - Globule Transition Investigated by Attenuated Total Reflection / Infrared Spectroscopy and Density. *J. Phys. Chem. A* **2002**, *106*, 3429–3435.

(116) Simmons, D. S.; Sanchez, I. C. A Model for a Thermally Induced Polymer Coil-to-Globule Transition. *Macromolecules* **2008**, *41*, 5885–5889.

(117) Zhang, J.; Xu, S.; Kumacheva, E. Photogeneration of Fluorescent Silver Nanoclusters in Polymer Microgels. *Adv. Mater.* **2005**, *17*, 2336–2340.

(118) Suzuki, D.; Kawaguchi, H. Gold Nanoparticle Localization at the Core Surface by Using Thermosensitive Core-Shell Particles as a Template. *Langmuir* **2005**, *21*, 12016–12024.

(119) Pich, A.; Karak, A.; Lu, Y.; K. Ghosh, A.; P. Adler, H. J. Tuneable Ctalytic Properties of Hybrid Microgels Containing Gold Nanoparticles. *Journal of Nanoscience and Nanotechnology* **2006**, *6*, 3763-3769.

(120) Whilton, N. T.; Berton, B.; Bronstein, L.; Hentze, H.-P.; Antonietti, M. Organized Functionalization of Mesoporous Silica Supports Using Prefabricated Metal-Polymer Modules. *Adv. Mater.* **1999**, *11*, 1014–1018.

(121) Biffis, A. Functionalised Microgels: Novel Stabilisers for Catalytically Active Metal Colloids. *J. Mol. Catal. A Chem.* **2001**, *165*, 303–307.

(122) Zhang, J.; Xu, S.; Kumacheva, E. Polymer Microgels: Reactors for Semiconductor, Metal, and Magnetic Nanoparticles. *J. Am. Chem. Soc.* **2004**, *126*, 7908–7914.

(123) Antonietti, M.; Ozin, G. A. Promises and Problems of Mesoscale Materials Chemistry or Why Meso? *Chem. - A Eur. J.* **2004**, *10*, 28–41.

(124) Biffis, A.; Orlandi, N.; Corain, B. Microgel-Stabilized Metal Nanoclusters: Size Control by Microgel Nanomorphology. *Adv. Mater.* **2003**, *15*, 1551–1555.

(125) Janssens, T. V. W.; Clausen, B. S.; Falsig, H.; Christensen, C. H. Catalytic Activity of Au Nanoparticles Au Is Usually Viewed as an Inert Metal , but Surprisingly It Has Been Found. *Nanotoday* **2007**, *2*, 14–18.

(126) Hammer, B.; Norskov, J. K. Why Gold Is the Noblest of All the Metals. *Nature*, **1995**, *376*, 238–240.

(127) Haruta, M.; Kobayashi, T.; Sano, H.; Yamada, N. Novel Gold Catalysts for the Oxidation of Carbon Monoxide at a Temperature Far below 0.DEG.C. *Chem. Lett.* **1987**, 405–408.

(128) Hervés, P.; Pérez-Lorenzo, M.; Liz-Marzán, L. M.; Dzubiella, J.; Lu, Y.; Ballauff, M. Catalysis by Metallic Nanoparticles in Aqueous Solution: Model Reactions. *Chem.*

Soc. Rev. **2012**, *41*, 5577-5587.

(129) Wunder, S.; Polzer, F.; Lu, Y.; Mei, Y.; Ballauff, M. Kinetic Analysis of Catalytic Reduction of 4-Nitrophenol by Metallic Nanoparticles Immobilized in Spherical Polyelectrolyte Brushes. *J. Phys. Chem. C* **2010**, *114*, 8814–8820.

(130) Fenger, R.; Fertitta, E.; Kirmse, H.; Thünemann, a. F.; Rademann, K. Size Dependent Catalysis with CTAB-Stabilized Gold Nanoparticles. *Phys. Chem. Chem. Phys.* **2012**, *14*, 9343-9349.

(131) Esumi, K.; Isono, R.; Yoshimura, T. Preparation of Silver-, Platinum-, and Palladium-PAMAM Dendrimer Nanocomposites and Their Catalytic Activities for Reduction of 4-Nitrophenol. *Shikizai Kyokaishi* **2003**, *76*, 421–427.

(132) Pradhan, N.; Pal, A.; Pal, T. Silver Nanoparticle Catalyzed Reduction of Aromatic Nitro Compounds. *Colloids Surfaces A Physicochem. Eng. Asp.* **2002**, *196*, 247–257.

(133) Ghosh, S. K.; Mandal, M.; Kundu, S.; Nath, S.; Pal, T. Bimetallic Pt-Ni Nanoparticles Can Catalyze Reduction of Aromatic Nitro Compounds by Sodium Borohydride in Aqueous Solution. *Appl. Catal. A Gen.* **2004**, *268*, 61–66.

(134) Yoshimura, T.; Hayakawa, K.; Esumi, K.; Hayakawa, K. Preparation of Gold-Dendrimer Nanocomposites by Laser Irradiation and Their Catalytic Reduction of 4-Nitrophenol. *Langmuir* **2003**, *19*, 5517–5521.

(135) Mei, Y.; Sharma, G.; Lu, Y.; Ballauff, M.; Drechsler, M.; Irrgang, T.; Kempe, R. High Catalytic Activity of Platinum Nanoparticles Immobilized on Spherical Polyelectrolyte Brushes. *Langmuir* **2005**, *21*, 12229–12234.

(136) Mei, Y.; Lu, Y.; Polzer, F.; Ballauff, M.; Drechsler, M. Catalytic Activity of Palladium Nanoparticles Encapsulated in Spherical Polyelectrolyte Brushes and Core - Shell Microgels. *Chem. - A Eur. J.* **2007**, *19*, 1062–1069.

(137) Panigrahi, S.; Basu, S.; Praharaj, S.; Pande, S.; Jana, S.; Pal, a; Ghosh, S.; Pal, T. Sythesis and Size-Selective Catalysis by Supported Gold Nanoparticles: Study on Heterogeneoue and Homogeneous Catalytic Process. *J. Phys. Chem. C* **2009**, *111*, 4596-4605.

(138) Cao, J.; Mei, S.; Jia, H.; Ott, A.; Ballauff, M.; Lu, Y. In Situ Synthesis of Catalytic Active Au Nanoparticles onto Gibbsite-Polydopamine Core-Shell Nanoplates.

Langmuir **2015**, *31*, 9483–9491.

(139) Antonels, N. C.; Meijboom, R. Preparation of Well-De Fi Ned Dendrimer Encapsulated Ruthenium Nanoparticles and Their Evaluation in the Reduction of 4 - Nitrophenol According to the Langmuir − Hinshelwood Approach. *Langmuir* **2013**, *29*, 13433-13442.

(140) Kaiser, J.; Leppert, L.; Welz, H.; Polzer, F.; Wunder, S.; Wanderka, N.; Albrecht, M.; Lunkenbein, T.; Breu, J.; Kümmel, S.; *et al.* Catalytic Activity of Nanoalloys from Gold and Palladium. *Phys. Chem. Chem. Phys.* **2012**, *14*, 6487-6495.

(141) Santos, K. D. O.; Elias, W. C.; Signori, A. M.; Giacomelli, F. C.; Yang, H.; Domingos, J. B. Synthesis and Catalytic Properties of Silver Nanoparticle-Linear Polyethylene Imine Colloidal Systems. *J. Phys. Chem. C* **2012**, *116*, 4594–4604.

(142) Baruah, B.; Gabriel, G. J.; Akbashev, M. J.; Booher, M. E. Facile Synthesis of Silver Nanoparticles Stabilized by Cationic Polynorbornenes and Their Catalytic Activity in 4-Nitrophenol Reduction. *Langmuir* **2013**, *29*, 4225–4234.

(143) Johnson, J. A.; Makis, J. J.; Marvin, K. A.; Rodenbusch, S. E.; Stevenson, K. J. Size-Dependent Hydrogenation of P-Nitrophenol with Pd Nanoparticles Synthesized with Poly(amido)amine Dendrimer Templates. *J. Phys. Chem. C* **2013**, *117*, 22644–22651.

(144) Gu, S.; Lu, Y.; Kaiser, J.; Albrecht, M.; Ballauff, M. Kinetic Analysis of the Reduction of 4-Nitrophenol Catalyzed by Au/Pd Nanoalloys Immobilized in Spherical Polyelectrolyte Brushes. *Phys. Chem. Chem. Phys.* **2015**, *17*, 28137–28143.

(145) Gu, S.; Wunder, S.; Lu, Y.; Ballauff, M.; Fenger, R.; Rademann, K.; Jaquet, B.; Zaccone, A. Kinetic Analysis of the Catalytic Reduction of 4-Nitrophenol by Metallic Nanoparticles. *J. Phys. Chem. C* **2014**, *118*, 18618–18625.

(146) Gu, S.; Kaiser, J.; Marzun, G.; Ott, A.; Lu, Y.; Ballauff, M.; Zaccone, A.; Barcikowski, S.; Wagener, P. Ligand-Free Gold Nanoparticles as a Reference Material for Kinetic Modelling of Catalytic Reduction of 4-Nitrophenol. *Catal. Letters* **2015**, *145*, 1105–1112.

(147) Wang, Y.; Wei, G.; Zhang, W.; Jiang, X.; Zheng, P.; Shi, L.; Dong, A. Responsive Catalysis of Thermoresponsive Micelle-Supported Gold Nanoparticles. *J. Mol. Catal. A Chem.* **2007**, *266*, 233–238.

(148) Al-Kaysi, R. O.; Müller, A. M.; Bardeen, C. J. Photochemically Driven Shape Changes

of Crystalline Organic Nanorods. *J. Am. Chem. Soc.* **2006**, *128*, 15938–15939.

(149) Frattini, A.; Pellegri, N.; Nicastro, D.; De Sanctis, O. Effect of Amine Groups in the Synthesis of Ag Nanoparticles Using Aminosilanes. *Mater. Chem. Phys.* **2005**, *94*, 148–152.

(150) Devos, I.; Womes, M.; Heilemann, M.; Olivier-Fourcade, J.; Jumas, J.-C.; Tirado, J. L. Lithium Insertion Mechanism in CoSb3 Analysed by 121Sb Mössbauer Spectrometry, X-Ray Absorption Spectroscopy and Electronic Structure Calculations. *J. Mater. Chem.* **2004**, *14*, 1759-1767.

(151) Nabid, M. R.; Bide, Y.; Niknezhad, M. Fe3O4-SiO2-P4VP pH-Sensitive Microgel for Immobilization of Nickel Nanoparticles: An Efficient Heterogeneous Catalyst for Nitrile Reduction in Water. *Chemcatchem* **2014**, *6*, 538-546.

(152) Graf, C.; Vossen, D. L. J.; Imhof, A.; Van Blaaderen, A. A General Method to Coat Colloidal Particles with Silica. *Langmuir* **2003**, *19*, 6693–6700.

(153) Washio, I.; Xiong, Y.; Yin, Y.; Xia, Y. Reduction by the End Groups of Poly(vinyl Pyrrolidone): A New and Versatile Route to the Kinetically Controlled Synthesis of Ag Triangular Nanoplates. *Adv. Mater.* **2006**, *18*, 1745–1749.

(154) Xiong, Y.; Washio, I.; Chen, J.; Cai, H.; Li, Z. Y.; Xia, Y. Poly (vinyl Pyrrolidone): A Dual Functional Reductant and Stabilizer for the Facile Synthesis of Noble Metal Nanoplates in Aqueous Solutions. *Langmuir* **2006**, *22*, 8563–8570.

(155) Debye, P. Reaction Rates in Ionic Solutions. *J. Electrochem. Soc.* **1942**, *82*, 265–272.

(156) Hwee, C.; Ng, B.; Fan, W. Y. Shape Evolution of Cu 2 O Nanostructures via Kinetic and Thermodynamic Controlled Growth. *J. Phys. Chem. B* **2006**, 20801–20807.

(157) Zhang, D.-F.; Zhang, H.; Guo, L.; Zheng, K.; Han, X.-D.; Zhang, Z. Delicate Control of Crystallographic Facet-Oriented Cu2O Nanocrystals and the Correlated Adsorption Ability. *J. Mater. Chem.* **2009**, *19*, 5220-5225.

(158) Xu, H.; Wang, W.; Zhu, W. Shape Evolution and Size-Controllable Synthesis of Cu2O Octahedra and Their Morphology-Dependent Photocatalytic Properties. *J. Phys. Chem. B* **2006**, *110*, 13829–13834.

(159) Zhang, Y.; Deng, B.; Zhang, T.; Gao, D.; Xu, A.-W. Shape Effects of CU2O Polyhedral

Microcrystals on Photocatalytic Activity. *J. Phys. Chem. C* **2010**, *114,*5073-5079.

(160) Pal, J.; Ganguly, M.; Mondal, C.; Roy, A.; Negishi, Y.; Pal, T. Crystal-Plane-Dependent Etching of Cuprous Oxide Nanoparticles of Varied Shapes and Their Application in Visible Light Photocatalysis. *J. Phys. Chem. C* **2013**, *117*, 24640–24653.

(161) Tang, A.; Xiao, Y.; Ouyang, J.; Nie, S. Preparation, Photo-Catalytic Activity of Cuprous Oxide Nano-Crystallites with Different Sizes. *J. Alloys Compd.* **2008**, *457*, 447–451.

(162) Hansen, B. J.; Kouklin, N.; Lu, G.; Lin, I. K.; Chen, J.; Zhang, X. Transport, Analyte Detection, and Opto-Electronic Response of P-Type CuO Nanowires. *J. Phys. Chem. C* **2010**, *114*, 2440–2447.

(163) Zhang, F.; Zhu, A.; Luo, Y.; Tian, Y.; Yang, J.; Qin, Y. CuO Nanosheets for Sensitive and Selective Determination of H 2 S with High Recovery Ability. *J. Phys. Chem. C* **2010**, *114*, 19214–19219.

(164) Torrisi, F.; Hasan, T.; Wu, W. P.; Sun, Z. P.; Lombardo, A.; Kulmala, T. S.; Hsieh, G. W.; Jung, S. J.; Bonaccorso, F.; Paul, P. J.; *et al.* Inkjet-Printed Graphene Electronics. *ACS Nano* **2012**, *6*, 2992–3006.

(165) Fromm, J. E. Numerical Calculation of the Fluid Dynamics of Drop-on-Demand Jets. *IBM J. Res. Dev.* **1984**, *28*, 322–333.

(166) Kuo, C. H.; Chen, C. H.; Huang, M. H. Seed-Mediated Synthesis of Monodispersed Cu2O Nanocubes with Five Different Size Ranges from 40 to 420 Nm. *Adv. Funct. Mater.* **2007**, *17*, 3773–3780.

(167) Zhu, H.; Wang, J.; Xu, G. Fast Synthesis of Cu 2 O Hollow Microspheres and Their Application in DNA Biosensor of Hepatitis B Virus & DESIGN 2009. *Cryst. Growth Des.* **2009**, *9*, 633–638.

(168) Kuo, C.H.; Huang, M. H. Morphologically Controlled Synthesisi of Cu2O Nanocrystals and Their Properties. *Nano Today* **2010**, *5*, 106–116.

(169) Zhu, H.; Zhang, C.; Yin, Y. Novel Synthesis of Copper Nanoparticles: Influence of the Synthesis Conditions on the Particle Size. *Nanotechnology* **2005**, *16*, 3079.

(170) Zhang, D. F.; Zhang, H.; Guo, L.; Zheng, K.; Han, X. D.; Zhang, Z. Delicate Control of Crystallographic Facet-Oriented Cu2O Nanocrystals and the Correlated Adsorption

Ability. *J. Mater. Chem.* **2009**, *19*, 5220–5225.

(171) Zhang, L.; Wang, H. Cuprous Oxide Nanoshells with Geometrically Tunable Optical Properties. *ACS Nano* **2011**, *5*, 3257–3267.

(172) Karg, M.; Pastoriza-Santos, I.; Pérez-Juste, J.; Hellweg, T.; Liz-Marzán, L. M. Nanorod-Coated PNIPAM Microgels: Thermoresponsive Optical Properties. *Small* **2007**, *3*, 1222–1229.

(173) Chaudhuri, R. G.; Paria, S. Core / Shell Nanoparticles : Classes , Properties , Synthesis Mechanisms , Characterization , and Applications. *Chem. Rev.* **2012**, 2373–2433.

(174) Hellweg, T. Towards Large-Scale Photonic Crystals with Tuneable Bandgaps. *Angew. Chemie - Int. Ed.* **2009**, *48*, 6777–6778.

(175) Schmidt, S.; Motschmann, H.; Hellweg, T.; von Klitzing, R. Thermoresponsive Surfaces by Spin-Coating of PNIPAM-Co-PAA Microgels: A Combined AFM and Ellipsometry Study. *Polymer*, **2008**, *49*, 749–756.

(176) Yu, W. L.; Lin, Y. Z.; Zhu, X. W.; Hu, Z. G.; Han, M. J.; Cai, S. S.; Chen, L. L.; Shao, H. H. Diversity of Electronic Transitions and Photoluminescence Properties of P-Type Cuprous Oxide films:A Temperature-Dependent Spectral Transmittance Study. *J. Appl. Phys.* **2015**, 045701.

(177) Schmid, M.; Andrae, P.; Manley, P. Plasmonic and Photonic Scattering and near Field of Nanoparticles. *nanoscale Res. Lett.* **2014**, 50.

(178) Janosch Kneer, Juergen Woellenstein, S. P. Manipulating the Gas-Surface Interaction between Copper (II) Oxide and Mono-Nitrogen Oxides Using Temperature. *Sensors Actuators B Chem.* **2016**, *229*, 57–62.

(179) Ghassemzadeh, L.; Peckham, T. J.; Weissbach, T.; Luo, X.; Holdcroft, S. Selective Formation of Hydrogen and Hydroxyl Radicals by Electron Beam Irradiation and Their Reactivity with Perfluorosulfonated Acid Ionomer. *J. Am. Chem. Soc.* **2013**, *135*, 15923–15932.

(180) Dong, F.; Zhao, W.; Wu, Z.; Guo S. Band Structure and Visible Light Photocatalytic Activity of Multi-Type Nitrogen Doped TiO2 Nanoparticles Prepared by Thermal Decomposition. *J. Hazard. Mater.* **2009**, *162*, 763–770.

(181) Xiang, Q.; Yu, J.; Jaroniec, M. Nitrogen and Sulfur Co-Doped TiO2 Nanosheets with Exposed {001} Facets: Synthesis, Characterization and Visible-Light Photocatalytic Activity. *Phys. Chem. Chem. Phys.* **2011**, *13*, 4853–4861.

(182) Fujieda, T.; Ohta, K.; Wakabayashi, N.; Higuchi, S. H-Aggregation of Methyl Orange at the Interface between the Water Phase and Oil Phase in a Water-in-Oil Microemulsion. *J. Colloid Interface Sci* **1997**, *185*, 332–334.

(183) Deegan, R. D.; Bakajin, O.; Dupont, T. F.; Huber, G.; Nagel, S. R.; Witten, T. a. Capillary Flow as the Cause of Ring Stains from Dried Liquid Drops. *Lett. to Nat.* **1997**, *389*, 827–829.

(184) Yamazoe, N.; Shimanoe, K. Theory of Power Laws for Semiconductor Gas Sensors. *Sensors Actuators B* **2008**, *128*, 566–573.

(185) Huang, T.; Meng, F.; Qi, L. Facile Synthesis and 1D Assembly of Cyclodextrin-Capped Gold Nanoparticles and Their Applications in Catalysis and SERS. *J. Phys. Chem. C* **2009**, *113,* 13636-13642.

(186) Sylvestre, J. P.; Kabashin, A. V.; Sacher, E.; Meunier, M.; Luong, J. H. T. Stabilization and Size Control of Gold Nanoparticles during Laser Ablation in Aqueous Cyclodextrins. *J. Am. Chem. Soc.* **2004**, *126*, 7176–7177.

(187) Kettel, M. J.; Dierkes, F.; Schaefer, K.; Moeller, M.; Pich, A. Aqueous Nanogels Modified with Cyclodextrin. *Polymer (Guildf).* **2011**, *52*, 1917–1924.

(188) Uekama, K.; Hirayama, F.; Irie, T. Cyclodextrin Drug Carrier Systems. *Chem Rev* **1998**, *98*, 2045–2076.

(189) Guo, J.; Suslick, K. S. Gold Nanoparticles Encapsulated in Porous Carbon. *Chem. Commun. (Camb).* **2012**, *48*, 11094–11096.

(190) Jana, N. R.; Gearheart, L.; Murphy, C. J.; Carolina, S. Seeding Growth for Size Control of 5 - 40 Nm Diameter Gold Nanoparticles. **2001**, 6782–6786.

List of Figures

List of Tables

List of Publications

[1] **He Jia**, Dominik Schmitz, Andreas Ott, Andrij Pich*, Yan Lu*, "Cyclodextrin Modified Microgels as Nanoreactor for Generation of Au Nanoparticles with Enhanced Catalytic Activity". *J. Mater. Chem. A,* **3** (2015) 6187-6195.

[2] **He Jia**, Rafael Roa, Stefano Angioletti-Uberti, Katja Henzler, Andreas Ott, Xianzhong Lin, Jannik Moeser, Zdravko Kochovski, Alexander Schnegg, Joachim Dzubiella, Matthias Ballauff, Yan Lu*, "Thermosensitive Cu_2O@PNIPAM core-shell nanoreactors with tunable photocatalytic activity." *J. Mater. Chem. A,* **4** (2016) 9677-9684.

[3] **He Jia**, Kneer Janosch, Xianzhong Lin, Qidi Ran, Miriam Siebenbürger, Jie Cao, Palzer Stefan, Yan Lu*, "Preparation of Cu_2O@PNIPAM core-shell nanoparticles as novel inkjet material for gas sensing layers", To be submitted.

[4] Jie Cao, Shilin Mei, **He Jia**, Andreas Ott, Matthias Ballauff and Yan Lu*, "In-situ synthesis of Catalytic Active Au nanoparticles onto Gibbsite-Polydopamine Core-Shell Nanoplates", Langmuir, **31** (2015) 9483-9491.

[5] Katja Henzler, Axel Heilmann, Janosch Kneer, Peter Guttmann, **He Jia**, Eckhard Bartsch, Yan Lu, Stefan Palzer*, "NEXAFS-TXM imaging of the gas-surface reaction of functional CuO nanospheres and octahedrons", Scientific Report, **5** (2015) 17729.

List of Abbreviations

PNIPAM	poly(N-isopropylacrylamide)
α-CD	α-cyclodextrin
PVCL	poly(N-vinylcaprolactam)
Nip	4-nitrophenol
DMNip	2,6-dimethyl-4-nitrophenol
LCST	lower critical solution temperature
PS	polystyrene
NPs	nanoparticles
SPB	spherical polyelectrolyte brushes
PVP	polyvinylpyrrolidone
SEM	Scanning electron microscope
TEM	Transmission electron microscopy
fcc	face-centered cubic
XRD	X-ray diffraction
NEXAFS-TXM	Near edge X-ray absorption fine structure
DLS	Dynamic light scattering
MO	Methyl Orange
UV-vis	Ultraviolet-visible spectroscopy
ESR	Electron spin resonance
t_0	induction time
k_{app}	apparent rate constant
S	total surface of all metal nanoparticles
k_1	normalized kinetic constant

Hx	4-hydroxylaminophenol
Amp	4-aminophenol
k_a	reaction rate of step A
θ_{Nip}	surface coverage of the nanoparticles by Nip
θ_{BH4}	surface coverage of the nanoparticles by borohydride
c_{Nip}	actual concentrations of Nip
c_{Hx}	actual concentrations of 4-hydroxylaminophenol
c_{BH4}	actual concentrations of Amp
K	Langmuir adsorption constants
k_b	reaction rate of step B
NB	Nitrobenzene
k_t	total reaction rate
k_D	diffusion controlled reaction rate
k_R	surface reaction controlled rate constant
R_{np}	radius of nanoparticles
D(r)	distance-dependent diffusion constant
$\Delta G_{sol}(r)$	local free enthalpy
c_0	concentration of reactant in the bulk solution
$\Delta\overline{G}_{sol}$	transfer free energy
Eg	energy band
VB	valence band
CB	conduction band
MB	Methylene Blue
Z	inverse of the Ohnesorge number

a	radius of the printing orifice
ρ	density
γ	surface tension
η	viscosity
MSD	minimum stand-off distance
SDS	sodium dodecyl sulfate
TEOS	tetraethyl orthosilicate
V50	2,2'-azobis(2-methylpropionamidine dihydrochloride)
PDDA	poly(diallyldimethylammonium chloride)
NaSS	4-styrenesulfonic acid sodium salt hydrate
SAED	selected area electron diffraction
BIS	N,N'-methylene-bis-acrylamide
TXM	transmission X-ray microscopy
TGA	Thermogravimetric Analysis
DMPO	5,5-dimethyl-pyrrdine N-oxide
AAEM	toacetoxyethyl methacrylate
FI-IR	Fourier transform infrared spectroscopy
SPR	surface plasmon resonance
VPTT	volume phase transition temperature
CTAB	solid cetyltrimethylammonium bromide

Acknowledgement

I would like to express my gratitude to all of those who selflessly provide their helps during this 4 years in Germany. As a student from foreign country, I am proud to say that I will never regret to come to Helmholtz-Zentrum Berlin, which is notable for its excellent research.

My deepest gratitude first goes to Prof. Matthias Ballauff and Prof. Yan Lu for their constant encouragement and guidance. They have walked me through all the stages of my PhD study. They supported me through academic discussions and emotional encouragement through the whole work to finish this thesis. Without their consistent and illuminating instruction, this dissertation could not have reached its present form. Moreover, I appreciate their patience and precious comments to improve my writing and presentation skills.

Also, I would like to convey my appreciation to Prof. Dr. Joachim Dzubiella, Dr. Rafael Roa Chamorro and Dr. Stefano Angioletti-Uberti for the cooperation with all the theoretical simulations and useful discussions. Much thanks to Dr. Katja Henzler for her efforts on NEXAFS-TXM measurements, to Andreas Ott, Cao Jie, Qidi Ran and Sasa Gu for all TEM measurements. I thank Dr. Alexander Schnegg for offering the opportunity to perform ERS measurements in his lab and all the assistance and efforts from Mr. Moeser Jannik during measurements. For the photo-catalytic measurement, I appreciate all the useful guidance and help from Dr. Thomas Dittrich. For the Rheological measurements, much thanks to my colleges Dr. Miriam Siebenbürger who offered helpful introductions and comments. Dr. Xianzhong Lin and Mr. Fuxian Wang also supported me a lot for the XRD measurements.

I am also greatly indebted to the professors and researchers from RWTH Aachen University: Prof. Andrij Pich and Mr. Dominik Schmitz. They offered the PVCL microgels for my research and supplied their best supports and instructions in my research.

Also, my thanks would go to Dr. Stefan Palzer and Dr. Janosch Kneer, who have helped me a lot on ink-jet printing and gas sensor measurement.

In the following, I would like to thank all the colleges in HZB for the friendly work environment with nice breaks. In particular, I would like to thank Dr. Nikoline Hansen and Ms. Estrella Macarro for their kindness and great help. Additionally, I would like to thank all the help from my colleges and my friends from Andreas Ott, Nils Heptner, Karol Palczynski, Yan Yang, Guanchao Yin, Xiao Xu, Xiaxia Liao, Penghui Yang, Fangfang Chu, Yang Liu for all the kindness during my normal life and all the great time after work. Next, I would like to

especially thank Shilin Mei, Xianzhong Lin, Jie Cao and Meng Liu, who helped me in my most difficult time in Berlin. Of course, all my friends from the HZB and all my Chinese friends in Berlin are highly appreciated.

At last but not the least, I would like to express my heartfelt gratitude to my father and my mother for their considerations and great confidence in me all through these years. Moreover, I would like to thank my wife, Dr. Hui Shang. Her understanding, encouragement and love give me the courage to continue my studying in a foreign country.

Selbstständigkeitserklärung

Hiermit erkläre ich die vorliegende Arbeit selbst verfasst und nur unter Zuhilfenahme der angegebenen Hilfsmittel angefertigt zu haben.

Ferner erkläre ich, dass ich nicht anderweitig mit oder ohne Erfolg versucht habe, eine Dissertation einzureichen oder mich einer Doktorprüfung zu unterziehen.

Berlin, den 06.07.2016

He JIA